# Superconductivity in quasiperiodic systems and magic-angle semimetals

Ricardo Francisco de Oliveira
Mestrado em Física
Departamento de Física e Astronomia
2022

**Orientador**
Prof. Dr. Eduardo Filipe Vieira De Castro, Universidade do Porto

**Co-orientador**
Prof. Dr. Bruno António Campos Amorim, Universidade do Minho

U.PORTO

FACULDADE DE CIÊNCIAS
UNIVERSIDADE DO PORTO

Todas as correções determinadas pelo júri, e só essas, foram efetuadas.

O Presidente do Júri,

Porto, _____/_____/_____

# Declaração de Honra

Eu, Ricardo Francisco Oliveira, inscrito no Mestrado em Física da Faculdade de Ciências da Universidade do Porto declaro, nos termos do disposto na alínea a) do artigo 14.º do Código Ético de Conduta Académica da U.Porto, que o conteúdo da presente dissertação reflete as perspetivas, o trabalho de investigação e as minhas interpretações no momento da sua entrega.

Ao entregar esta dissertação, declaro, ainda, que a mesma é resultado do meu próprio trabalho de investigação e contém contributos que não foram utilizados previamente noutros trabalhos apresentados a esta ou outra instituição.

Mais declaro que todas as referências a outros autores respeitam escrupulosamente as regras da atribuição, encontrando-se devidamente citadas no corpo do texto e identificadas na secção de referências bibliográficas. Não são divulgados na presente dissertação quaisquer conteúdos cuja reprodução esteja vedada por direitos de autor.

Tenho consciência de que a prática de plágio e auto-plágio constitui um ilícito académico.

Ricardo Francisco Oliveira

Porto, 11 de outubro de 2022

Faculdade de Ciências da Universidade do Porto

Master's Thesis

# Superconductivity in quasiperiodic systems and magic-angle semimetals

**Ricardo Francisco de Oliveira**

**Supervisors:**
Prof. Dr. Eduardo Filipe Vieira de Castro
Prof. Dr. Bruno António Campos Amorim

*A thesis submitted in fulfilment of the requirements*
*for the degree of Master of Science in Theoretical Physics*
*at*
Departamento de Física e Astronomia

**Porto, September 2022**

# Acknowledgements

I'm extremely grateful to my supervisors Dr. Eduardo Castro and Dr. Bruno Amorim for their continued guidance and assistance thoughout all this work, and would like to extend my sincere thanks to Miguel Gonçalves for his invaluable insights in our weekly meetings.

To my family goes my deepest gratitude for their unwavering support throughout this past year. Their belief in me was invaluable.

# Resumo

Neste trabalho estudamos supercondutividade singleto, do tipo onda s, numa variedade de modelos de tight-binding incomensurados. Estes incluem sistemas quasiperiódicos 1D, tal como o modelo clássico de Aubry-André-Harper e uma variante que apresenta uma modulação quasiperiódica dos hoppings a primeiros vizinhos, assim como um modelo de um semimetal de ângulo-mágico que emula a bicamada de grafeno rodada no limite quiral. Estudando a equação do hiato supercondutor linearizada, mostrámos que existe uma amplificação da fase supercondutora, associada a um acréscimo da temperatura crítica, na transição do regime estendido para o localizado nos sistemas 1D. Também determinamos que os parâmetros de hiato supercondutores, nos modelos 1D quasiperiódicos, herdam as propriedades de localização dos estados próprios do Hamiltoniano de uma partícula. Identificámos um escalamento em lei de potência da temperatura crítica supercondutora com o acoplamento da interação, com diferentes expoentes para os regimes críticos e estendido dos sistemas 1D. Finalmente, encontramos um escalamento reforçado da temperatura crítica supercondutor, devido à incommensurabilidade, no regime de acoplamento da interação fraco para a fase metálica do modelo quiral da bicamada de grafeno rodada.

# Abstract

In this work we study s-wave singlet superconductivity in a variety of incommensurate tight-binding models. These include 1D quasiperiodic systems, such as the classical Aubry-André-Harper model and an extended variant which features a quasiperiodical modulation of the nearest-neighbor hoppings, along with a magic-angle semimetal model that emulates twisted bilayer graphene for moderate angles in the chiral limit. By studying the linearized superconductor gap equation, we showed that there is enhancement of superconductivity, associated with an increased critical temperature, when we transition from the extended to the localized regime in these 1D systems. We also determined that the superconductor gap parameters, in the 1D quasiperiodic models, inherite much of the localization properties of the single-particle Hamiltonian. We found that the superconducting critical temperature has a power-law scaling with the interaction coupling characterized by different exponents for both the critical and localized regimes in the 1D sytems. Finally, we also found that the critical temperature has an enhanced scaling, due to incommensurability, in the weak interaction coupling regime for the metallic phase of the chiral twisted bilayer graphene model.

# Contents

# List of Figures

# Chapter 1

# Introduction

Superconductors are a class of materials whose electrical resistance drops abruptly to zero below a characteristic critical temperature. This contrasts with ordinary metallic conductors for which this happens gradually as their temperature approaches absolute zero. Another important phenomenon associated with superconductivity is the Meissner effect [1] which manifests itself through the expulsion of magnetic field lines from the interior of a superconducting material. The vanishing of resistivity and the occurrence of the Meissner effect are two phenomena that any superconductivity theory should be able to explain.

The first theories of superconductivity were of a phenomenological nature, such as the London equations by Fritz London and Heinz London which predicted an expression for the penetration depth $\lambda$ of a magnetic field in a superconductor, or the Ginzburg-Landau theory that introduced a superconductor order parameter and a coherence length that changes between the normal and superconducting phases.

However, the first microscopic theory came in the form of the theory by Bardeen, Cooper and Schrieffer (BCS) in 1957 [2]. In this theory, a bound pair (Cooper pair) is formed by two electrons with equal and opposite momenta near the Fermi surface, due to an effective attractive interaction, mediated by the lattice phonons, that overcomes the Coulomb repulsion. The two principal mechanisms of the BCS theory are then the formation of Cooper pairs which manifests itself as an energy gap $\Delta(T)$ in the quasiparticle density of states at the Fermi level, that goes to zero at the critical temperature, and the condensation of these pairs into a phase coherent macroscopic quantum state that gives rise to a finite superfluid density.

These theories fail to explain the so-called high-temperature cuprate supercondutors, since the absence of the isotope effect, where the critical temperature scales as $T_c \sim M^{-\frac{1}{2}}$ with the isotopic mass, indicates that there is no phonon mediation in the formation of pairs in this class of superconductors. This new type of materials were first discovered in 1986, by Bednorz and Müller [3], and, since then, there have been many attempts at finding a suitable microscopic theory that explains the mechanism behind these high-temperature superconductors.

## 1.1 Motivation

A recent development in 2018, by a research team at MIT [4], consisted of the realization of intrinsic unconventional superconductivity in twisted bilayer graphene for twist angles of $\sim 1.1°$, the so-called

"magic" angle.

In twisted bilayer graphene (tBLG), a van der Waals material, two stacked graphene layers that are rotated with respect to one another by a small angle form a long-wavelength moiré pattern. At certain discrete values of the twist angle, the so-called magic angles, the Fermi velocity of the fermions at the Dirac cones vanishes and two narrow, nearly flat, bands (per valley per spin) develop in the middle of the full spectrum, for energies close to the Fermi level, that are separated from other bands [5–9].

These moiré flat bands put tBLG in the strongly-correlated regime, because the bandwith is so narrow that the interactions dominate over the kinetic energy and even weak interactions can lift the near degeneracy of states formed by various single particle levels near the Fermi energy, leading to the emergence of exotic correlated phases. The study of the complex phase diagram of tBLG has gained much interest since the discovery of unconventional superconductivity [4] and correlated insulator behaviour at half-filling [10] by the experimental group of Pablo Jarillo-Herrero.

While correlated insulators in these systems can be explained as a consequence of Coulomb interaction, superconductivity may emerge from an eletron-eletron interaction only or from a more conventional BCS mechanism where the interaction between eletrons is mediated by the phonons of the lattice. The underlying mechanism for superconductivity in tBLG, as in the high-$T_c$ superconductors, is still an open question and has been the subject of intense theoretical studies in the last few years. The theoretical approaches to understanding superconductivity in tBLG range from mean-field theory/Bogoliubov-de Gennes method [11–13] to renormalization group method [14, 15] to the study of the linearized gap equation [16–18].

In tBLG, the eletronic structure is usually well-described by moiré band theory where Bloch's theorem applies to an enlarged unit cell in real space yielding a small moiré Brillouin zone. The twist angles are then generally restricted to a discrete subset that yields commensurate structures. This is in line with the underlying hypothesis of typical continuum models of tBLG that for small twist angles the difference between commensurate and incommensurate angles is not relevant to study the low energy physics of the system [6, 19].

However, this cannot be true in general and quasiperiodic effects that arise from general incommensurable twist angles should be taken into account to give a careful description of tBLG and of the correlated phases, such as superconductivity, that emerge in these systems. Recent work has shown that sub-ballistic states can be found in the narrow-band regime around the magic angle in tBLG for incommensurate twist angles [20]. It was also shown that quasiperiodicity can induce single-particle quantum phase transitions in a class of models called magic-angle semimetals [21], such as the chiral model of tBLG, which hosts multifractal momentum-space wave functions in the narrow-band regime. An enhancement of superconductivity due to the multifractal structure of noninteracting wave functions was also found in the 1D AAH model [22], hinting to a new relationship between incommensurability and superconductivity.

To study quasiperiodicity, one must first understand the historical background which lead to the introduction of this concept in condensed matter theory. The classical theory of eletronic conductivity had the scattering of free eletrons by the ionic cores in metal lattice sites at its foundation. One of its main predictions was that the conductivity in metals should be proportional to the mean free path of the eletrons, i.e., the average distance an eletron travels between colisions with the lattice ions.

The advent of quantum mechanics refined our view of conductivity in metals. It was found that the eletrons, due to their wave character, diffract in an ideal crystal, instead of scattering from the ion cores.

The resistence is due to the scattering of the eletrons from imperfections. What happens when we keep increasing the disorder strength? Will we keep getting a lower conductivity, because of the decreased mean free path in the presence of more impurities? Or will some new phenomena emerge? The answer to the latter question is affirmative. For example, in 3D random lattices there is a critical amount of impurity scattering beyond which there is an absence of diffusion, i.e., eletrons become exponentially localized in the lattice and the conductivity drops to zero (At $T = 0$). This is known as Anderson localization [23] and this metal-insulator transition (MIT) between a diffusive and a localized regime is the so-called Anderson transition due to P. W. Anderson (1958).

The class of systems we will be interested in share some common ground with the Anderson disordered models. The Anderson localization of particles is usually discussed in the context of random potentials, but the fundamental physics of Anderson localization is not contigent on the existence of randomness. Instead, if we have a tight-binding model of a lattice, the essential ingredient is that the differences in potential energy between neighbouring sites should be large when compared to the hopping matrix elements in order to suppress the hopping of eletrons. Of course, we can achieve this with a random potential, but we can also produce it deterministically with quasiperiodic potentials.

The first and simplest model of this kind is the Aubry-André-Harper (AAH) model in 1D [24, 25], which is a nearest-neighbor tight-binding model with a sinusoidal on-site potential whose wavelength is incommensurate with the underlying lattice, i.e., the ratio between the potential wavelength and the lattice parameter is irrational. This type of model can be thought as emerging from the reduction of a 2D Quantum Hall system to a 1D chain, with the Landau gauge chosen in such a way that the vector potential is transverse to the chain [24, 26].

The physics of single–particle Anderson localization in this class of models is as diverse as in the randomly disordered systems, and there have been many developments regarding the critical spectra and multifractal wavefunctions [27–29]. This quasiperiodic localization also survives in extensions of the Aubry-André model to higher dimensions [30–32]. Quasiperiodicity has recently attracted attention due to cold atom experiments on Bose glasses and many-body localization (MBL) [33–42].

The main goal of this thesis is to study the influence of incommensurability on superconducitivity, either on the critical temperature of the system or on the localization of the superconductor local parameter, on 1D systems such as the variants of the AAH model or on the class of magic-angle semimetals such as tBLG.

## 1.2 Outline of thesis

In chapter 2, we develop the Green's function formalism of superconductivity for a general tight-binding Hamiltonian with interactions. The analysis of the interaction term can be reduced to the study of a self-consistent equation of motion for the anomalous Green's function. Near the critical temperature, $T_c$, this reduces to the linear gap equation which is, in its most general form, an eigenvalue problem for the superconductor gap parameter.

Chapter 3 deals with the application of the linear gap equation, developed in the previous chapter, to a single layer of graphene. This simple commensurate system, which has translational invariance, allows a momentum space computation of the critical temperature and an analysis of the symmetry of the superconductor local parameter. The quantum critical point of graphene, when the Fermi level is at the Dirac energy,

is discussed in the context of the dependence of the critical temperature on the coupling constant. We also compare the results of the linear gap equation formulated in momentum and real space, which are in good agreement.

Chapter 4 deals with incommensurate systems which include the 1D Aubry-André-Harper model and a generalization with quasiperiodical modulation of the hoppings. We study the localization properties of the superconductor local parameter and investigate the scaling of the critical temperature with the interaction coupling.

Finally, in chapter 5 we study a magic-angle semimetal that emulates twisted bilayer graphene and also analyze the scaling of the critical temperature when we transition to the metallic phase of the model.

# Chapter 2

# Green's function formalism of superconductivity

The first successful microscopic theory of superconductivity was the BCS theory developed in 1957 [2]. The idea was that a weakly attractive interaction between two electrons leads to the formation of a Cooper pair (boson), which opens up a temperature dependent gap in the energy spectrum. To determine this gap as a function of temperature for a generic system with a BCS interaction term in the Hamiltonian, a possible common approach is to do a mean-field decoupling and compute the superconductor gap self-consistently using the Bogoliubov-de Gennes method.

However, in order to compute the critical temperature corresponding to the transition from a normal metal to a superconducting state, this mean-field method is inadequate due to its slow convergence for temperatures close to the critical temperature as we show in Appendix A. Hence, we need an alternative formalism more suitable for computing the critical temperature. This formalism will be based on a Green's function approach and, within a mean-field approximation, will allow us to derive a linear equation for the superconductor local parameter which provides a computationally efficient way to obtain the critical temperature.

Let us consider a general tight-binding Hamiltonian with interactions

$$\hat{H} = \hat{H}_0 + \hat{H}_{int}, \tag{2.1}$$

where the single-particle term of the Hamiltonian has the general form

$$\hat{H}_0 = \sum_{s,s'} \sum_{i,i'} \sum_{\mathbf{k}} \langle i,s| H_0(\mathbf{k}) |i',s'\rangle \, a^{\dagger}_{\mathbf{k},i,s} a_{\mathbf{k},i',s'}, \tag{2.2}$$

and the operators $\left\{a^{\dagger}_{\mathbf{k},i,s}\right\}$ create a fermion with momentum $\mathbf{k}$, spin $s$, and in the orbital $i$.

The interaction term is given by

$$\hat{H}_{int} = \frac{1}{2} \sum_{s_1,s_2,s_3,s_4} \sum_{i_1,i_2,i_3,i_4} \sum_{\mathbf{k},\mathbf{k}',\mathbf{q}} V^{s_1,s_2,s_3,s_4}_{i_1,i_2,i_3,i_4}(\mathbf{q}) \, a^{\dagger}_{\mathbf{k}+\mathbf{q},i_1,s_1} a^{\dagger}_{\mathbf{k}'-\mathbf{q},i_2,s_2} a_{\mathbf{k}',i_3,s_3} a_{\mathbf{k},i_4,s_4}, \tag{2.3}$$

which corresponds to an effective two-body process, in which two fermions exchange momentum $\mathbf{q}$ with an overall conservation of momentum, that can include the typical BCS phonon-mediated interaction.

Our goal is now to obtain a self-consistent equation for the superconductor gap. In order to do this, we will employ the equation of motion method in the Matsubara formalism, that is commonly used in equilibrium many-body physics [43], for the finite temperature normal Green's function $\mathcal{G}$ and the anomalous Green's function $\mathcal{F}$, in imaginary time $\tau$, defined as:

$$\mathcal{G}_{s,s'}^{i,i'}(\mathbf{k},\mathbf{k}';\tau) \equiv -\left\langle T_\tau a_{\mathbf{k},i,s}(\tau)\, a_{\mathbf{k}',i',s'}^{\dagger}(0)\right\rangle, \tag{2.4}$$

$$\mathcal{F}_{s,s'}^{i,i'}(\mathbf{k},\mathbf{k}';\tau) \equiv \left\langle T_\tau a_{\mathbf{k},i,s}(\tau)\, a_{\mathbf{k}',i',s'}(0)\right\rangle, \tag{2.5}$$

The symbol $T_\tau$ stands for the imaginary time ordering operation and the brackets $\left\langle \cdots \right\rangle$ represent the thermodynamical average over the grand canonical ensemble, i.e., $\left\langle \cdots \right\rangle = Tr\left[e^{-\beta\left(\hat{H}-\mu\hat{N}\right)}(\cdots)\right]/Tr\left[e^{-\beta\left(\hat{H}-\mu\hat{N}\right)}\right]$. The operators $a_{\mathbf{k},i,s}(\tau)$ and $a_{\mathbf{k},i,s}^{\dagger}(\tau)$ evolve according to the Heisenberg equation of motion in imaginary time

$$\frac{da_{\mathbf{k},i,s}}{d\tau} = \left[\hat{H}, a_{\mathbf{k},i,s}\right]. \tag{2.6}$$

## 2.1 Equation of motion of the noninteracting Green's function

As the first use of equation (2.6), let's determine the equation of motion of the noninteracting (free-particle) Green's function defined as

$$\mathcal{G}_{s,s'}^{0;i,i'}(\mathbf{k};\tau) \equiv -\left\langle T_\tau a_{\mathbf{k},i,s}(\tau)\, a_{\mathbf{k},i',s'}^{\dagger}(0)\right\rangle, \tag{2.7}$$

which has the same form as equation (2.4), but now the time evolution of the operators $a_{\mathbf{k},i,s}(\tau)$ is governed solely by the single-particle Hamiltonian $\hat{H}_0$.

The equation of motion is given by

$$\frac{d\mathcal{G}_{s,s'}^{0;i,i'}(\mathbf{k};\tau)}{d\tau} = -\delta(\tau)\,\delta_{i,i'}\delta_{s,s'} - \left\langle T_\tau \frac{da_{\mathbf{k},i,s}}{d\tau}(\tau)\, a_{\mathbf{k},i',s'}^{\dagger}(0)\right\rangle, \tag{2.8}$$

where we use the canonical anti-commutation relation for fermions $\left\{a_i^{\dagger}, a_j\right\} = \delta_{i,j}$ and the fact that the delta function is the derivative of the Heaviside step function. The only quantity that is left to compute in equation (2.8) is $\frac{da_{\mathbf{k},i,s}}{d\tau}(\tau)$. For a free system, this can be determined by the Heisenberg equation of motion (2.6), with $\hat{H} = \hat{H}_0$. After simple algebra,

$$\frac{da_{\mathbf{k},i,s}}{d\tau} = \left[\hat{H}_0, a_{\mathbf{k},i,s}\right] = -\sum_{s'}\sum_{i'} \langle i,s|\, H_0(\mathbf{k})\, |i',s'\rangle\, a_{\mathbf{k},i',s'}. \tag{2.9}$$

The equation of motion for the free-particle Green's function is then given by

$$\frac{d\mathcal{G}^{0;i,i'}_{s,s'}(\mathbf{k};\tau)}{d\tau}+\sum_{s''}\sum_{i''}\langle i,s|\,H_0(\mathbf{k})\,|i'',s''\rangle\,\mathcal{G}^{0;i'',i'}_{s'',s'}(\mathbf{k};\tau)=-\delta(\tau)\,\delta_{i,i'}\delta_{s,s'}. \tag{2.10}$$

We can now define the Fourier transform from $i\omega_n$ to $\tau$ of the noninteracting Green's function as

$$\mathcal{G}^{0;i,i'}_{s,s'}(\mathbf{k};\tau)\equiv\frac{1}{\beta}\sum_{i\omega_n}\mathcal{G}^{0;i,i'}_{s,s'}(\mathbf{k};i\omega_n)\,e^{-i\omega_n\tau}, \tag{2.11}$$

where the fermionic Matsubara frequencies are $i\omega_n=\frac{(2n+1)\pi}{\beta}$, with $n\in\mathbb{Z}$. Identical definitions hold for $\mathcal{G}^{i,i'}_{s,s'}(\mathbf{k},\mathbf{k}';\tau)$ and $\mathcal{F}^{i,i'}_{s,s'}(\mathbf{k},\mathbf{k}';\tau)$. Performing a Fourier transform of equation (2.10), we arrive at

$$\sum_{s''}\sum_{i''}\langle i,s|\,i\omega_n-H_0(\mathbf{k})\,|i'',s''\rangle\,\mathcal{G}^{0;i'',i'}_{s'',s'}(\mathbf{k};i\omega_n)=\delta_{i,i'}\delta_{s,s'}. \tag{2.12}$$

Henceforth, equation (2.12) can be taken as the definition of the noninteracting Green's function $\mathcal{G}^{0;i,i'}_{s,s'}(\mathbf{k};i\omega_n)$.

## 2.2 Equation of motion of the anomalous Green's function $\mathcal{F}^{i,i'}_{s,s'}(\mathbf{k},\mathbf{k}';\tau)$

Now we turn to the anomalous Green's function. As we did for the noninteracting Green's function, we can study it's equation of motion. After some simple algebra and using that the anti-commutation relation $\{a_i,a_j\}=0$ holds for fermions, we obtain

$$\frac{d\mathcal{F}^{i,i'}_{s,s'}(\mathbf{k},\mathbf{k}';\tau)}{d\tau}=\left\langle T_\tau\frac{da_{\mathbf{k},i,s}}{d\tau}(\tau)\,a_{\mathbf{k}',i',s'}(0)\right\rangle \tag{2.13}$$

A crucial difference between this anomalous Green's function and the noninteracting one is that the imaginary time evolution of the operators $a_{\mathbf{k},i,s}(\tau)$ is determined by the full interaction Hamiltonian (2.1). The Heisenberg equation of motion is therefore given by

$$\frac{da_{\mathbf{k},i,s}}{d\tau}=\left[\hat{H},a_{\mathbf{k},i,s}\right]=\left[\hat{H}_0,a_{\mathbf{k},i,s}\right]+\left[\hat{H}_{int},a_{\mathbf{k},i,s}\right]. \tag{2.14}$$

We already computed the first commutator on the right-hand side of Eq. (2.14) in Eq. (2.9). The second commutator is a little more complex,

$$\left[\hat{H}_{int},a_{\mathbf{k},i,s}\right]=\sum_{s_1,s_2,s_3}\sum_{i_1,i_2,i_3}\sum_{\mathbf{k}'',\mathbf{q}}V^{s_1,s,s_2,s_3}_{i_1,i,i_2,i_3}(\mathbf{q})\,a^\dagger_{\mathbf{k}''+\mathbf{q},i_1,s_1}a_{\mathbf{k}+\mathbf{q},i_2,s_2}a_{\mathbf{k}'',i_3,s_3}, \tag{2.15}$$

where we have used the symmetry property $V^{s_1,s_2,s_3,s_4}_{i_1,i_2,i_3,i_4}(\mathbf{q})=V^{s_2,s_1,s_4,s_3}_{i_2,i_1,i_4,i_3}(-\mathbf{q})$, which is derived by anti-commuting the operators and changing dummy variables in the interaction Hamiltonian (2.3). The equation of motion

is then

$$\frac{d\mathcal{F}^{i,i'}_{s,s'}(\mathbf{k},\mathbf{k}';\tau)}{d\tau} = -\sum_{s''}\sum_{i''}\langle i,s|\,H_0(\mathbf{k})\,|i'',s''\rangle\,\mathcal{F}^{i'',i'}_{s'',s'}(\mathbf{k},\mathbf{k}';\tau) + \sum_{s_1,s_2,s_3}\sum_{i_1,i_2,i_3}\sum_{\mathbf{k}'',\mathbf{q}} V^{s_1,s,s_2,s_3}_{i_1,i,i_2,i_3}(\mathbf{q})\left\langle T_\tau a^\dagger_{\mathbf{k}''+\mathbf{q},i_1,s_1}(\tau)\,a_{\mathbf{k}+\mathbf{q},i_2,s_2}(\tau)\,a_{\mathbf{k}'',i_3,s_3}(\tau)\,a_{\mathbf{k}',i',s'}(0)\right\rangle. \quad (2.16)$$

The interaction problem now comes into full picture in the equation of motion, because we now have the non-trivial task of computing a four-point correlation function $\left\langle a^\dagger_i a_j a_k a_l\right\rangle$. The simplest way to solve this problem is to do a mean-field decoupling of the correlation function, reducing the four-point correlation function to products of two-point correlation functions.

Using mean-field decoupling we obtain

$$\left\langle T_\tau a^\dagger_{\mathbf{k}''+\mathbf{q},i_1,s_1}(\tau)\,a_{\mathbf{k}+\mathbf{q},i_2,s_2}(\tau)\,a_{\mathbf{k}'',i_3,s_3}(\tau)\,a_{\mathbf{k}',i',s'}(0)\right\rangle \approx \delta_{i_1,i_2}\delta_{s_1,s_2}\delta_{\mathbf{k}'',\mathbf{k}}n_{\mathbf{k}''+\mathbf{q}}\mathcal{F}^{i_3,i'}_{s_3,s'}(\mathbf{k}'',\mathbf{k}';\tau) - \delta_{i_1,i_3}\delta_{s_1,s_3}\delta_{\mathbf{q},0}n_{\mathbf{k}''+\mathbf{q}}\mathcal{F}^{i_2,i'}_{s_2,s'}(\mathbf{k}+\mathbf{q},\mathbf{k}';\tau) + \left\langle T_\tau a_{\mathbf{k}+\mathbf{q},i_2,s_2}(\tau)\,a_{\mathbf{k}'',i_3,s_3}(\tau)\right\rangle\mathcal{G}^{i',i_1}_{s',s_1}(\mathbf{k}',\mathbf{k}''+\mathbf{q};-\tau), \quad (2.17)$$

where $n_{\mathbf{k},i,s} \equiv \left\langle T_\tau a^\dagger_{\mathbf{k},i,s}(\tau)\,a_{\mathbf{k},i,}(\tau)\right\rangle$ and we can ignore the $\mathbf{q}=0$ term, since we will assume that long-wavelength phonons give a zero potential, so that $V(\mathbf{q}=0)=0$. Using this result, the equation of motion can be written as

$$\frac{d\mathcal{F}^{i,i'}_{s,s'}(\mathbf{k},\mathbf{k}';\tau)}{d\tau} = -\sum_{s'',i'',\mathbf{k}''}\langle\mathbf{k},i,s|\,H_0+\Sigma\,|\mathbf{k}'',i'',s''\rangle\,\mathcal{F}^{i'',i'}_{s'',s'}(\mathbf{k}'',\mathbf{k}';\tau) - \sum_{s'',i'',\mathbf{k}''}\Delta^{i,i''}_{s,s''}(\mathbf{k},\mathbf{k}'')\,\mathcal{G}^{i',i''}_{s',s''}(\mathbf{k}',\mathbf{k}'';-\tau), \quad (2.18)$$

where we have defined the normal metal self-energy as

$$\Sigma^{i,i'}_{s,s'}(\mathbf{k},\mathbf{k}') = \langle\mathbf{k},i,s|\,\Sigma\,|\mathbf{k}',i',s'\rangle \equiv -\sum_{s'',i'',\mathbf{q}} V^{s'',s,s'',s'}_{i'',i,i'',i'}(\mathbf{q})\,n_{\mathbf{k}+\mathbf{q}}\delta_{\mathbf{k},\mathbf{k}'} \quad (2.19)$$

and the superconductor gap parameter as

$$\Delta^{i,i'}_{s,s'}(\mathbf{k},\mathbf{k}') \equiv -\sum_{s_2,s_3}\sum_{i_2,i_3}\sum_{\mathbf{q}} V^{s',s,s_2,s_3}_{i',i,i_2,i_3}(\mathbf{q})\,\mathcal{F}^{i_2,i_3}_{s_2,s_3}(\mathbf{k}+\mathbf{q},\mathbf{k}'-\mathbf{q};0). \quad (2.20)$$

The equation of motion for $\mathcal{F}$ after a Matsubara transform is simply

$$\sum_{s'',i'',\mathbf{k}''}\left[\langle\mathbf{k},i,s|\,i\omega_n - H_0 - \Sigma\,|\mathbf{k}'',i'',s''\rangle\,\mathcal{F}^{i'',i'}_{s'',s'}(\mathbf{k}'',\mathbf{k}';i\omega_n) - \Delta^{i,i''}_{s,s''}(\mathbf{k},\mathbf{k}'')\,\mathcal{G}^{i',i''}_{s',s''}(\mathbf{k}',\mathbf{k}'';-i\omega_n)\right] = 0. \quad (2.21)$$

Henceforth, we shall assume $\Sigma \approx 0$, which is equivalent to saying that the Hartree-Fock self-energy is already included in $H_0$. This is a good approximation for a weak coupling theory, where the Hartree-Fock self-energy in the superconductor state is similar to the normal metal for most materials.

We now wish to invert equation (2.21) and obtain $\mathcal{F}$. This can be achieved using the matrix equation for the noninteracting Green's function (2.12) (See Appendix B for details). Therefore,

$$\mathcal{F}^{i,i'}_{s,s'}(\mathbf{k},\mathbf{k}';i\omega_n) = \sum_{s_1,i_1,\mathbf{k_1}}\sum_{s_2,i_2,\mathbf{k_2}} \mathcal{G}^{0;i,i_1}_{s,s_1}(\mathbf{k};i\omega_n)\,\mathcal{G}^{i',i_2}_{s',s_2}(\mathbf{k}',\mathbf{k_2};-i\omega_n)\,\Delta^{i_1,i_2}_{s_1,s_2}(\mathbf{k},\mathbf{k_2}). \tag{2.22}$$

## 2.3 Self-consistent equation for the gap parameter

The superconductor gap parameter was defined in Eq. (2.20) in terms of the anomalous Green's function. Using the result obtained in Eq. (2.22), we obtain a self-consistent equation for the gap parameter,

$$\Delta^{i,i'}_{s,s'}(\mathbf{k},\mathbf{k}') = -\frac{1}{\beta}\sum_{i\omega_n}\sum_{s_1,s_2}\sum_{i_1,i_2}\sum_{\mathbf{q}} V^{s',s,s_1,s_2}_{i',i,i_1,i_2}(\mathbf{q})\sum_{s_3,s_4}\sum_{i_3,i_4}\sum_{\mathbf{k_1},\mathbf{k_2}} \mathcal{G}^{0;i_1,i_3}_{s_1,s_3}(\mathbf{k}+\mathbf{q};i\omega_n)\,\mathcal{G}^{i_2,i_4}_{s_2,s_4}(\mathbf{k}'-\mathbf{q};-i\omega_n)\,\Delta^{i_3,i_4}_{s_3,s_4}(\mathbf{k}+\mathbf{q},\mathbf{k}'-\mathbf{q}),$$

where we have used $\mathcal{F}^{i,i'}_{s,s'}(\mathbf{k},\mathbf{k}';\tau=0) = \frac{1}{\beta}\sum_{i\omega_n}\mathcal{F}^{i,i'}_{s,s'}(\mathbf{k},\mathbf{k}';i\omega_n)$.

At $T_c$, the first superconductivity mode is just starting to develop, such that the normal Green's function is not too different from the noninteracting one. Only as we lower the temperature below $T_c$ will we starting getting a significat contribution from superconductivity to the normal Green's function self-energy. Hence, near $T_c$, we approximate $\mathcal{G}$ by the noninteracting Green's function $\mathcal{G}^0$, and obtain the so-called linear gap equation given by

$$\Delta^{i,i'}_{s,s'}(\mathbf{k},\mathbf{k}') = -k_B T_c\sum_{i\omega_n}\sum_{s_1,s_2}\sum_{i_1,i_2}\sum_{\mathbf{q}} V^{s',s,s_1,s_2}_{i',i,i_1,i_2}(\mathbf{q})\sum_{s_3,s_4}\sum_{i_3,i_4}\sum_{\mathbf{k_1},\mathbf{k_2}} \mathcal{G}^{0;i_1,i_3}_{s_1,s_3}(\mathbf{k}+\mathbf{q};i\omega_n)\,\mathcal{G}^{0;i_2,i_4}_{s_2,s_4}(\mathbf{k}'-\mathbf{q};-i\omega_n)\,\Delta^{i_3,i_4}_{s_3,s_4}(\mathbf{k}+\mathbf{q},\mathbf{k}'-\mathbf{q}). \tag{2.23}$$

The linear gap equation is only dependent on the interaction coefficients and the noninteracting Green's function for our model. However, before we commit to solving equation (2.23) numerically for our models of interest, we must first do the Matsubara sum $\sum_{i\omega_n}$ analytically. The easiest way to go about this calculation is to first project the noninteracting Green's function into the eigenbasis of $\hat{H}_0$ and, only then, sum over the fermionic frequencies.

Let $\{|\lambda\rangle\}$ be an eigenbasis of $\hat{H}_0$ such that $\hat{H}_0|\lambda\rangle = \xi_\lambda|\lambda\rangle$, with $\{\xi_\lambda\}$ being the corresponding eigenvalues with the respect to the chemical potential. The matrix equation that defines the noninteracting Green's function in a general basis is

$$[i\omega_n\mathbb{1} - \mathbf{H}_0]\,\mathbf{G}^0(i\omega_n) = \mathbb{1}, \tag{2.24}$$

whose solution, in terms of the eigenbasis of $\mathbf{H}_0$, is just

$$\mathbf{G}^0(i\omega_n) = \sum_\lambda \frac{|\lambda\rangle\langle\lambda|}{i\omega_n - \xi_\lambda}, \tag{2.25}$$

and, since the linear gap equation (2.23) contains a product of two noninteracting Green's functions $\mathbf{G}^0(i\omega_n)\,\mathbf{G}^0(-i\omega_n)$, the Matsubara summation can be encapsulated in a single function defined as

$$\chi(\xi_\lambda,\xi_{\lambda'}) \equiv \frac{1}{\beta_c}\sum_{i\omega_n}\frac{1}{i\omega_n - \xi_\lambda}\frac{1}{i\omega_n + \xi_\lambda}, \tag{2.26}$$

where $\beta_c = \frac{1}{k_B T_c}$.

The Matsubara sum over the fermionic frequencies $i\omega_n$ can be performed as usual, by using contour integration and changing the problem of summing over $i\omega_n$ to that of computing the residues of the function $n_F(z)\, g(z) = \frac{n_F(z)}{(z-\xi_\lambda)(z+\xi_{\lambda'})}$, where $n_F(z) = \frac{1}{e^{\beta_c z}-1}$ is the Fermi-Dirac distribution function. The function $\frac{n_F(z)}{(z-\xi_\lambda)(z+\xi_{\lambda'})}$ has poles at $z = \xi_\lambda$ and $z = -\xi_{\lambda'}$, hence special care must be taken for the case when $\xi_\lambda = -\xi_{\lambda'}$, since the function will have a second order pole. Therefore, the $\chi$ function can be simply written as

$$\chi(\xi_\lambda, \xi_{\lambda'}) = \begin{cases} n_F'(\xi_\lambda) & ,\xi_{\lambda'} = -\xi_\lambda \\ \frac{n_F(\xi_\lambda) - n_F(-\xi_{\lambda'})}{\xi_\lambda + \xi_{\lambda'}} & ,\xi_{\lambda'} \neq -\xi_\lambda \end{cases} \tag{2.27}$$

## 2.4 Application to the homogeneous system

As a simple test of equation (2.23), we will try to obtain an analytical expression for the critical temperature of a simple system whose single-particle Hamiltonian has a single band (Which could be, for example, the electron gas). Assuming that the interaction has an atractive constant coupling $-g$ over a range of energies a Debye energy away from the Fermi surface, we can write the Hamiltonian for this model as

$$\hat{H} = \sum_{\mathbf{k},s} \xi(\mathbf{k})\, c^\dagger_{\mathbf{k},s} c_{\mathbf{k},s} - \frac{g}{2} \sum_s \sum_{\mathbf{k},\mathbf{k}',\mathbf{q}}{}' c^\dagger_{\mathbf{k}+\mathbf{q},s} c^\dagger_{\mathbf{k}'-\mathbf{q},-s} c_{\mathbf{k}',-s} c_{\mathbf{k},s},$$

where $\xi(\mathbf{k}) = \varepsilon(\mathbf{k}) - \mu$ and the $'$ over the sum indicates that we restrict the momentum exchange of the pairs such that $|\xi| \leq \omega_D$, meaning that we are choosing the interaction coefficients as

$$V^{s_1,s_2,s_3,s_4}_{i_1,i_2,i_3,i_4}(\mathbf{q}) = \delta_{s_1,s_4}\delta_{s_2,s_3}\delta_{s_1,-s_2} \begin{cases} -g & |\xi(\mathbf{q})| \leq \omega_D \\ 0 & |\xi(\mathbf{q})| > \omega_D \end{cases}. \tag{2.28}$$

In BCS theory, the Cooper pairs are formed with eletrons that have equal and opposite momenta and spin, such that $\Delta_{s,s'}(\mathbf{k},\mathbf{k}') = \Delta_{\uparrow\downarrow}(\mathbf{k},-\mathbf{k}) \equiv \Delta(\mathbf{k})$. We only need to consider the $\uparrow\downarrow$ pairing, since the form of the interaction coefficients (2.28) and the fact that the noninteracting Green's function is diagonal in spin assures us that only singlet superconductivity takes place in our BCS model. We can then write the linear gap equation for our model as

$$\Delta(\mathbf{k}) = \frac{g}{\beta_c} \sum_{\mathbf{q}}{}' \sum_{i\omega_n} \mathcal{G}^0(\mathbf{k}+\mathbf{q}; i\omega_n)\, \mathcal{G}^0(-\mathbf{k}-\mathbf{q}; -i\omega_n)\, \Delta(\mathbf{k}+\mathbf{q}). \tag{2.29}$$

The single particle Green's functions are already diagonal in the eigenbasis of $\hat{H}_0$ and can be written as

$$\mathcal{G}^0(\mathbf{k}; i\omega_n) = \frac{1}{i\omega_n - \xi(\mathbf{k})}, \tag{2.30}$$

so that

$$\begin{aligned}\Delta(\mathbf{k}) &= \frac{g}{\beta_c}\sum_{\mathbf{q}}{}'\sum_{i\omega_n}\frac{1}{i\omega_n-\xi(\mathbf{k}+\mathbf{q})}\frac{1}{-i\omega_n-\xi(-\mathbf{k}-\mathbf{q})}\Delta(\mathbf{k}+\mathbf{q})\\ &= -\frac{g}{\beta_c}\sum_{\mathbf{q}}{}'\sum_{i\omega_n}\frac{1}{(i\omega_n)^2-\xi^2(\mathbf{k}+\mathbf{q})}\Delta(\mathbf{k}+\mathbf{q})\end{aligned} \tag{2.31}$$

where in the last step of we used inversion symmetry, implying that the energy dispersion enjoys the property $\xi(\mathbf{k}) = \xi(-\mathbf{k})$. Using the result of Eq. (2.27) for the Matsubara sum, the linear gap equation for this simple model is

$$\begin{aligned}\Delta(\mathbf{k}) &= -g\sum_{\mathbf{q}}{}'\frac{n_F(\xi(\mathbf{k}+\mathbf{q}))-n_F(-\xi(\mathbf{k}+\mathbf{q}))}{2\xi(\mathbf{k}+\mathbf{q})}\Delta(\mathbf{k}+\mathbf{q}).\\ &= g\sum_{\mathbf{q}}{}'\frac{\tanh\left(\frac{\beta_c\xi(\mathbf{k}+\mathbf{q})}{2}\right)}{2\xi(\mathbf{k}+\mathbf{q})}\Delta(\mathbf{k}+\mathbf{q}).\end{aligned} \tag{2.32}$$

In order to obtain an analytical expression for the critical temperature, we can start by noticing that the right side of Eq. (2.32) is independent of $\mathbf{k}$ after making the change $\mathbf{q}\to\mathbf{q}-\mathbf{k}$, which implies that the gap parameter is also independent of momentum, i.e., $\Delta(\mathbf{k}) = \Delta$. If we are searching for a non-zero solution of the gap parameter for a finite temperature, then $\Delta$ can be factored out of Eq. (2.32). Finally, we assume that the density of states (DOS) varies slowly within the Debye energy window centered at the Fermi energy. We can then replace the sum $\sum_{\mathbf{q}}{}'$ by an integral over energies in the Debye window and factor the DOS as a constant.

$$\begin{aligned}\Delta &= g\sum_{\mathbf{k}}{}'\frac{\tanh\left(\frac{\beta_c\xi(\mathbf{k})}{2}\right)}{2\xi(\mathbf{k})}\Delta\\ 1 &\approx g\rho(0)\int_0^{\frac{1}{2\theta_c}}dx\,\frac{\tanh(x)}{x},\end{aligned} \tag{2.33}$$

where $\theta_c \equiv \frac{k_B T_c}{\omega_D}$. Integrating the right side of Eq. (2.33) by parts, we get

$$\frac{1}{g\rho(0)} = \ln(x)\tanh(x)\Big|_0^{\frac{1}{2\theta_c}} - \int_0^{\frac{1}{2\theta_c}}dx\,\ln(x)\,sech^2(x). \tag{2.34}$$

If we assume that in the weak-coupling limit $\theta_c \ll 1$, i.e., the critical temperature is much smaller than the Debye temperature, we can do the integral in Eq. (2.34) analytically, arriving at

$$\frac{1}{g\rho(0)} \approx \ln\left(\frac{1}{2\theta_c}\right) - \ln\left(\frac{\pi}{4}\right) + \gamma, \tag{2.35}$$

where $\gamma \approx 0.577$ is the Euler–Mascheroni constant. Inverting equation (2.35) for $T_c$, we get

$$T_c = \frac{2\omega_D}{\pi k_B} e^{\gamma} e^{-\frac{1}{g\rho(0)}}. \tag{2.36}$$

Equation (2.36) is the well known BCS formula for the critical temperature of an homogeneous superconductor in the weak-coupling limit. Its scaling behaviour with the coupling constant $g$, $T_c \sim e^{-\frac{1}{g\rho(0)}}$, will be of importance later on.

## 2.5 Anderson time-reversal pairing approximation

Since we wish to study systems which exhibit quasiperiodicity, where the momentum space treatment is no longer adequate, we will necessarily need to compute the linear gap equation in real space. As we will discuss below, this significantly limits the maximum size of the systems we can efficiently study numerically. Therefore, in this section we will present an approximation of the linear gap equation which is a much more efficient alternative.

With the study of incommensurate systems in mind, we will consider a general tight-binding Hamiltonian written in real space

$$\hat{H} = \hat{H}_0 + \frac{1}{2} \sum_s \sum_{i,j,k,l} V_{i,j,k,l} c^\dagger_{i,s} c^\dagger_{j,-s} c_{k,-s} c_{l,s}. \tag{2.37}$$

The interaction term in Eq. (2.37) differs from the one previously considered (2.3), since it does not depend on momentum and conserves spin. The whole system can be thought as being made up of, essentially, just one big unit cell with $L$ lattice sites. Within this interpretation, the labels $\{i,j,k,l\}$ now encompass all lattice sites.

The linear gap equation in Eq. (2.23), for singlet BCS superconductivity with the Hamiltonian given by (2.37), can be written in the lattice basis as

$$\Delta^{i,j} = -\frac{1}{\beta_c} \sum_{i\omega_n} \sum_{i_1,i_2} V_{j,i,i_1,i_2} \sum_{i_3,i_4} \mathcal{G}^0_{i_1,i_3}(i\omega_n)\, \mathcal{G}^0_{i_2,i_4}(-i\omega_n)\, \Delta^{i_3,i_4}, \tag{2.38}$$

and, projecting the noninteracting Green's function (2.25) written in the eigenbasis of $\hat{H}_0$ onto the real space lattice basis $\{i\}$, we get

$$\mathcal{G}^0_{i,j}(i\omega_n) = \sum_\lambda \frac{\langle i \mid \lambda\rangle \langle \lambda \mid j\rangle}{i\omega_n - \xi_\lambda} = \sum_\lambda \frac{\phi^\lambda_i \phi^{\lambda,*}_j}{i\omega_n - \xi_\lambda},$$

where $\phi^\lambda_i \equiv \langle i \mid \lambda\rangle$. Therefore, the linear gap equation (2.38) can be rewritten as

$$\begin{aligned}\Delta^{i,j} &= \frac{1}{\beta_c} \sum_{i\omega_n} \sum_{i_1,i_2} V_{j,i,i_1,i_2} \sum_{i_3,i_4} \sum_{\lambda,\lambda'} \frac{\phi^\lambda_{i_1} \phi^{\lambda,*}_{i_3}}{i\omega_n - \xi_\lambda} \frac{\phi^{\lambda'}_{i_2} \phi^{\lambda',*}_{i_4}}{i\omega_n + \xi_{\lambda'}} \Delta^{i_3,i_4} \\ &= \sum_{i_1,i_2} V_{j,i,i_1,i_2} \sum_{i_3,i_4} \sum_{\lambda,\lambda'} \chi(\xi_\lambda, \xi_{\lambda'})\, \phi^\lambda_{i_1} \phi^{\lambda,*}_{i_3} \phi^{\lambda'}_{i_2} \phi^{\lambda',*}_{i_4} \Delta^{i_3,i_4},\end{aligned} \tag{2.39}$$

with the Matsubara summation resulting in the $\chi$ function given by Eq. (2.27).

Let us now consider an Hamiltonian with a $s$-wave singlet interaction term, than favors the formation of Cooper pairs on the same lattice site with opposite spin, given by

$$\hat{H}_{int} = -\frac{g_1}{2}\sum_{\sigma,i} c^{\dagger}_{i,\sigma} c^{\dagger}_{i,-\sigma} c_{i,-\sigma} c_{i,\sigma}, \tag{2.40}$$

with a constant coupling coefficient $g_1$. Going back to Eq. (2.39), we can write down the simplified linear gap equation as

$$\Delta^i = -g_1 \sum_j \sum_{\lambda,\lambda'} \chi\left(\xi_\lambda, \xi_{\lambda'}\right) \phi_i^{\lambda} \phi_j^{\lambda,*} \phi_i^{\lambda'} \phi_j^{\lambda',*} \Delta^j, \tag{2.41}$$

where only on-site pairing $\Delta^i = \frac{g_1}{2}\left\langle c_{i\uparrow} c_{i\downarrow}\right\rangle$ occurs, due to the form of the interaction coefficients $V_{i,j,k,l} = -g_1 \delta_{i,j}\delta_{i,k}\delta_{i,l}$.

To solve equation (2.41) numerically, we need to compute the elements and diagonalize the matrix

$$\Omega_{i,j} = -g_1 \sum_{\lambda,\lambda'} \chi\left(\xi_\lambda, \xi_{\lambda'}\right) \phi_i^{\lambda} \phi_j^{\lambda,*} \phi_i^{\lambda'} \phi_j^{\lambda',*}, \tag{2.42}$$

and if $L$ is the dimension of the eigenspace of $\hat{H}_0$ then the $\Omega$ matrix construction computational time is $O\left(L^4\right)$, given that there are $L^2$ elements and each elements requires a double sum over all the eigenvalues indices (if there is no $\omega_D$ energy restriction). By contrast, its diagonalization is only $O\left(L^3\right)$, so that the matrix construction is the bottleneck in this computation. Our aim in this section is to introduce an approximation into our linear gap equation approach that reduces this computational cost.

In the spirit of the Anderson time-reversal pairing approximation originally proposed in the context of the theory of dirty superconductors [44], we will only consider the pairing interaction between time-reversed eigenstates of the noninteracting system, which is a good aproximation to study $T_c$ in the weak coupling limit, as we will show later.

If $d^{\dagger}_{\lambda,\sigma}|0\rangle = \left|\psi_{\lambda,\sigma}\right\rangle$ is the basis that diagonalizes $\hat{H}_0$ such that

$$\hat{H}_0 = \sum_{\lambda,\sigma} \xi_\lambda d^{\dagger}_{\lambda,\sigma} d_{\lambda,\sigma}, \tag{2.43}$$

we can then do a change of basis $c^{\dagger}_i = \sum_\lambda \phi_i^{\lambda,*} d^{\dagger}_{\lambda}$ and transform the full Hamiltonian into the eigenbasis of $\hat{H}_0$

$$\hat{H} = \hat{H}_0 - \frac{g_1}{2}\sum_{\sigma,i}\sum_{\lambda_1,\lambda_2,\lambda_3,\lambda_4} \phi_i^{\lambda_1,*}\phi_i^{\lambda_2,*}\phi_i^{\lambda_3}\phi_i^{\lambda_4} d^{\dagger}_{\lambda_1,\sigma} d^{\dagger}_{\lambda_2,-\sigma} d_{\lambda_3,-\sigma} d_{\lambda_4,\sigma}. \tag{2.44}$$

We will only be pairing the time-reversed states, which for $\hat{H}_0$ independent of spin amounts to pairing $\left|\psi_{\lambda,\sigma}\right\rangle$ with its complex conjugate, and this truncation of the Hamiltonian results in

$$\hat{H}' = \hat{H}_0 - \frac{g_1}{2}\sum_{\sigma}\sum_{\lambda,\lambda'} M_{\lambda,\lambda'} d^{\dagger}_{\lambda,\sigma} d^{\dagger}_{\lambda,-\sigma} d_{\lambda',-\sigma} d_{\lambda',\sigma} \tag{2.45}$$

where

$$M_{\lambda,\lambda'} \equiv \sum_i \left|\phi_i^{\lambda}\right|^2 \left|\phi_i^{\lambda'}\right|^2 \tag{2.46}$$

is the matrix that approximately encodes the structure of the noninteracting wave functions in our reduced linear gap equation. The great advantage of this $M$-matrix formulation is that its computation time is of time complexity $O\left(L^3\right)$, due to the assumption of diagonal pairing, which means that each element in the matrix involves a single sum of the dimensionality of our eigenspace. This is a great improvement over the time complexity $O\left(L^4\right)$ of the matrix in Eq. (2.42).

In the eigenbasis of $\hat{H}_0$, $\left\{d_{\lambda,\sigma}^{\dagger}\right\}$, if we recall the definition (2.20), the superconductor gap parameter is just

$$\begin{aligned}\Delta^{\lambda,\lambda'} &= -\sum_{\eta,\eta'} V_{\lambda',\lambda,\eta,\eta'} \left\langle d_{\eta\uparrow} d_{\eta'\downarrow}\right\rangle \\ &= \delta_{\lambda,\lambda'} \frac{g}{2} \sum_{\eta} M_{\lambda,\eta} \left\langle d_{\eta\uparrow} d_{\eta\downarrow}\right\rangle .\end{aligned} \tag{2.47}$$

Therefore, the truncation of the Hamiltonian by pairing time-reversed states leads to a diagonal pairing in the eigenbasis of the bilinear Hamiltonian. It is only natural to simplify notation and define

$$\Delta^{\lambda} \equiv \Delta^{\lambda,\lambda} = \frac{g}{2} \sum_{\eta} M_{\lambda,\eta} \left\langle d_{\eta\uparrow} d_{\eta\downarrow}\right\rangle . \tag{2.48}$$

The linear gap equation for the diagonal gap parameter $\Delta^{\lambda}$ is then given by

$$\begin{aligned}\Delta^{\lambda} &= \frac{g}{\beta_c} \sum_{i\omega_n} \sum_{\lambda'} M_{\lambda,\lambda'} \mathcal{G}_{\lambda'}^{0}\left(i\omega_n\right) \mathcal{G}_{\lambda'}^{0}\left(-i\omega_n\right) \Delta^{\lambda'} \\ &= -\frac{g}{\beta_c} \sum_{\lambda'} M_{\lambda,\lambda'} \sum_{i\omega_n} \frac{1}{i\omega_n - \xi_{\lambda'}} \frac{1}{i\omega_n + \xi_{\lambda'}} \Delta^{\lambda'},\end{aligned} \tag{2.49}$$

and summing over the Matsubara's frequencies as we did before to obtain Eq. (2.27), we get

$$\Delta^{\lambda} = g \sum_{\lambda'} M_{\lambda,\lambda'} \frac{\tanh\left(\frac{\xi_{\lambda'}\beta}{2}\right)}{2\xi_{\lambda'}} \Delta^{\lambda'} . \tag{2.50}$$

Solving the time-reversal pairing linear gap equation (Anderson linear gap equation) (2.50), gets us the gap parameters $\left\{\Delta^{\lambda}\right\}$ in the eigenbasis of $\hat{H}_0$. However, if we wish to study the localization properties of the superconductor local parameters in real space we need to compute the gap parameters in the lattice basis $\left\{\Delta^{i}\right\}$. For the interaction Hamiltonian (2.40), our gap parameter in the lattice basis takes a very simple form and is given by

$$\Delta^{i} = \frac{g}{2} \left\langle c_{i\uparrow} c_{i\downarrow}\right\rangle . \tag{2.51}$$

The first step in getting an equation that relates $\Delta^{i}$ to $\Delta^{\lambda}$ is to do a change of basis at the level of the $c$-operators in equation (2.51),

$$\begin{aligned}\Delta^i &= \frac{g_1}{2}\left\langle c_{i\uparrow}c_{i\downarrow}\right\rangle \\ &= \frac{g_1}{2}\left\langle \sum_\lambda \phi_i^\lambda d_{\lambda\uparrow}\sum_{\lambda'}\phi_i^{\lambda'}d_{\lambda'\downarrow}\right\rangle \\ &= \frac{g_1}{2}\sum_{\lambda,\lambda'}\phi_i^\lambda\phi_i^{\lambda,*}\left\langle d_{\lambda\uparrow}d_{\lambda\downarrow}\right\rangle\delta_{\lambda',\lambda} \\ &= \frac{g_1}{2}\sum_\lambda\left|\phi_i^\lambda\right|^2\left\langle d_{\lambda\uparrow}d_{\lambda\downarrow}\right\rangle. \end{aligned} \tag{2.52}$$

Equation (2.52) expresses $\Delta^i$ in terms of the anomalous expectation value $\left\langle d_{\lambda\uparrow}d_{\lambda\downarrow}\right\rangle$. We just need to write $\left\langle d_{\lambda\uparrow}d_{\lambda\downarrow}\right\rangle$ in terms of $\Delta^\lambda$, which can be achieved by looking at the equation of motion of the anomalous Green's function close to the critical temperature. Recalling the equation of motion in Eq. (2.22), we can write it in the eigenbasis of $\hat{H}_0$, where $\Delta^{\eta,\eta'}$ is diagonal, as

$$\begin{aligned}\mathcal{F}^{\lambda,\lambda'}(i\omega_n) &= \sum_{\eta,\eta'}\mathcal{G}^0_{\lambda,\eta}(i\omega_n)\,\mathcal{G}_{\lambda',\eta'}(-i\omega_n)\,\Delta^\eta\delta_{\eta,\eta'} \\ &= \sum_\eta \mathcal{G}^0_{\lambda,\eta}(i\omega_n)\,\mathcal{G}_{\lambda',\eta}(-i\omega_n)\,\Delta^\eta. \end{aligned} \tag{2.53}$$

To make contact with the linear gap equation, we consistently approximate $\mathcal{G}$ by $\mathcal{G}^0$ near $T_c$. Using this and the fact that noninteracting Green's function is diagonal in this basis $\mathcal{G}^0_{\lambda,\eta} = \delta_{\lambda,\eta}\mathcal{G}^0_\lambda$,

$$\begin{aligned}\mathcal{F}^{\lambda,\lambda'}(i\omega_n) &= \sum_\eta \delta_{\lambda,\eta}\delta_{\lambda',\eta}\mathcal{G}^0_\lambda(i\omega_n)\,\mathcal{G}^0_{\lambda'}(-i\omega_n)\,\Delta^\eta \\ &= \delta_{\lambda,\lambda'}\mathcal{G}^0_\lambda(i\omega_n)\,\mathcal{G}^0_{\lambda'}(-i\omega_n)\,\Delta^{\lambda'}, \end{aligned} \tag{2.54}$$

hence

$$\mathcal{F}^\lambda(i\omega_n) \equiv \mathcal{F}^{\lambda,\lambda}(i\omega_n) = \mathcal{G}^0_\lambda(i\omega_n)\,\mathcal{G}^0_\lambda(-i\omega_n)\,\Delta^\lambda. \tag{2.55}$$

Equation (2.55) gives the anomalous Green's function in fermionic frequency domain as a function of the noninteracting Green's function and the superconductor gap parameter in the eigenbasis of $\hat{H}_0$ obtained self-consistently from the linear gap equation (2.50). The anomalous expection value we are interested in is just

$$\left\langle d_{\lambda\uparrow}d_{\lambda\downarrow}\right\rangle = \mathcal{F}^\lambda(\tau=0) = \frac{1}{\beta_c}\lim_{\tau\to0^+}\sum_{i\omega_n}\mathcal{F}^\lambda(i\omega_n)\,e^{-i\omega_n\tau},$$

which after the usual Matsubara summation is just

$$\left\langle d_{\lambda\uparrow}d_{\lambda\downarrow}\right\rangle = \frac{\tanh\left(\frac{\xi_\lambda\beta_c}{2}\right)}{2\xi_\lambda}\Delta^\lambda, \tag{2.56}$$

where $\beta_c$ is computed from the eigenvalues of (2.50). Inserting the result of equation (2.56) into (2.52), we

finally obtain

$$\Delta^i = \frac{g_1}{2} \sum_\lambda \left|\phi_i^\lambda\right|^2 \frac{\tanh\left(\frac{\xi_\lambda \beta_c}{2}\right)}{2\xi_\lambda} \Delta^\lambda. \tag{2.57}$$

We will employ equation (2.57) when we wish to study the localization properties of the superconductor local parameters within the time-reversal pairing approximation.

# Chapter 3

# Superconductivity in single layer graphene

Since we wish to study superconductivity in the tBLG, it is important to first understand the results of the linear gap equation for the graphene monolayer, given that it is the building block of tBLG. The following chapter is devoted to studying the linear gap equation, formulated both in momentum and in real space, for a tight-binding model of the single layer graphene (SLG).

## 3.1 Model

### 3.1.1 Lattice structure

The graphene lattice is an honeycomb lattice, i.e., a triangular Bravais lattice with two sublattices, which we will call $A$ and $B$. The Bravais lattice is generated by a set of discrete translation operations described by the vectors

$$\mathbf{R} = n\mathbf{a}_1 + m\mathbf{a}_2, \tag{3.1}$$

where $n, m$ are integers. We choose the primitive vectors to be

$$\begin{aligned} \mathbf{a}_1 &= \frac{1}{2}\left(\sqrt{3}, 3\right), \\ \mathbf{a}_2 &= \frac{1}{2}\left(-\sqrt{3}, 3\right), \end{aligned} \tag{3.2}$$

with the carbon-carbon distance set to $a = 1$ for numerical purposes. The basis vectors are

$$\begin{aligned} \mathbf{d}_A &= (0,0), \\ \mathbf{d}_B &= (0,1), \end{aligned} \tag{3.3}$$

and the vectors which connect an $A$ site to its nearest-neighbors in sublattice $B$ are given by

$$\begin{aligned}\boldsymbol{\tau}_1 &= (0,1)\,,\\ \boldsymbol{\tau}_2 &= \frac{1}{2}\left(-\sqrt{3},-1\right),\\ \boldsymbol{\tau}_3 &= \frac{1}{2}\left(\sqrt{3},-1\right).\end{aligned} \tag{3.4}$$

The reciprocal lattice for graphene is also a triangular Bravais lattice and its primitive vectors are

$$\begin{aligned}\mathbf{b}_1 &= 2\pi\left(\frac{1}{\sqrt{3}},\frac{1}{3}\right),\\ \mathbf{b}_2 &= 2\pi\left(-\frac{1}{\sqrt{3}},\frac{1}{3}\right),\end{aligned} \tag{3.5}$$

given our choice of real-space lattice vectors in (3.2).

The Brillouin Zone (BZ) forms an hexagon rotated in relation to the real-space unit cell. The most important high symmetry points in the BZ are the Dirac points

$$\begin{aligned}\boldsymbol{K} &= \frac{2\pi}{3}\left(\frac{1}{\sqrt{3}},1\right),\\ \boldsymbol{K}' &= -\boldsymbol{K},\end{aligned} \tag{3.6}$$

along with its equivalent points obtained with translations by vectors of the reciprocal lattice, and the points

$$\begin{aligned}\Gamma &= (0,0)\,,\\ \boldsymbol{M} &= \left(0,\frac{2\pi}{3}\right).\end{aligned} \tag{3.7}$$

### 3.1.2 Single-particle Hamiltonian

The nearest-neighbor tight-binding Hamiltonian for SLG is

$$\hat{H}_0 = -t\sum_{\mathbf{R},\boldsymbol{\tau}_i,\sigma}\left[b^\dagger_{\mathbf{R}+\boldsymbol{\tau}_i,\sigma}a_{\mathbf{R},\sigma} + a^\dagger_{\mathbf{R},\sigma}b_{\mathbf{R}+\boldsymbol{\tau}_i,\sigma}\right], \tag{3.8}$$

where $a^\dagger_{\mathbf{R},\sigma}\left(b^\dagger_{\mathbf{R},\sigma}\right)$ creates an eletron at position $\mathbf{R}$ in the sublattice $A\,(B)$ with spin $\sigma \in \{\uparrow,\downarrow\}$. This Hamiltonian can be easily diagonalized by the introduction of Bloch states, which is equivalent to doing a Fourier transformation of the second quantization operators,

$$\begin{aligned}a^\dagger_{\mathbf{R},\sigma} &= \frac{1}{N}\sum_{\mathbf{k}} e^{-i\mathbf{k}\cdot\mathbf{R}}a^\dagger_{\mathbf{k},\sigma},\\ b^\dagger_{\mathbf{R},\sigma} &= \frac{1}{N}\sum_{\mathbf{k}} e^{-i\mathbf{k}\cdot\mathbf{R}}b^\dagger_{\mathbf{k},\sigma},\end{aligned} \tag{3.9}$$

where $N$ is the number of unit cells along the $\mathbf{a}_1$ or the $\mathbf{a}_2$ direction. Therefore, the SLG Hamiltonian is written as

$$\hat{H}_0 = -t \sum_{\mathbf{k},\sigma} \left[ f^*_{\mathbf{k}} b^\dagger_{\mathbf{k},\sigma} a_{\mathbf{k},\sigma} + f_{\mathbf{k}} a^\dagger_{\mathbf{k},\sigma} b_{\mathbf{k},\sigma} \right], \tag{3.10}$$

given the identity $\sum_{\mathbf{R}} e^{i(\mathbf{k}'-\mathbf{k})\cdot\mathbf{R}} = N^2 \delta_{\mathbf{k},\mathbf{k}'}$ and having defined

$$f_{\mathbf{k}} \equiv \sum_{\boldsymbol{\tau}_j} e^{-i\mathbf{k}\cdot\boldsymbol{\tau}_j}. \tag{3.11}$$

Writing the anhilation operators as a column vector

$$\Psi_{\mathbf{k},\sigma} \equiv \begin{pmatrix} a_{\mathbf{k},\sigma} \\ b_{\mathbf{k},\sigma} \end{pmatrix}, \tag{3.12}$$

we can rewrite the SLG Hamiltonian as

$$\hat{H}_0 = \sum_{\mathbf{k},\sigma} \Psi^\dagger_{\mathbf{k},\sigma} h(\mathbf{k}) \Psi_{\mathbf{k},\sigma}, \tag{3.13}$$

where the Bloch matrix is

$$h(\mathbf{k}) \equiv -t \begin{pmatrix} 0 & f_{\mathbf{k}} \\ f^*_{\mathbf{k}} & 0 \end{pmatrix}. \tag{3.14}$$

In the numerical results that follow, we will always take $t = 1$. In other words, all energies (the thermal energy $k_B T_c$, the chemical potential $\mu$, etc.) will be in units of $t$.

The eigenvalues of the matrix (3.14) are simply

$$\varepsilon(\mathbf{k}) = \pm\sqrt{f_{\mathbf{k}} f^*_{\mathbf{k}}}, \tag{3.15}$$

and the eigenvectors can be written in terms of the phase of $f_{\mathbf{k}}$, $\phi(\mathbf{k})$, allowing us to write the change from the sublattice basis $\{|A,\mathbf{k}\rangle, |B,\mathbf{k}\rangle\}$ to the $h(\mathbf{k})$ eigenbasis $\{|+,\mathbf{k}\rangle, |-,\mathbf{k}\rangle\}$ as

$$\begin{aligned} |+,\mathbf{k}\rangle &= \frac{1}{\sqrt{2}} \left[ e^{i\phi(\mathbf{k})/2} |A,\mathbf{k}\rangle + e^{-i\phi(\mathbf{k})/2} |B,\mathbf{k}\rangle \right] \\ |-,\mathbf{k}\rangle &= \frac{1}{\sqrt{2}} \left[ e^{i\phi(\mathbf{k})/2} |A,\mathbf{k}\rangle - e^{-i\phi(\mathbf{k})/2} |B,\mathbf{k}\rangle \right], \end{aligned} \tag{3.16}$$

where $|A,\mathbf{k}\rangle = a^\dagger_{\mathbf{k}} |0\rangle$ and $|B,\mathbf{k}\rangle = b^\dagger_{\mathbf{k}} |0\rangle$.

If we do a small momentum expansion of the energy dispersion in Eq. (3.15) around the **K**-point, we conclude that the dispersion is linear, i.e., we get $\varepsilon(\mathbf{K}+\mathbf{q}) \sim |\mathbf{q}|$. Due to this linear behaviour, we say that the energy dispersion has a Dirac cone at the **K**-point. We can see the Dirac cone in Fig. (3.1a), along with the vanishing density of states at the Dirac energy in Fig. (3.1b). Another interesting behaviour of the band structure of graphene is the existence of saddle points at the ***M***-points, which lead to van Hove singularities at $\varepsilon = \pm 1$, as seen in Fig. (3.1b).

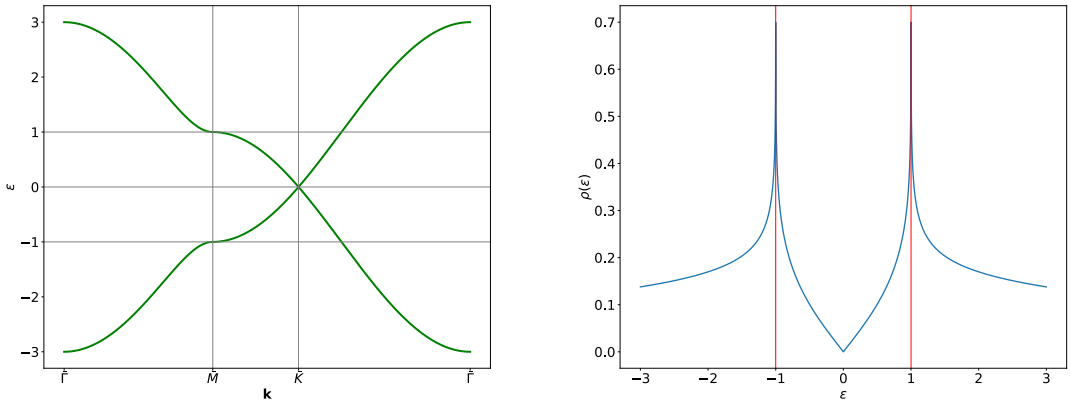


(a) (b)

Figure 3.1: The energy dispersion $\varepsilon(\mathbf{k})$ of Eq. (3.15) and the corresponding density of states (per spin) for single layer graphene. $(a)$ $\varepsilon(\mathbf{k})$ along the path $\Gamma \to \boldsymbol{M} \to \boldsymbol{K} \to \Gamma$ in the first BZ of graphene. The upper and lower bands touch linearly in the Dirac cone at $\boldsymbol{K}$. $(b)$ Density of states (per spin) $\rho(\varepsilon)$. The van Hove singularities are marked as vertical lines at $\varepsilon = \pm 1$.

### 3.1.3 Interaction Hamiltonian

Having summarized some properties of the noninteracting Hamiltonian of SLG, we can turn to the choice of the interacting model. We will consider an Hamiltonian with a BCS interaction term that favors Cooper pairs on the same lattice site with coupling constant $g_1$ and another term which couples nearest-neighbor (NN) lattice sites with coupling constant $g_2$,

$$\hat{H}_{int} = \hat{H}_L + \hat{H}_{NN} = -\frac{g_1}{2}\sum_{s,i,\mathbf{R}} c^\dagger_{\mathbf{R},i,s} c^\dagger_{\mathbf{R},i,-s} c_{\mathbf{R},i,-s} c_{\mathbf{R},i,s} - \frac{g_2}{2}\sum_{s}\sum_{j\neq i}\sum_{\mathbf{R},\boldsymbol{\tau}_k} c^\dagger_{\mathbf{R}+\boldsymbol{\tau}_k,j,s} c^\dagger_{\mathbf{R},i,-s} c_{\mathbf{R},i,-s} c_{\mathbf{R}+\boldsymbol{\tau}_k,j,s}, \tag{3.17}$$

where $c^\dagger_{\mathbf{R},i,\sigma}$ creates an eletron at site $\mathbf{R}$ in the sublattice $i$ with spin $s$. This is just an extended Hubbard model with attractive on-site and nearest-neighbor interactions.

## 3.2 Momentum space linear gap equation

In order to use equation (2.23) in momentum space, we have to write the Hamiltonian of our model (3.17) in the momentum space canonical form of equation (2.3). We start by Fourier transforming the operators in the interaction terms of the Hamiltonian. The on-site BCS term is simply

$$\hat{H}_L = -\frac{g_1}{2}\sum_{s,i}\sum_{\mathbf{k},\mathbf{k}',\mathbf{q}} c^\dagger_{\mathbf{k}+\mathbf{q},s,i} c^\dagger_{\mathbf{k}'-\mathbf{q},-s,i} c_{\mathbf{k}',-s,i} c_{\mathbf{k},s,i}, \tag{3.18}$$

while the nearest-neighbor term is

$$\hat{H}_{NN} = -\frac{g_2}{2} \sum_s \sum_{j \neq i} \sum_{\mathbf{k},\mathbf{k}',\mathbf{q}} f_{i,j}(\mathbf{q})\, c^\dagger_{\mathbf{k}+\mathbf{q},j,s} c^\dagger_{\mathbf{k}'-\mathbf{q},i,-s} c_{\mathbf{k}',i,-s} c_{\mathbf{k},j,s}, \tag{3.19}$$

where

$$f_{j,i}(-\mathbf{q}) = f^*_{j,i}(\mathbf{q}) = f_{i,j}(\mathbf{q}) \equiv \sum_\tau e^{-i\gamma_{i,j}\boldsymbol{\tau}\cdot\mathbf{q}} \left(1 - \delta_{i,j}\right), \tag{3.20}$$

with $\gamma_{A,B} = 1$ and $\gamma_{B,A} = -1$. The full Hamiltonian for our model is now in the canonical form of equation (2.3), and we can identify the interaction coefficients as

$$V^{s_1,s_2,s_3,s_4}_{i_1,i_2,i_3,i_4}(\mathbf{q}) = \delta_{s_1,s_4}\delta_{s_2,s_1}\delta_{s_2,-s_1} \begin{cases} -g_1 & i_1,i_2,i_3,i_4 = i \\ -g_2 f_{i,j}(\mathbf{q}) & i_1 = i_4 = j \neq i = i_2 = i_3 \end{cases}. \tag{3.21}$$

With the choice of interaction coefficients in Eq. (3.21), the linear gap equation in momentum space assumes a simple $4\times4$ sublattice structure,

$$\begin{aligned} \Delta^{i,i}(\mathbf{k}) &= \frac{g_1}{\beta_c} \sum_{\mathbf{k}'} \sum_{m,n} \sum_{i\omega_n} \mathcal{G}^0_{i,m}(\mathbf{k}';i\omega_n)\, \mathcal{G}^0_{i,n}(-\mathbf{k}';-i\omega_n)\, \Delta^{m,n}(\mathbf{k}') \\ \Delta^{i,j}(\mathbf{k}) &= \frac{g_2}{\beta_c} \sum_{\mathbf{k}'} f_{i,j}(\mathbf{k}'-\mathbf{k}) \sum_{m,n} \sum_{i\omega_n} \mathcal{G}^0_{i,m}(\mathbf{k}';i\omega_n)\, \mathcal{G}^0_{j,n}(-\mathbf{k}';-i\omega_n)\, \Delta^{m,n}(\mathbf{k}'), \qquad j \neq i. \end{aligned} \tag{3.22}$$

and we once again we assumed singlet BCS superconductivity. With the inclusion of the nearest-neighbor interaction term, we could have other types of superconductivity, but we will always restrict ourselves to the study of singlet superconductivity. Recalling the general procedure we employed in Section 2.3 to deal with the Matsubara summation, we start by writing the noninteracting Green's function in the eigenbasis of $\mathbf{H}_0$,

$$\mathbf{G}^0(\mathbf{k},i\omega_n) = \sum_\lambda \frac{|\lambda\rangle\langle\lambda|}{i\omega_n - \xi_\lambda(\mathbf{k})}, \tag{3.23}$$

where $\lambda \in \{+,-\}$ is the band index, i.e., the eigenbasis index of the Bloch Hamiltonian. Projeting the Green's function (3.23) into the sublattice basis, we get

$$\mathcal{G}^0_{i,i'}(\mathbf{k},i\omega_n) = \sum_\lambda \frac{u^\lambda_i(\mathbf{k})\, u^{\lambda,*}_{i'}(\mathbf{k})}{i\omega_n - \xi_\lambda(\mathbf{k})}, \tag{3.24}$$

with $u^\lambda_i(\mathbf{k}) = \langle i \mid \lambda\rangle(\mathbf{k})$. Substituting (3.24) into equation (3.22), we obtain

$$\Delta^{i,i}(\mathbf{k}) = -g_1 \sum_{\mathbf{k}'} \sum_{m,n} \Gamma_{i,i}^{m,n}(\mathbf{k}) \Delta^{m,n}(\mathbf{k}')$$
$$\Delta^{i,j}(\mathbf{k}) = -g_2 \sum_{\mathbf{k}'} f_{i,j}(\mathbf{k}'-\mathbf{k}) \sum_{m,n} \Gamma_{i,j}^{m,n}(\mathbf{k}) \Delta^{m,n}(\mathbf{k}'), \qquad j \neq i. \tag{3.25}$$

where the $\Gamma$ function is defined as

$$\Gamma_{i,j}^{m,n}(\mathbf{k}) \equiv \sum_{\lambda,\lambda'} \chi(\varepsilon_\lambda(\mathbf{k}), \varepsilon_{\lambda'}(\mathbf{k})) u_i^\lambda(\mathbf{k}) u_m^{\lambda,*}(\mathbf{k}) u_j^{\lambda'}(-\mathbf{k}) u_n^{\lambda',*}(-\mathbf{k}), \tag{3.26}$$

with the Matsubara sum given by

$$\chi(\varepsilon_\lambda(\mathbf{k}), \varepsilon_{\lambda'}(\mathbf{k})) = \frac{1}{\beta_c} \sum_{i\omega_n} \frac{1}{i\omega_n - \xi_\lambda(\mathbf{k}')} \frac{1}{i\omega_n + \xi_\lambda(-\mathbf{k}')}, \tag{3.27}$$

in agreement with the general definition (2.26).

The next crucial step is, of course, the Matsubara summation itself. With this goal in mind, we exploit the symmetry of $\xi_\lambda(\mathbf{k})$. If $\lambda \in \{+,-\}$,then $\xi_\lambda(\mathbf{k}) = \lambda\varepsilon(\mathbf{k}) - \mu$, where $\varepsilon(-\mathbf{k}) = \varepsilon(\mathbf{k}) \equiv |\varepsilon_\lambda(\mathbf{k})|$. Using the general result of Eq. (2.27), we may then write

$$\chi(\varepsilon_+(\mathbf{k}), \varepsilon_+(\mathbf{k})) = -\frac{tanh\left(\frac{\beta_c[\varepsilon(\mathbf{k})-\mu]}{2}\right)}{2[\varepsilon(\mathbf{k})-\mu]} \tag{3.28}$$
$$\chi(\varepsilon_-(\mathbf{k}), \varepsilon_-(\mathbf{k})) = -\frac{tanh\left(\frac{\beta_c[\varepsilon(\mathbf{k})+\mu]}{2}\right)}{2[\varepsilon(\mathbf{k})+\mu]} \tag{3.29}$$
$$\chi(\varepsilon_+(\mathbf{k}), \varepsilon_-(\mathbf{k})) = \frac{1}{2\mu}[n_F(\varepsilon(\mathbf{k})+\mu) - n_F(\varepsilon(\mathbf{k})-\mu)] \tag{3.30}$$
$$\chi(\varepsilon_-(\mathbf{k}), \varepsilon_+(\mathbf{k})) = \frac{1}{2\mu}[n_F(-\varepsilon(\mathbf{k})+\mu) - n_F(-\varepsilon(\mathbf{k})-\mu)], \tag{3.31}$$

with the caveat that when $\mu = 0$ then Eqs. 3.30 and 3.31 must take the form $n_F'(\varepsilon(\mathbf{k}))$ and $n_F'(-\varepsilon(\mathbf{k}))$, respectively, due to the second-order nature of the poles when we do the Matsubara summation.

Finally, we compute the coefficients $\Gamma_{i,j}^{m,n}(\mathbf{k})$ by doing the sum over the eigenstates of the Bloch Hamiltonian (3.14). The explicit form of all $\Gamma$ coefficients in terms of the $\chi$'s and the Bloch eigenfunctions $u(\mathbf{k})$ can be found in Appendix C.

Having overcome the minutiae of the previous calculation, we are now in a position to write the final form of our linear gap equation for SLG in momentum space. This form is able to emphasize the sublattice structure of the equation that we will only be able to solve numerically and takes the simple matrix form given by

$$\begin{pmatrix} \Delta^{A,A}(\mathbf{k}') \\ \Delta^{A,B}(\mathbf{k}') \\ \Delta^{B,A}(\mathbf{k}') \\ \Delta^{B,B}(\mathbf{k}') \end{pmatrix} = \frac{1}{4} \sum_{\mathbf{k}} \Omega(\mathbf{k}, \mathbf{k}') \begin{pmatrix} \Delta^{A,A}(\mathbf{k}) \\ \Delta^{A,B}(\mathbf{k}) \\ \Delta^{B,A}(\mathbf{k}) \\ \Delta^{B,B}(\mathbf{k}) \end{pmatrix}, \tag{3.32}$$

where the matrix $\Omega(\mathbf{k},\mathbf{k}')$ is a $4\times4$ matrix defined as

$$\Omega(\mathbf{k},\mathbf{k}') \equiv \begin{pmatrix} g_1\Gamma^{A,A}_{A,A}(\mathbf{k}) & g_1\Gamma^{A,B}_{A,A}(\mathbf{k}) & g_1\Gamma^{B,A}_{A,A}(\mathbf{k}) & g_1\Gamma^{B,B}_{A,A}(\mathbf{k}) \\ g_2 f(\mathbf{k}-\mathbf{k}')\Gamma^{A,A}_{A,B}(\mathbf{k}) & g_2 f(\mathbf{k}-\mathbf{k}')\Gamma^{A,B}_{A,B}(\mathbf{k}) & g_2 f(\mathbf{k}-\mathbf{k}')\chi^{+}(\mathbf{k})\Gamma^{B,A}_{A,B}(\mathbf{k}) & g_2 f(\mathbf{k}-\mathbf{k}')\Gamma^{B,B}_{A,B}(\mathbf{k}) \\ g_2 f^{*}(\mathbf{k}-\mathbf{k}')\Gamma^{A,A}_{B,A}(\mathbf{k}) & g_2 f^{*}(\mathbf{k}-\mathbf{k}')\Gamma^{A,B}_{B,A}(\mathbf{k}) & g_2 f^{*}(\mathbf{k}-\mathbf{k}')\Gamma^{B,A}_{B,A}(\mathbf{k}) & g_2 f^{*}(\mathbf{k}-\mathbf{k}')\Gamma^{B,B}_{B,A}(\mathbf{k}) \\ g_1\Gamma^{A,A}_{B,B}(\mathbf{k}) & g_1\Gamma^{A,B}_{B,B}(\mathbf{k}) & g_1\Gamma^{B,A}_{B,B}(\mathbf{k}) & g_1\Gamma^{B,B}_{B,B}(\mathbf{k}) \end{pmatrix}. \tag{3.33}$$

### 3.2.1 Numerical solution of the linear gap equation

Since $\Omega(\mathbf{k},\mathbf{k}')$ now depends on $\mathbf{k}'$, we can no longer assume that $\Delta^{i,j}$ is independent of momentum and factor it out of the linear gap equation, as we did in the single-band system. To numerically solve the eigenvalue problem (3.32), we will consider a sampling of $\mathbf{k}$-points in reciprocal space in order to diagonalize the matrix $\Omega = [\Omega(\mathbf{k},\mathbf{k}');\mathbf{k},\mathbf{k}' \in \mathcal{P}]$ in the basis $\{(i,j,\mathbf{k});i,j \in A,B;\mathbf{k}\in\mathcal{P}\}$, where $\mathcal{P}$ can be taken as a discrete uniform grid of the parallelogram generated by the reciprocal lattice vectors $\mathbf{b_1}$ and $\mathbf{b_2}$ (See Eq. (3.5)):

$$\mathcal{P} = \left\{\alpha_n\mathbf{b_1}+\beta_m\mathbf{b_2};(\alpha_n,\beta_m)=\left(\frac{n}{N},\frac{m}{N}\right);n,m=0,1,2,...N-1\right\}, \tag{3.34}$$

where $N$ is the number of $\mathbf{k}$-points along $\mathbf{b_1}$ or $\mathbf{b_2}$. To fix notation, let us define

$$\Delta(\mathbf{k}) \equiv \begin{pmatrix}\Delta^{A,A}(\mathbf{k}) & \Delta^{A,B}(\mathbf{k}) & \Delta^{B,A}(\mathbf{k}) & \Delta^{B,B}(\mathbf{k})\end{pmatrix}^{T} \tag{3.35}$$

such that

$$\vec{\Delta} = \begin{pmatrix}\Delta(\mathbf{k}_0) & \Delta(\mathbf{k}_1) & \cdots & \Delta(\mathbf{k}_{N^2})\end{pmatrix}^{T}, \tag{3.36}$$

with $\mathbf{k}_i \in \mathcal{P}$.

Having obtained equation (3.32), we now must solve it numerically. Therefore, the computational problem is finding $T_c$ such that the eigenvalue equation $\Omega\vec{\Delta} = \vec{\Delta}$ is satisfied. In particular, we will associate $T_c$ with the temperature at which the highest eigenvalue of $\Omega$ is equal to 1. This means that $T_c$ is the (greater) root of the function

$$F(T) = \max_{\lambda\in\sigma(\Omega(T))}\{\lambda\} - 1, \tag{3.37}$$

where $\sigma(\Omega(T))$ is the spectrum of $\Omega(T)$.

Given that the construction and diagonalization of $\Omega(T)$ is a costly computational problem (of time complexity $O(N^4)$ and $O(N^6)$, respectively), it is imperative that we implement an optimized root-finding method to solve $F(T)=0$. We have settled on the Brent-Dekker's method [45, 46], which is an hybrid algorithm that combines the bisection method, the secant method and inverse quadratic interpolation.

At this point, one may ask if there is, besides the $T_c$ obtained from the eigenvalues of $\Omega$, any interest in computing the eigenvectors $\vec{\Delta}$ given that the gap parameter vanishes at $T_c$. The answer is that $\vec{\Delta}$ gives the direction in the mean-field parameter space in which $\vec{\Delta}$ becomes nonzero for $T < T_c$. Therefore, apart from its magnitude $\left\|\vec{\Delta}\right\|(T)$ and its dependence on temperature, we get a linear approximation of the gap parameter vector $\vec{\Delta}$ for temperatures just below $T_c$ and can study the structure of these eigenvectors in real or momentum space and investigate how the first superconducting modes emerge.

#### 3.2.1.1 On-site interaction

First off, let us study the solutions of equation (3.32) when we change the chemical potential and the on-site coupling constant, without the nearest-neighbor term, i.e., we will look at the behaviour of $T_c$ and $\Delta(\mathbf{k})$ for the parameters $(\mu, g_1)$, with $g_2 = 0$.

As one might except, for a general doping that corresponds to a nonzero density of states at the chemical potential, the scaling of $T_c$ with the on-site coupling $g_1$ follows the BCS equation (2.36). However, in the limit $\mu \to 0$, this picture changes given that $\rho(\varepsilon = 0) = 0$, i.e., the density of states vanishes (linearly) at the Fermi level in graphene. It turns out, that because of this vanishing density of states, superconductivity requires a minimum coupling constant to develop, $g_1^c$, and becomes quantum critical. The convergence of the curves $T_c(g_1;\mu)$ into the critical curve $T_c^0 = lim_{\mu\to 0} T_c(g_1;\mu)$ can be seen in Fig. 3.2.

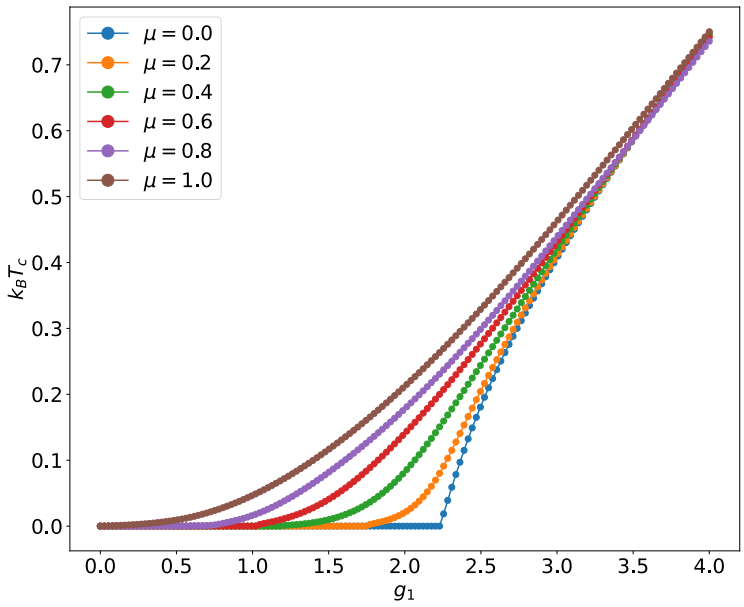


Figure 3.2: $k_B T_c$ as a function of $g_1$, for the values of the chemical potential $\mu \in \{0, 0.2, 0.4, 0.6, 0.8, 1\}$ measured from the Dirac point of graphene. We can see that the quantum critical curve emerges as we lower the chemical potential, $\mu \to 0$.

In Fig. 3.3, we can see the critical temperature diagram as function of the coupling parameter and the chemical potential. The critical point is found at $\left(\mu, g_1^c\right) = (0, 2.25)$. In the horizontal slices, $g_1 = const.$, we see that the critical temperature follows the behaviour of the density of states and has its maxima at $\mu = \pm 1$, i.e., at the Van Hove singularities of graphene. This is also an expected behaviour from the BCS equation (2.36), $T_c \sim \exp\left(-\left[g_1 \rho(0)\right]^{-1}\right)$, because changing $\mu$, while keeping the coupling constant, amounts to changing $\rho(0) = \rho(\xi = 0) = \rho(\varepsilon = \mu)$.

Regarding the reciprocal space structure of the superconducting gap in the sublattice basis, since we are only considering an on-site interaction, we have $\Delta^{A,B}(\mathbf{k}) = \Delta^{B,A}(\mathbf{k}) = 0$ and only $s$-wave superconductivity

emerges with an homogeneous gap parameter which is independent of momentum $\Delta^{A,A}(\mathbf{k}) = \Delta^{B,B}(\mathbf{k}) = \Delta_1$.

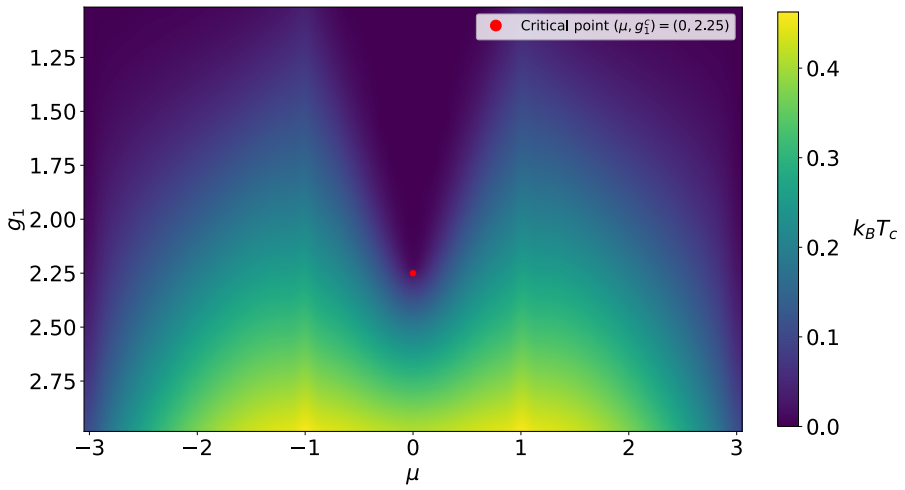


Figure 3.3: Heatmap of $k_B T_c$ as a function of $\mu$ and $g_1$. The critical temperature along the horizontal lines, $g = const.$, follows the behaviour of the DOS, and has its maxima at the Van Hove singularities.

#### 3.2.1.2 On-site and nearest-neighbor interaction

We can now turn on the nearest-neighbor interaction and investigate the critical temperature as a function of $g_1$ and $g_2$. The results are summarized in Fig. 3.4.

With the chemical potential at the Fermi level, we also find that, with $g_1 = 0$, that there is a minimum nearest-neighbor coupling, $g_2^c$, required for the critical temperature to be finite. For $\mu = 0$, we now have two critical lines $g_1 = g_1^c$ and $g_2 = g_2^c$ and the critical temperature is only finite if $g_1 > g_1^c$ or $g_2 > g_2^c$. If $g_1 < g_1^c$ and $g_2 < g_2^c$, the critical temperature in null and superconductivity cannot occur. This can be seen on the 3D plot of Fig. 3.4a in the form of a flat surface, corresponding to $T_c = 0$ in the $(g_1, g_2)$ plane.

For $\mu \neq 0$, we have $\left(g_1^c, g_2^c\right) = (0,0)$ and a superconducting phase always develops unless both the on-site and the nearest-neighbor interaction are repulsive, as seen in Fig. 3.4b.

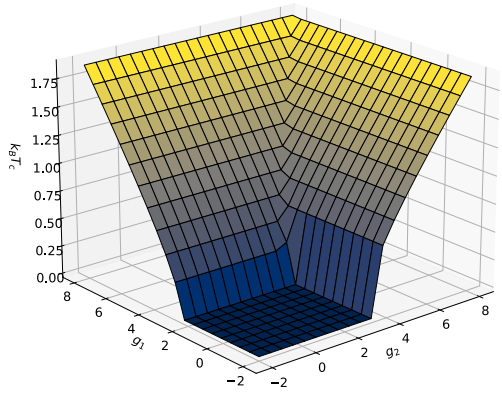


(a)

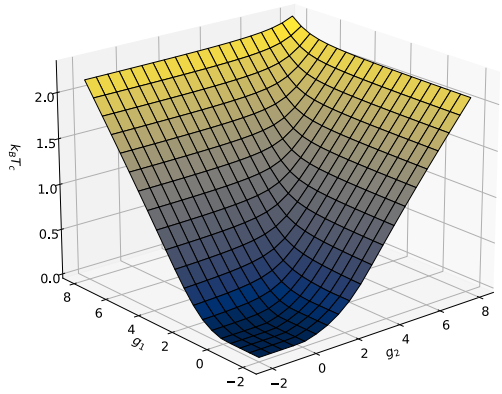


(b)

Figure 3.4: $k_BT_c$ as a function of $g_1$ and $g_2$. $(a)$ With the chemical potential at $\mu = 0$, it is evident that there is a forbidden region for superconductivity when $g_1 < g_1^c$ and $g_2 < g_2^c$. $(b)$ With the chemical potential at $\mu = 1$, superconductivity always develops for positive values of $g_1$ or $g_2$.

Having looked at $T_c$, we now study the eigenvectors $\Delta^{A,B}(\mathbf{k})$ when the nearest-neighbor interaction is dominant, $g_2 > g_1$. Recalling that the nearest-neighbor interaction term has a momentum dependent

coefficient $f_{i,j}(\mathbf{q})$, given in Eq. (3.20), we expect the superconductor gap parameter to also be momentum dependent, contrasting with the on-site only case. As we can see in Fig. 3.5, $\left|\Delta^{A,B}(\mathbf{k})\right|$ has a minimum at the $\Gamma$-point and a maximum at the $\boldsymbol{M}$-point, which lies between the Dirac points $\boldsymbol{K}$ and $\boldsymbol{K'}$ where the chemical potential $\mu = 0$ was placed, where the density of states has a van Hove singularity.

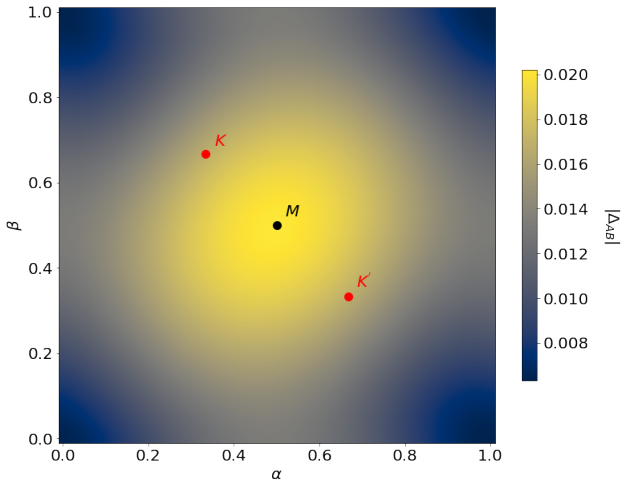


Figure 3.5: $\left|\Delta^{A,B}\right|$ as a function of $\mathbf{k} = \alpha\mathbf{b_1} + \beta\mathbf{b_2}$, with $(\mu, g_1, g_2) = (0, 5, 10)$. The Dirac points are marked in red, while the $\boldsymbol{M}$-point is marked in black.

What phases exist for general couplings $g_1$ and $g_2$, and how do they change with doping? An easy way to probe these phases is to look at the momentum space order parameter defined as

$$\eta = \left\langle\left|\Delta^{A,A}(\mathbf{k})\right|\right\rangle_{\mathbf{k}} - \left\langle\left|\Delta^{A,B}(\mathbf{k})\right|\right\rangle_{\mathbf{k}}, \tag{3.38}$$

where $\langle\cdots\rangle_{\mathbf{k}}$ is the average over the momentum space unit cell. The phase diagram for the $\eta$ order parameter as a function of $g_1$ and $g_2$ can be seen in Fig. 3.6. We found three types of phases: for $g_1$ dominant, only the on-site superconductor gaps $\Delta^{A,A}$ and $\Delta^{B,B}$ develop; for $g_2$ dominant, only the nearest-neighbor gaps $\Delta^{A,B}$ and $\Delta^{B,A}$ develop; and finally if $g_1 \sim g_2$ and $\mu \neq 0$, we get a mixed phase where the two types of superconductor gaps coexist. For $\mu = 0$, this mixed phase doesn't exist and the transition between the on-site and the nearest-neighbor phases is abrupt.

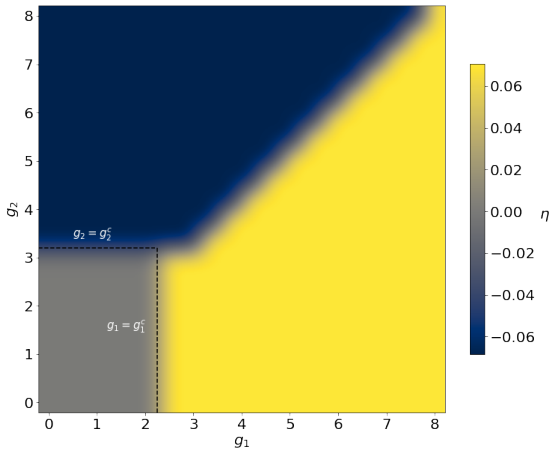


(a) $\mu = 0$

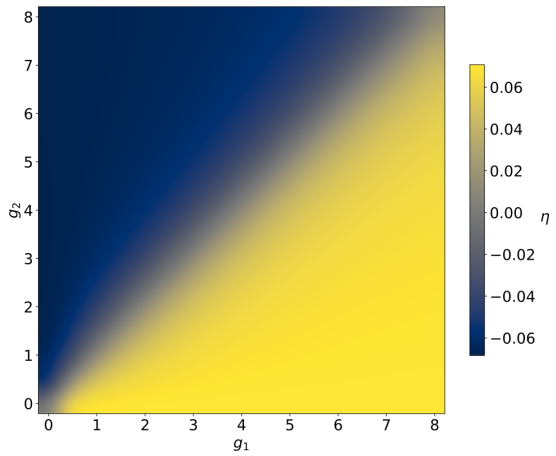


(b) $\mu = 1$

Figure 3.6: $\eta$ as a function of $g_1$ and $g_2$. The critical lines $g_1 = g_1^c = 2.25$ and $g_2 = g_2^c = 3.2$ are marked in black.

## 3.3 Real space linear gap equation

Since we are going to work in real space when we study quasiperiodic systems, it will be useful to do a real space analysis for the graphene monolayer as a crosscheck. The aim will then be to show that the two approaches are compatible alternatives, with similar results for the critical temperature, at least for the case of commensurable systems such as the graphene monolayer.

Recalling Eq. (2.39) for the general form of the linear gap equation in the real-space lattice basis and considering only on-site and nearest-neighbor interactions, with an Hamiltonian given by (3.17), the linear

gap equation reduces to

$$\Delta^{i,j} = V_{j,i} \sum_{i_3,i_4} \sum_{\lambda,\lambda'} \chi\left(E_\lambda, E_{\lambda'}\right) \phi_i^\lambda \phi_{i_3}^{\lambda,*} \phi_j^{\lambda'} \phi_{i_4}^{\lambda',*} \Delta^{i_3,i_4}, \tag{3.39}$$

where the interaction coefficients are simply

$$V_{i,j} = \begin{cases} -g_1 & i = j \\ -g_2 & i,j \quad \text{are NN.} \end{cases} \tag{3.40}$$

### 3.3.1 Numerical solution of the linear gap equation

Now that we are equipped with the real space linear gap equation (3.39), we can compute $T_c$ for different parameters $(g_1, g_2, \mu)$ and compare them with the results obtained from the momentum space linear gap equation.

For example, with $\mu = 0$, we see in Fig. 3.7 that the curves $T_c\left(g_1; g_2 = 0\right)$ and $T_c\left(g_1 = 0; g_2\right)$ for the real space and the momentum space gap equation agree quite well with one another.

For $g_2 = 0$, we only have $s$-wave superconductivity and the real space eigenvector $\Delta^{i,j}$ corresponds to an homogeneous solution $\Delta^{i,j} = 0$ if $j \neq i$ and $\Delta^{i,i} = \Delta_1 \neq 0, \forall i$, similar to the momentum space case. This homogeneous solution implies that the $g_1^c$ computed with the real space equation is the same as in the momentum space equation solution and this is exactly what we found.

However, this perfect agreement does not occur for the $g_1 = 0$ case. The real space curve converges to the momentum space one for high values of the nearest-neighbor interaction coefficient $g_2$. But for lower values of $g_2$, the curves do not completely match and the computed values of $g_2^c$ have a relative error of 20%, with the $g_2^c$ for the real space linear gap equation smaller than that for the momentum space equation. This is a due to a finite size effect, which is expected to vanish as we increase the number of unit cells used in the real space computation, i.e., as we increase the system size $L = 2N^2$ where $N$ is the number of unit cells along the $\mathbf{a}_1$ or the $\mathbf{a}_2$ direction.

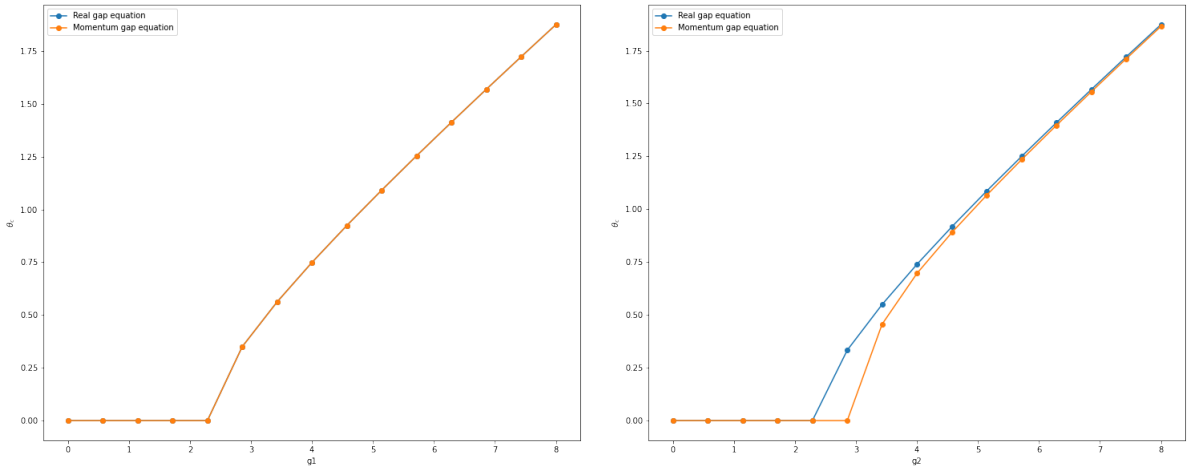


(a) $T_c\,(g_1; g_2 = 0)$ (b) $T_c\,(g_1 = 0; g_2)$

Figure 3.7: $T_c\,(g_1; g_2 = 0)$ and $T_c\,(g_1 = 0; g_2)$ computed from linear gap equation formulated in real (blue curve) and momentum space (orange curve). We used $N^2 = 10^2$ unit cells in the real space computation and $N^2 = 10^2$ **k**-points in the momentum space computation.

# Chapter 4

# 1D quasiperiodic models

After studying superconductivity in commensurate systems, such as the single-band homogeneous system (in Section 2.4) and the single layer graphene (in Chapter 3), we are now in a position to investigate how the quasiperiodic nature of some systems can affect superconductivity. How does the incommensurability of a system affect the superconductor critical temperature and the superconductor local parameters close to this temperature? This is the question we are going to try to answer in this chapter for some one-dimensional quasiperiodic models which will include the Aubry-André-Harper model [24, 25], a standard system to study quasiperiodicity, and an extended version of it with off-diagonal quasiperiodic modulation.

## 4.1 Aubry-André-Harper model

The tight-binding Hamiltonian for the 1D AAH model is

$$\hat{H}_{AAH} = -t \sum_{\sigma,m} \left( c^{\dagger}_{m,\sigma} c_{m+1,\sigma} + c^{\dagger}_{m+1,\sigma} c_{i,\sigma} \right) - J \sum_{\sigma,m} \cos\left(2\pi Q m\right) c^{\dagger}_{m,\sigma} c_{m,\sigma}, \tag{4.1}$$

where $t$ is the nearest-neighbor hopping integral, $J$ is the strength of the quasiperiodic potential and $Q$ is the inverse of the wavelength of the quasiperiodic potential.

This model has some interesting properties that we will briefly mention. First, there is a duality between the space and momentum representations of its Hamiltonian. If we do a transformation at the $c$-operator level between the Wannier basis and the momentum basis as

$$c^{\dagger}_{m} = \frac{1}{\sqrt{N}} \sum_{k} e^{-2\pi i Q k R_m} c^{\dagger}_{k}, \tag{4.2}$$

where $2\pi Qk$ is Bloch momentum, $k \in \{0, 1, \ldots, N-1\}$, we find that the transformed Hamiltonian has the dual form

$$\hat{H}'_{AAH} = -\frac{J}{2} \sum_{\sigma,k} \left( c^{\dagger}_{k,\sigma} c_{k+1,\sigma} + c^{\dagger}_{k+1,\sigma} c_{k,\sigma} \right) - 2t \sum_{\sigma,k} \cos\left(2\pi Q k\right) c^{\dagger}_{k,\sigma} c_{k,\sigma}. \tag{4.3}$$

The Hamiltonian in (4.3) has the same structure as the original Hamiltonian in (4.1), with nearest-neighbor tunneling change from $t \to \frac{J}{2}$ and the on-site quasiperiodic strength from $J \to 2t$. The form of the Hamiltonian is actually left invariant when $J = 2t$. An heuristic argument can be made that, for the Hamiltonian in (4.1), the eigenstates should be extended in real space for small values of $J$, while for the Hamiltonian in (4.3), they should be extended in momentum space for small values of $t$, suggesting that $J = J_c \equiv 2t$ corresponds to a localization-delocalization transition. This study can be made rigorous and this duality along with the nature of the transition has been extensively analysed in the literature [25, 27–29].

From now on, for simplicity purposes, we will take $t = 1$, i.e., all energy values will be in units of $t$.

It turns out that all eletronic states of the 1D AAH model are extended for $J < J_c$, localized for $J > J_c$, and critical for $J = J_c$, due to the previously mentioned duality. We then have a transition that is independent of energy and the line $J = J_c$ in the $(E, J)$ diagram separates localized and extended eigenstates.

The localization transition depends on the value of the parameter $Q$. In order to observe the transition, $Q$ must have some degree of incommensurability. Choosing $Q$ to be irrational does correspond to the quasiperiodic case. However, if we wish to use periodic boundary conditions (PBC) in our real space numerical simulations, $Q$ must be rational. A common approach is to consider a sequence of rational approximants $Q_n$ of the irrational number $Q$ such that $\lim_{n\to\infty} Q_n = Q$. For each $n$, the system is chosen to be of the size of the unit cell defined by $Q_n$, that should increase with $n$ for the quasiperiodic limit to be accurately taken.

The energy spectrum of (4.1) as a function of $Q$ yields quite a beautiful picture (See Fig. 4.1) called the Hofstadter butterfly [26]. The structure of the spectrum for $J \neq J_c$ is quite different from that associated with $J = J_c$, since for $J = J_c$ it shows a complex self-similar geometric shape called a fractal. The model with $J = 2$ has been greatly studied in literature, given that it is the reduction to 1D of the problem of an eletron moving in a 2D square lattice in the presence of a perpendicular magnetic field [24, 26].

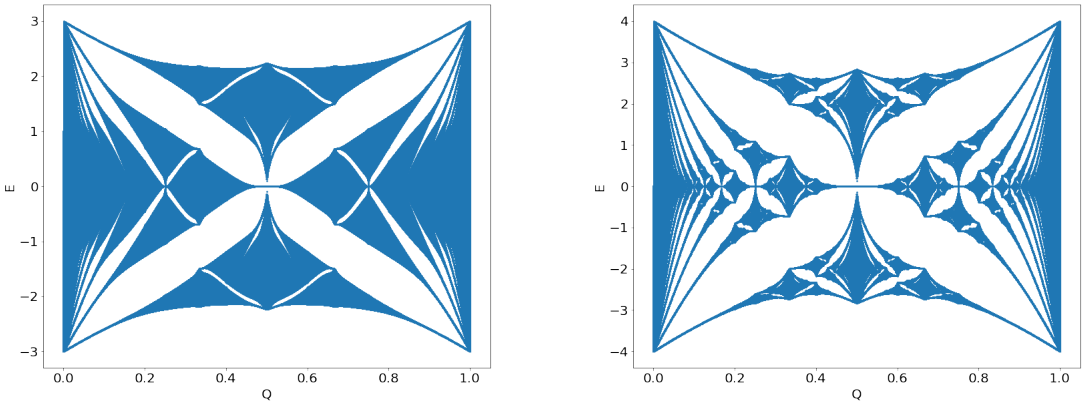


(a) $J = 1$ (b) $J = 2$

Figure 4.1: Energy spectrum of the 1D AAH model as a function of $Q$, with $Q = \frac{i}{N}$ such that $i \in \{0, 1, 2, \ldots, N\}$ where $N = 2584$ is the system size. At $J = 2$, we can see the Hofstadter butterfly.

A common choice in the study of the AAH model is to take $Q$ as the golden ratio conjugate

$$\varphi = \frac{\sqrt{5}-1}{2} \approx 0.618, \tag{4.4}$$

which can be obtained from the Fibonacci sequence. The Fibonacci sequence is defined by the recurrence relation

$$\begin{aligned} &F_0 = 0, \qquad F_1 = 1, \\ &F_n = F_{n-1} + F_{n-2},\ n > 1, \end{aligned} \tag{4.5}$$

and the ratio of consecutive Fibonacci numbers converges to the golden ratio conjugate

$$\lim_{n\to\infty} \frac{F_{n-1}}{F_n} = \varphi. \tag{4.6}$$

We can then choose $Q = \varphi$ and the rational approximants as $Q_n = \frac{F_{n-1}}{F_n}$. For the $n$-th approximant, the size of our system is determined by $F_n$ in order to have matching PBC. Some of our rational approximants will be

$$\frac{2}{3}, \frac{3}{5}, \frac{5}{8}, \frac{8}{13}, \frac{13}{21}, \frac{21}{34}, \cdots$$

The Fibonacci sequence is particularly good because it allows us to access many system sizes, defined by the denominator of the irreducible fractions above. This is advantageous for a more detailed finite-size analysis.

There are several methods to study localization in this type of systems such as the transfer matrix method or the analysis of level statistics. However, in describing the localization transition and the nature of the eigenstates of our systems, we will use the inverse participation ratio (IPR) which is a quantity widely used in the literature. The utility of the IPR is that it can encode in a single number the extended or localized nature of a wave function, saving us from having to look at the distribution of the eigenstates in each realization to ascertain its nature. It is also easy to generalize to other types of distributions besides wave functions, such as our superconductor order parameters (See Eq. (4.9)).

For the real space eigenstate $\phi^\lambda$, with energy $E_\lambda$, the IPR is defined as

$$IPR(E_\lambda) \equiv \frac{\sum_i \left|\phi_i^\lambda\right|^4}{\left[\sum_i \left|\phi_i^\lambda\right|^2\right]^2}, \tag{4.7}$$

where the sum $\sum_i$ is over all lattice sites. We can then study the two extreme limits of the IPR. On the one hand, if a normalized wave function is extended over the entire lattice, its components will be $\phi_i \sim \frac{1}{\sqrt{N}}$, where $N$ is the number of lattice sites, hence the IPR goes to zero as $\sim \frac{1}{N}$. On the other hand, if the wave function is localized on a few lattice sites, then $IPR \sim const$, being equal to 1 in the extreme case when the wave function is localized at a single site.

In our numerical results, we will often present the quantity $-\frac{\log(IPR)}{\log(N)}$, that for extended states converges to 1 as we increase the system size and that for localized states converges to 0. We can see clearly in Fig. 4.2 that the localization transition for the 1D AAH is at $J_c = 2$ and all states undergo a transition from extended

to localized. At $J = J_c$, the states are neither localized or extended but are instead critical, and in this case the $IPR$ does not converge to zero as $\sim \frac{1}{N}$ or to a non-zero constant, hence $0 < -\frac{\log(IPR)}{\log(N)} < 1$.

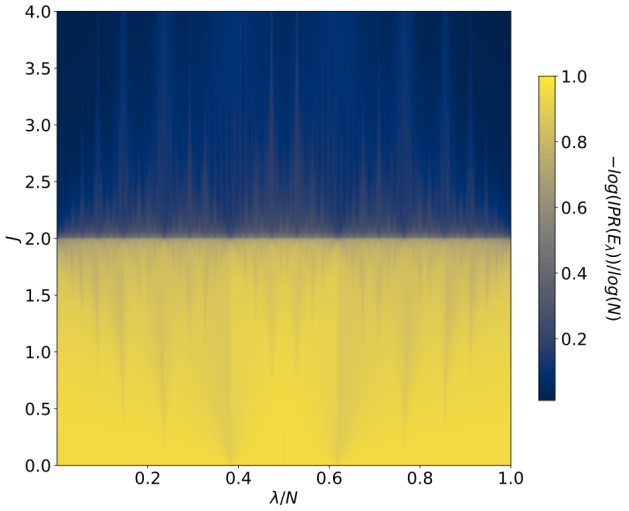


Figure 4.2: $-\log(IPR(E_\lambda))/\log(N)$ as a function of $J$ and the normalized eigenstate index $\frac{\lambda}{N}$, for $N = 2584$. All eigenstates transition from extended to localized at $J_c = 2$ and the mobility edge is just the line $J = J_c$.

A good order parameter for the extended-localized transition in the AAH model is the average of the IPR over the whole spectrum $\langle IPR(E_\lambda)\rangle_{E_\lambda}$. And, as shown in Fig. 4.3, it is practically zero for $J < J_c$, starts to become finite at $J_c$ and progressively increases towards unity as our quasi-disorder gets stronger.

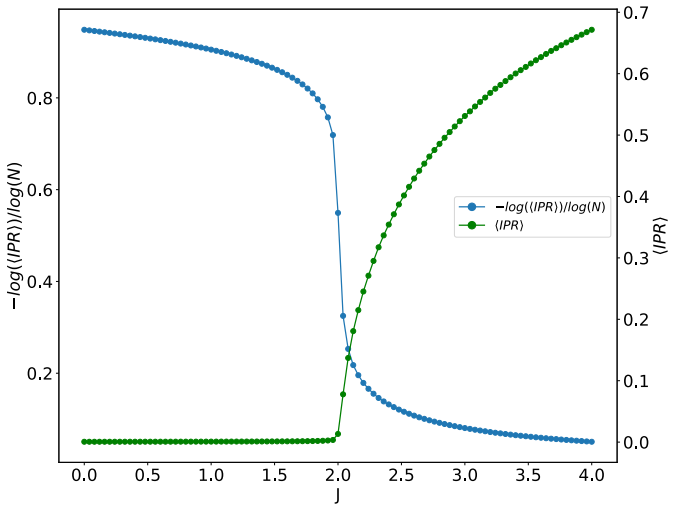


Figure 4.3: $\langle IPR\rangle_{E_\lambda}$ and $-\log\left(\langle IPR\rangle_{E_\lambda}\right)/\log(N)$ as a function of $J$, for $N = 2584$. It is clear in both curves that the localization transition happens at $J = 2$.

### 4.1.1 Critical temperature

Now that we discussed the general properties of the single-particle part of our Hamiltonian, we are ready to move on to study the effect of incommensurability on superconductivity. To this effect, our interaction Hamiltonian will be an on-site Hubbard term (2.40) to allow for $s$-wave singlet superconductivity. To fix nomenclature, we will call the original form of the linear gap equation (2.41) the Hubbard linear gap equation (HLGE), while the linear gap equation in the time-reversal pairing approximation (2.50) will be called the Anderson linear gap equation (ALGE).

The first quantity of interest associated with the superconductivity that we intend to study is, of course, the transition temperature from the phase our single-particle system is in, metal or insulator, to the superconductor phase. Unless stated otherwise, our noninteracting system is always at half-filling.

In general, we find that the critical temperature is enhanced by the quasiperiodic potential and this increase of $T_c$ with $J$ is particularly evident for small values of the coupling $g_1$ when we cross the localization transition at $J_c = 2$, as can be seen in Fig. 4.4. At this point, it is useful to compare the critical temperature curves computed with HLGE and ALGE. The curves in Fig. 4.4 show us that the HLGE and the ALGE produce similar results in the extended regime, $J < J_c$, indicating that the diagonal pairing we do for the ALGE captures all the relevant superconductor properties for extended states. However, as we approach $J_c$ and the transition to the localized regime, $J > J_c$, there is a small discrepancy between the two curves, which is noticeable for higher values of the interaction coupling $g_1$, but vanishes for small couplings. These results assure us that the ALGE is quite apt at capturing the behaviour of the critical temperature as a function of the single-particle parameters for weak coupling (small $g_1$).

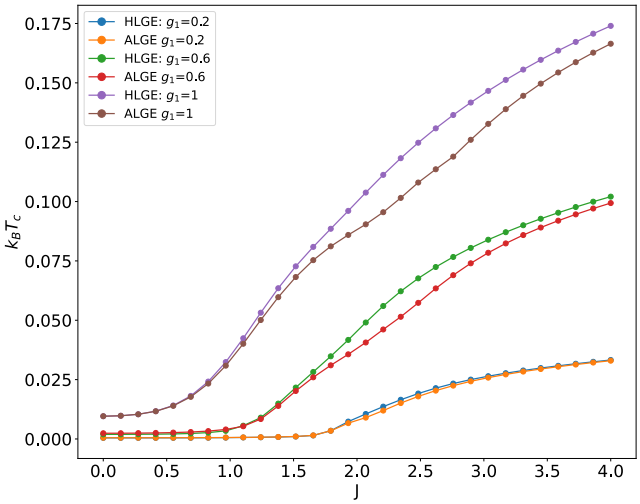


Figure 4.4: $k_BT_c$ as a function of $J$, computed with the HLGE and the ALGE, for $g_1 \in \{0.2, 0.6, 1\}$. The size of the 1D chain is $N = 233$, corresponding to $Q = \frac{144}{233}$.

This enhancement of the critical temperature with the quasiperiodic potential strength could just be a consequence of the increase of the density of states at the Fermi level with our correlated disorder and not

a result of the incommensurability of the system. A suitable test to discern between these two effects is to study how the critical temperature scales with the interaction coupling $g_1$ and compare the commensurate limit with the incommensurate one. In the extended regime, one might expect a scaling similar to that of the BCS equation (2.36), but this will not be the case in the critical or localized regime, as we show in Fig. 4.5.

In order to compare the commensurate case with the incommensurate case, we must be able to construct a periodic potential such that our system contains many periods, i.e., unit cells. This can be done by constructing sytems with roughly the same size but with $Q$ chosen from different rational approximants. For example, in the analysis we do in Fig. 4.5, we consider the sequence of rational approximants $Q_n \in \left\{\frac{3}{5}, \frac{8}{13}, \frac{1597}{2584}\right\}$, extracted from the Fibonacci sequence. If we take the system with $Q_3 = \frac{1597}{2584}$, then its size has to be $N_3 = 2584$ in order to obey PBC. In this case, the system has one unit cell, $\#u.c. = 1$, and we will take this choice of rational approximant as our incommensurate limit. For our commensurate limit, we can choose $Q_1 = \frac{3}{5}$, which corresponds to a potential that is repeated every 5 lattice sites. If we fix the system size at $N_1 = 2585 \approx N_3$, we have a system comprising 517 periods, i.e., a system with 517 unit cells, $\#u.c. = 517$. This procedure can be repeated with other rational approximants and we can go back and forth between the incommensurate and the commensurate limit with as many unit cells as our sequence of rational approximants allows. In our example, the sequence of rational approximants we have chosen, $Q_n \in \left\{\frac{3}{5}, \frac{8}{13}, \frac{1597}{2584}\right\}$, will correspond to systems of roughly the same size $N_n \in \{2585, 2587, 2584\}$, but spanning different numbers of unit cells, $\#u.c. \in \{517, 199, 1\}$.

Using the ALGE, we found that in the extended regime, $J < J_c$, the scaling of the critical temperature with the interaction coupling follows that of the BCS equation in both the commensurate and the incommensurate limit, i.e., $T_c \sim \exp\left(-[g_1 \rho(0)]^{-1}\right)$. In the localized regime, $J > J_c$, and in the incommensurate case, the critical temperature scales almost linearly, $T_c \sim g_1^{1.004 \pm 0.001}$ (See Fig. 4.5b). However, in the critical regime $J = J_c$ and in the incommensurate limit, its scaling is significantly enhanced, following a power-law with a greater exponent $T_c \sim g_1^{1.50 \pm 0.02}$ (See Fig. 4.5a). This is in line with recent literature [22]. As we can see in Fig. 4.5, in the commensurate case with $\#u.c. = 517$, the power-law behaviour vanishes and we get back our BCS scaling, both for $J = J_c$ and $J > J_c$. However, even with $\#u.c. = 199$, $T_c$ still has an almost power-law scaling, indicating that at the level of superconductivity we do not need to get too close to the incommensurate limit, i.e., the irrational limit in $Q$ (corresponding to extremely large systems), to see the effects of incommensurability on the superconductor critical temperature. Low order rational approximants can already capture this behaviour, both in the critical regime and the localized regime of the 1D AAH model.

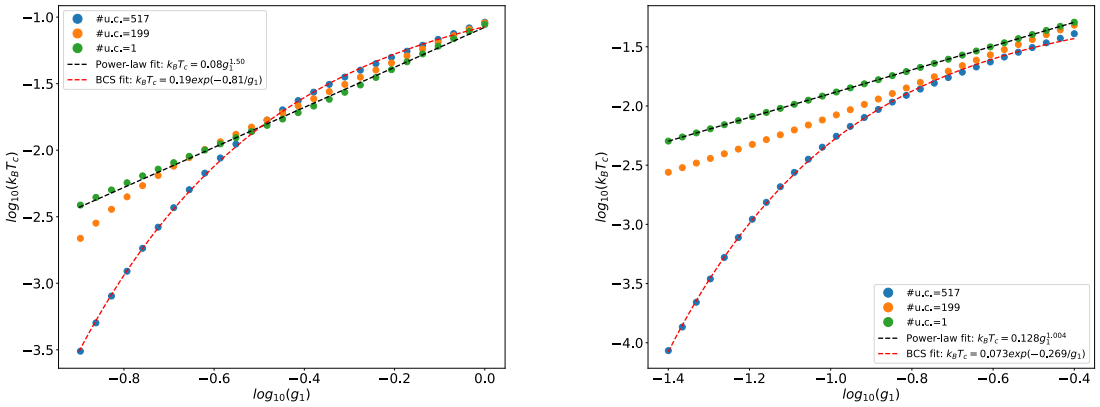


(a) (b)

Figure 4.5: log-log plot of the scaling of $k_BT_c$ with $g_1$ for different numbers of unit cells, $\#u.c. \in \{517, 199, 1\}$, corresponding to the rational approximants $Q_n \in \left\{\frac{3}{5}, \frac{8}{13}, \frac{1597}{2584}\right\}$. The system size is fixed at $N = 2584$ for the case with one unit cell $Q_n = \frac{1597}{2584}$ and similar sizes for the other choices of rational approximants. These results were computed with ALGE. $(a)$ $J = 2$. The power-law fit to the $\#u.c. = 1$ curve gives us $k_BT_c = 0.08g_1^{1.50}$, while a BCS fit to the $\#u.c. = 517$ curve gives $k_BT_c = 0.19e^{-0.81/g_1}$. $(b)$ $J = 3$. The power-law fit to the $\#u.c. = 1$ curve gives us $k_BT_c = 0.128g_1^{1.004}$, while a BCS fit to the $\#u.c. = 517$ curve gives $k_BT_c = 0.073e^{-0.269/g_1}$.

To explain why the critical temperature scales with the interaction coupling parameter as it does at the level of the ALGE, we can present an argument similar to that of Ref. [47] in the context of Anderson disorder. This argument relies on the structure of the $M$-matrix (2.46), which is represented in Fig. 4.6.

In the extended regime, for $J < J_c$, all the eigenstates are extended across the entire system, $\phi_i^\lambda \sim \frac{1}{\sqrt{N}}$, so that the elements of $M$ are actually independent of energy. Because of this uniformity, its elements scale simply as $M_{\lambda,\lambda'} \sim \frac{1}{N}$, so that the ALGE reduces to the standard BCS equation (2.32) which admits an homogeneous gap parameter and a critical temperature that has a BCS scaling with $g_1$.

In the localized regime, for $J > J_c$, the eigenstates are all strongly localized, have negligible overlap with each other and are characterized by their localization length $\xi_\lambda$, such that the wave functions scale as $\phi_i^\lambda \sim \frac{1}{\sqrt{\xi_\lambda}}$, and the $M$-matrix is approximately given by $M_{\lambda,\lambda'} = \delta_{\lambda,\lambda'} \sum_i \left|\phi_i^\lambda\right|^4 = \frac{\delta_{\lambda,\lambda'}}{\xi_\lambda^2}$ (there are small overlaps due to the finite localization length, as seen in Fig. 4.6b). This means that the ALGE just gives us the simple linear scaling $T_c = \frac{g_1}{4\xi_\lambda}$. This also explains why $T_c$ increases with the quasiperiodic potential strength, since $\xi_\lambda$ actually decreases with $J$, for $J > J_c$.

The interesting part happens for $J = J_c$. In this case, the $M$-matrix has its richest structure. It is evident in Fig. 4.6c that the $M$-matrix is self-similar and exhibits a fractal geometry akin to that of the previously discussed Hofstadter butterfly, which is not surprising since we know that the AAH spectrum is also self-similar [48]. Due to its self-similarity, we could assume that $M$ is an homogenous function in its two energy variables $M(zE_\lambda, zE_{\lambda'}) = z^\alpha M(E_\lambda, E_{\lambda'})$. This scaling argument when applied to the ALGE, would imply a power-law scaling of $T_c$ with $g_1$ dependent on the $\alpha$ exponent.

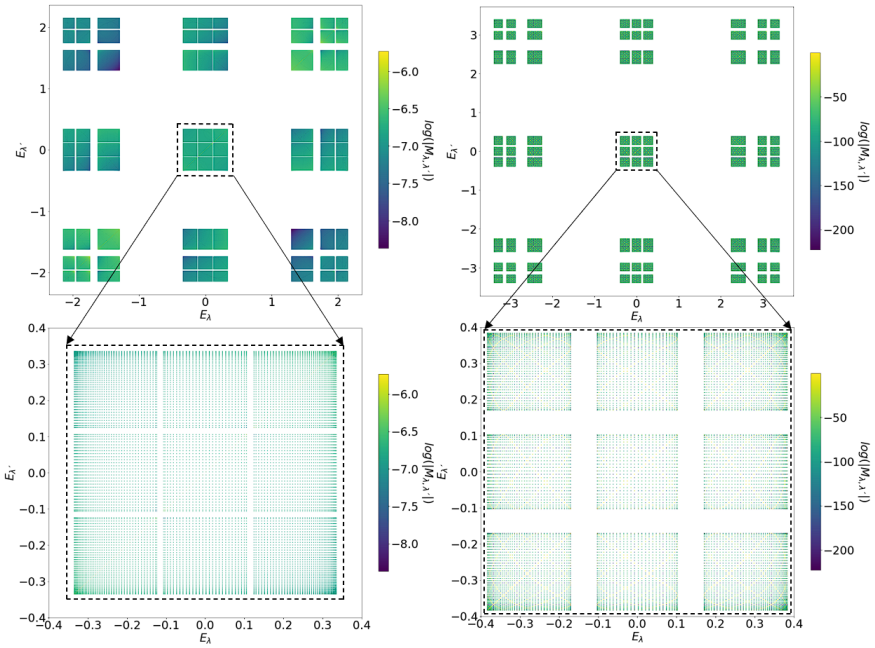

(a) $J = 1$ (b) $J = 3$

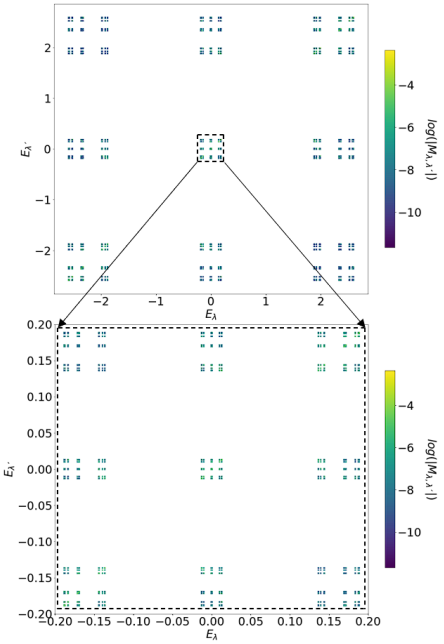

(c) $J = 2$

Figure 4.6: Structure of $M_{\lambda,\lambda'}$, for $N = 987$. Each dot represents an element of $M_{\lambda,\lambda'}$ with its color given by $\log_{10}\left(\left|M_{\lambda,\lambda'}\right|\right)$, with the axes representing the spectrum of the AAH model for a given value of $J$. Under each image is a zoom for energies close to the chemical potential. In the case $J = J_c = 2$, the self-similarity of the $M$-matrix is quite evident.

With the results of chapter 5 in mind, let us take a small detour to investigate what happens when we

impose an energy cutoff on the ALGE. A cutoff in energy can be easily introduced by truncating (2.50) to a subspace of our eigenspace for which $|\xi_\lambda| \leq \xi_{\max}$, such the truncated version is given by

$$\Delta^\lambda = g \sum_{\{\lambda' : |\xi_{\lambda'}| \leq \xi_{\max}\}} M_{\lambda,\lambda'} \frac{\tanh\left(\frac{\xi_{\lambda'}\beta}{2}\right)}{2\xi_{\lambda'}} \Delta^{\lambda'}. \tag{4.8}$$

In the general, we found its effect negligible on the critical temperature unless we were studying it as a function of doping or imposing a very restrictive cutoff. This happens because the factor $\frac{\tanh\left(\frac{E_\lambda \beta_c}{2}\right)}{2E_\lambda}$ in the ALGE already assures that states relatively close to the Fermi level are more relevant to the structure of the gap equation than those that are far away. If we study $T_c$ as a function of $\mu$ with all other relevant parameters fixed, we find that $T_c$ follows the density of states at the Fermi level more closely, i.e., it has a maximum/minimum when $\rho(\xi = 0)$ has a maximum/minimum, when we impose a more restrictive cutoff in energy.

However, a very restrictive energy cutoff can have a big impact when we study the scaling of the critical temperature with the interaction coupling $g_1$. As we can see in Fig. 4.7, at the critical point $J = 2$, imposing a smaller energy cutoff implies a power-law scaling with a smaller exponent $\eta$. A very small energy cutoff can reduce the power-law in the critical regime into a simple linear scaling, such as the one found for the localized regime with $J > 2$.

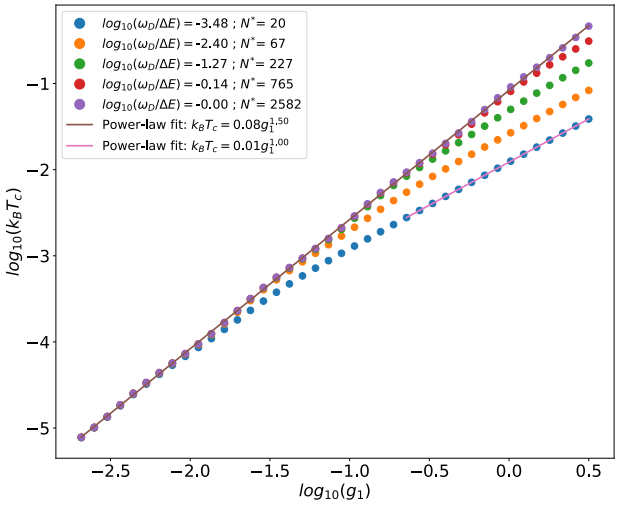


Figure 4.7: Critical temperature scaling with $g_1$ for $J = 2$ of the AAH model. The different curves correspond to different energy cutoffs $\log_{10}\left(\frac{\omega_D}{\Delta E}\right)$, where $\Delta E$ is the bandwith of the AAH model, associated with the dimensionality $N^*$of the truncated eigenspace used in the ALGE. The curve with $\log_{10}\left(\frac{\omega_D}{\Delta E}\right) = 0$ fits with the power-law $k_BT_c = 0.08g_1^{1.50\pm0.02}$, while the curve with the more restrictive cutoff $\log_{10}\left(\frac{\omega_D}{\Delta E}\right) = -3.48$ fits with power-law $k_BT_c = 0.01g_1^{1.00\pm0.02}$, i.e., we go from a power-law with exponent $\eta = 1.50$ to a linear scaling as we lower the values of the energy cutoff.

### 4.1.2 Localization of the superconductor local parameters

The next step in our study of superconductivity in the 1D AAH model is to look at the structure of eigenvectors of both the HLGE and the ALGE, i.e., at the lattice distribution of the superconductor local parameters.

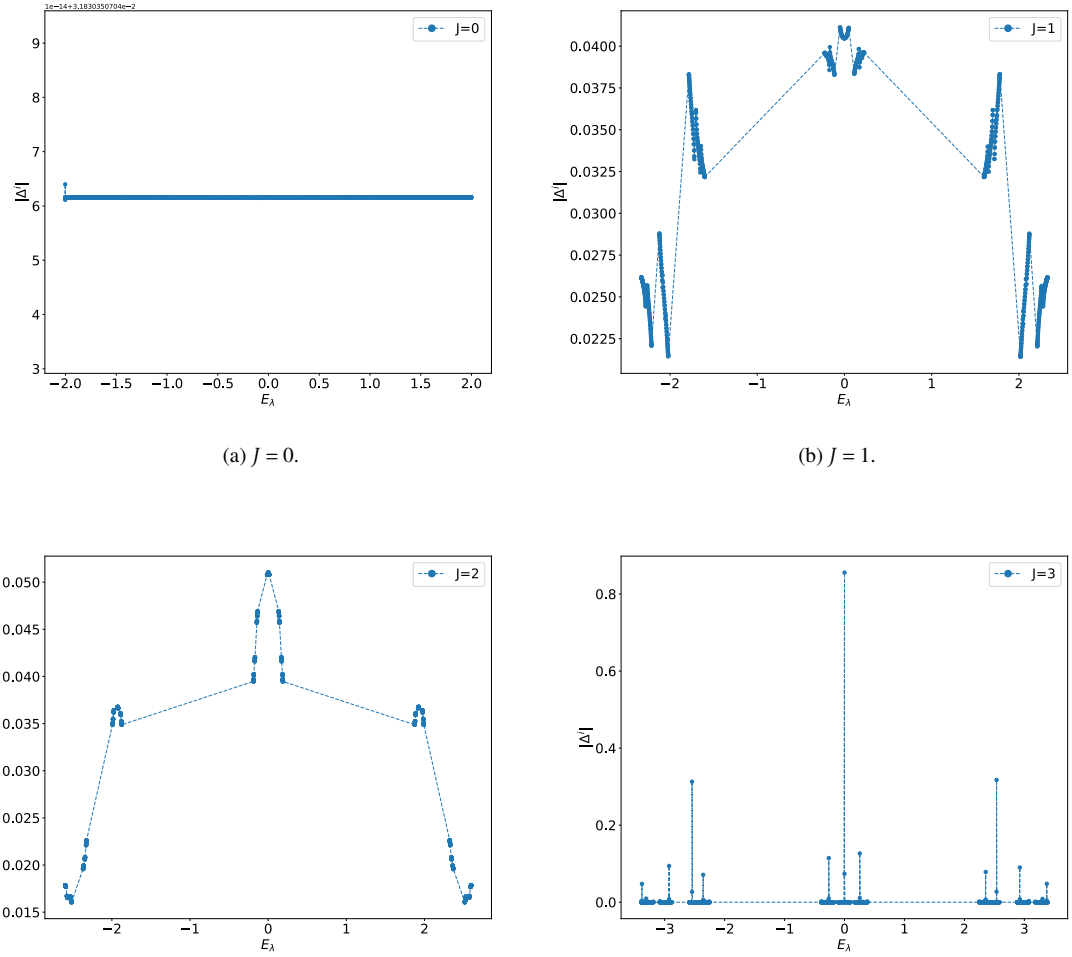


(a) $J = 0$.

(b) $J = 1$.

(c) $J = 2$.

(d) $J = 3$.

Figure 4.8: $\left|\Delta^\lambda\right|$ distribution for the spectrum of $\hat{H}_{AAH}$, with $N = 987$ and $g_1 = 0.5$. The gaps we see in the horizontal axis have a one-to-one correspondence with the gaps in the energy spectrum of the single-particle Hamiltonian, which is built into the construction of the ALGE.

First, we can take a look at the spectral distribution of the superconductor gap parameter in the eigenbasis of $\hat{H}_0 = \hat{H}_{AAH}$, i.e., at $\Delta^\lambda$ for each energy level $E_\lambda$, as shown in Fig.4.8, computed from the ALGE. When $J = 0$, we are in the clean limit of our system, and found that $\Delta^\lambda$ is the same for every energy level (Fig. 4.8a). This suggests that for commensurate systems with one orbital and on-site Hubbard interaction the gap parameter is the same for all eigenstates. This is similar to the results of section 3.2.1.1, where we

found a superconductor gap parameter independent of momentum for graphene. But as we increase $J$ we can see an asymmetry start to develop, with the maximum of $\left|\Delta^{\lambda}\right|$ always at the Fermi level. In the localized regime, the superconductor gap parameter at the Fermi energy is clearly dominant (Fig. 4.8d).

Regarding the real space localization of superconductor local parameters, we found out that there is also a transition from extended to localized phases in the $\Delta^{i}$'s, computed from Eq. (2.57). In analogy with the inverse participation ratio that we constructed for the noninteracting wave functions (4.7), we can also define an inverse participation ratio for the superconductor local parameters, associated with the highest eigenvalue of the linear gap equation, as

$$IPR_{\Delta} \equiv \frac{\sum_i \left|\Delta^i\right|^4}{\left[\sum_i \left|\Delta^i\right|^2\right]^2}, \tag{4.9}$$

given that the $\Delta^{i}$'s also form a distribution on the lattice.

For the HLGE, we found an extended regime for $J < J_c^{HLGE}$, with $J_c^{HLGE} \approx J_c$, that in the limit of $J \to 0$ tends to the typical homogeneous BCS solution, but as we increase the quasi-disorder it adquires a fluctuating real part, that never changes sign and still extends over the entire lattice, with no imaginary component. There is a localized regime for $J > J_c^{HLGE}$ with a exponential localization of the superconductor local parameters (See Figs. 4.11c and 4.11d), which turn out to always be real-valued and centered at the lattice sites for which the low energy wave functions, i.e., the eigenstates near the Fermi level of the noninteracting system locate (Fig. 4.10b). For $J = J_c^{HLGE}$, we also found a fractral distribution of the superconductor local parameters (Fig. 4.11b) similar to that of the wave function counterpart (Fig. 4.10a). These results indicate that at the level of the HLGE, the gap parameters inherite much of the properties of the noninteracting wave functions, sharing a similar localization transition. This no surprise, since the HLGE is contructed exclusively from the noninteracting wave functions and, given that superconductivity is a Fermi level phenomenon, shares the localization properties of the low energy eigenstates.

However, this is where the ALGE starts to diverge from the HLGE. First off, the localization transition happens at a higher critical value for the quasiperiodic potential strength $J_c^{ALGE} \approx 2.36 > J_c$, as we can see in Fig. 4.9. The approximate nature of ALGE does not allow for the the superconductor local parameters to exhibit a fractal distribution for $J = J_c^{ALGE}$, with partial localization around the sites where localization occurs above $J_c^{ALGE}$, as in the HLGE. Instead, there is a transition from an extended to a localized phase with an intermediate phase where the distribution is extended but with a highly fluctuating absolute value, as can be seen in Fig. 4.11c. Nevertheless, the distribution of the superconductor local parameters is also exponentially localized (Fig. 4.11d) above $J_c^{ALGE}$, with peaks centered at the same lattice sites as in the HLGE.

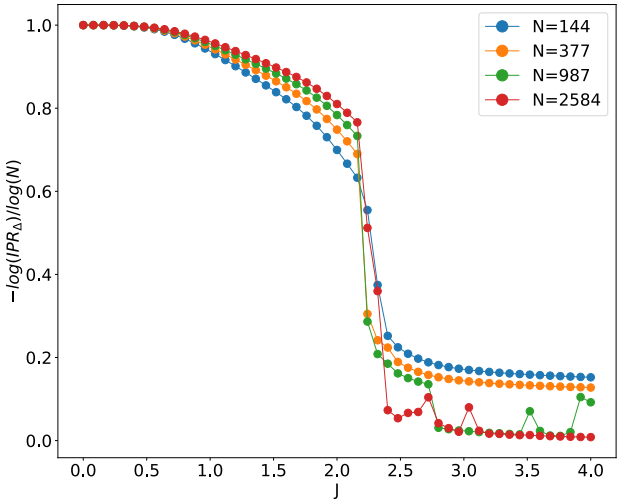


Figure 4.9: $-\log(IPR_\Delta)/\log(N)$ as a function of $J$ for different system sizes up to $N = 2584$, with $g_1 = 0.5$, computed with the ALGE. We can see that the curves converge to a localization transition at $J_c^{ALGE} \approx 2.36$ as we increase the system size, having a similar profile to that of the noninteracting wave functions IPR as shown in Fig. 4.3.

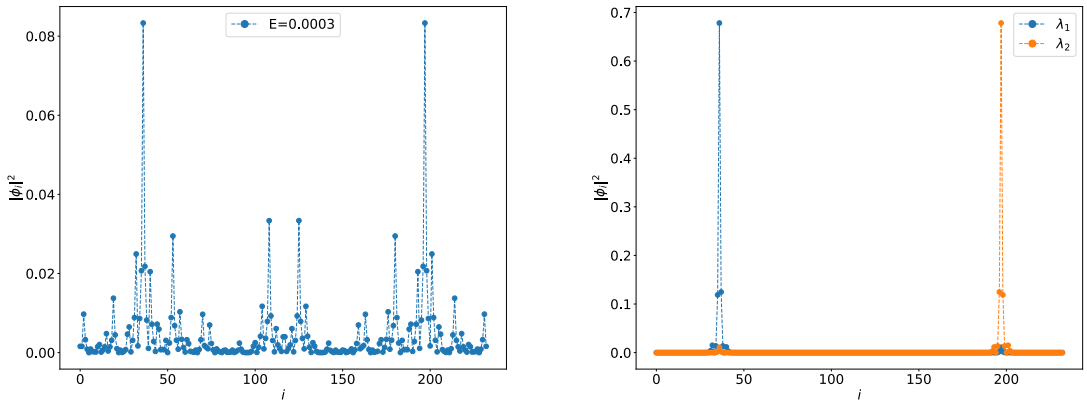


(a) (b)

Figure 4.10: Lattice distribution of the low-energy eigenstates of $\hat{H}_{AAH}$, for a system of size $N = 233$. $(a)$ $J = 2$. Lattice distribution of the wave function $\left|\phi_i^\lambda\right|^2$ closest to zero energy. $E_\lambda = 3 \times 10^{-4}$. $(b)$ $J = 3$. Lattice distribution of the two degenerate wave functions $\left|\phi_i^{\lambda_1}\right|^2$ and $\left|\phi_i^{\lambda_2}\right|^2$ closest to zero energy. $E_{\lambda_1} = E_{\lambda_2} = -1 \times 10^{-2}$.

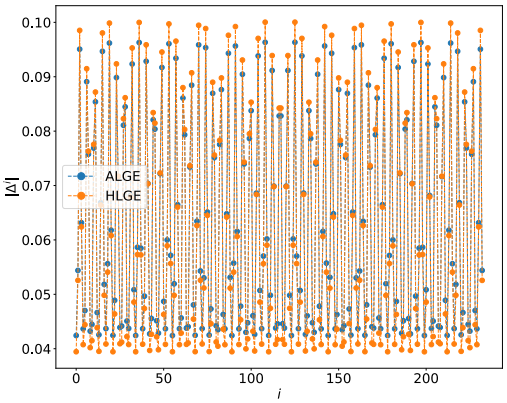


(a) $J = 1$.

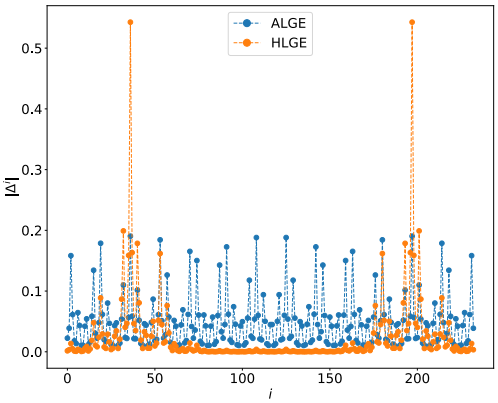


(b) $J = 2$.

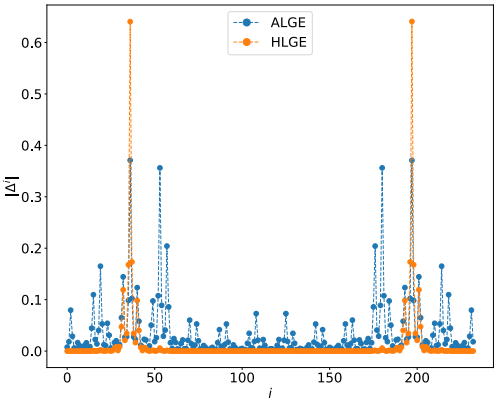


(c) $J_c^{HLGE} < J = 2.25 < J_c^{ALGE}$.

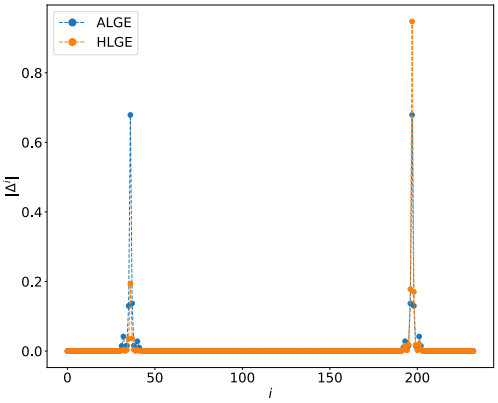


(d) $J = 3$.

Figure 4.11: $\left|\Delta^i\right|$ distribution in the lattice for a system size of $N = 233$ and with $g_1 = 0.5$. The orange plots are computed with the HLGE and the blue plots with the ALGE.

## 4.2 Extended Aubry–André-Harper model

We now turn to a particular variant of the 1D AAH model, whose incommensurability comes not only from the on-site potential but from an incommensurate modulation of the hopping coefficients between nearest-neighbors [49–51]. This variant is of particular interest for our work, since its single-particle phase diagram hosts three kinds of phases: extended, critical and localized.

This system, which we will call the extended Aubry-André model (eAAH), has an Hamiltonian given by

$$\hat{H}_{eAAH} = \sum_{\sigma,m}\left(-t+\nu\cos\left[2\pi Q\left(R_m+\frac{1}{2}\right)\right]\right)\left(c^{\dagger}_{m,\sigma}c_{m+1,\sigma}+c^{\dagger}_{m+1,\sigma}c_{i,\sigma}\right)-J\sum_{\sigma,m}\cos\left(2\pi QR_m\right)c^{\dagger}_{m,\sigma}c_{m,\sigma}, \tag{4.10}$$

where $\nu$ is the strength of the hoppings's incommensurate modulation.

If we fix $J=0$, and study the localization properties of the eigenstates as function of $\nu$, we find that, in similar fashion to the AAH model, there is a well defined transition at $\nu_c=1$. But, unlike the AAH, this time around it is a transition from an extended phase to a critical one as seen in Fig. 4.12.

Relaxing the constraint that $J=0$, we find that this sytem hosts a rich single-particle phase diagram in the $(J,\nu)$ parameter space. In Fig. 4.13, we show the average of the IPR over all eigenstates, $\langle IPR\rangle_{E_\lambda}$, which allows us to distinguish three types of phases: an extended regime, a localized regime and a critical regime. The extended phase is found for $J<J_c$ and $\nu<\nu_c$, the localized phase for $J>2\max(1,\nu)$ and the critical phase for $\nu>\frac{1}{2}\max(2,J)$. In these phases all eigenstates are either extended, localized or critical.

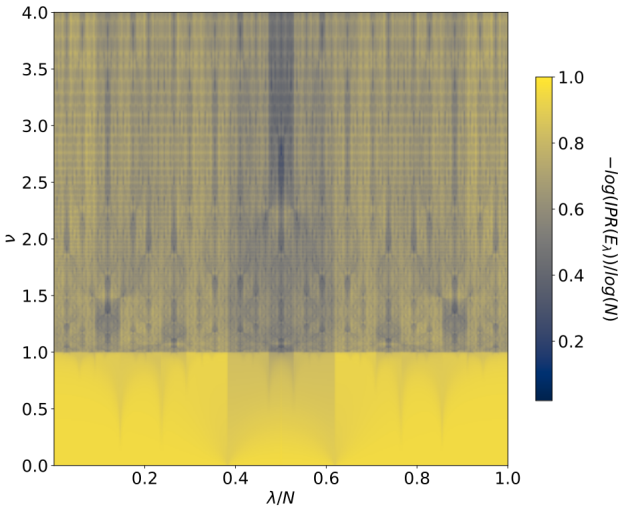


Figure 4.12: $-\log\left(IPR\left(E_\lambda\right)\right)/\log\left(N\right)$ as a function of $\nu$ and the normalized eigenstate index $\frac{\lambda}{N}$, for a system size of $N=2584$. All eigenstates transition from extended to critical at $\nu_c=1$, with $J=0$.

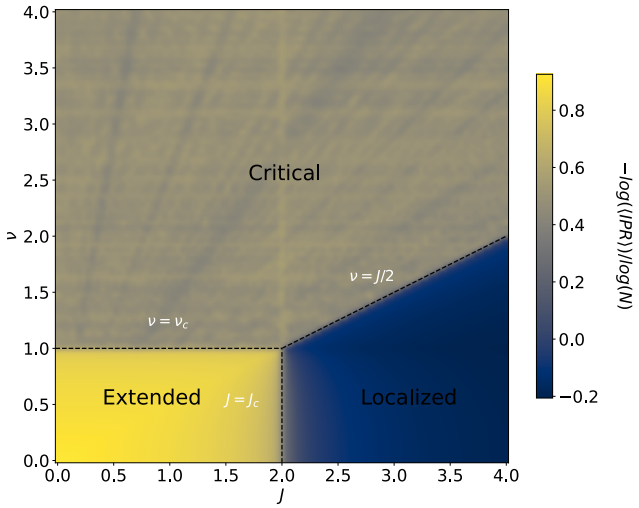


Figure 4.13: $-\log\left(\langle IPR\rangle_{E_\lambda}\right)/\log(N)$ as a function of $(J,\nu)$ where $\langle\ldots\rangle_{E_\lambda}$ means average over all eigenstates. The system size is $N = 987$.

### 4.2.1 Critical temperature

Using the ALGE, we can compute the critical temperature in the $(J,\nu)$ parameter space, shown in Fig. 4.14. If $J < J_c$, there is an enhancement of the critical temperature with an increase in the strength $\nu$ of the hoppings' modulation. Similarly, if $\nu < \nu_c$, we find the behaviour of the AAH model, as $T_c$ increases with $J$. However, it is interesting to notice that for both $J > J_c$ and $\nu > \nu_c$, there is a significant decrease of the critical temperature when there is a competition between the diagonal and off-diagonal quasiperiodicity, i.e., when we have $J \sim \nu$.

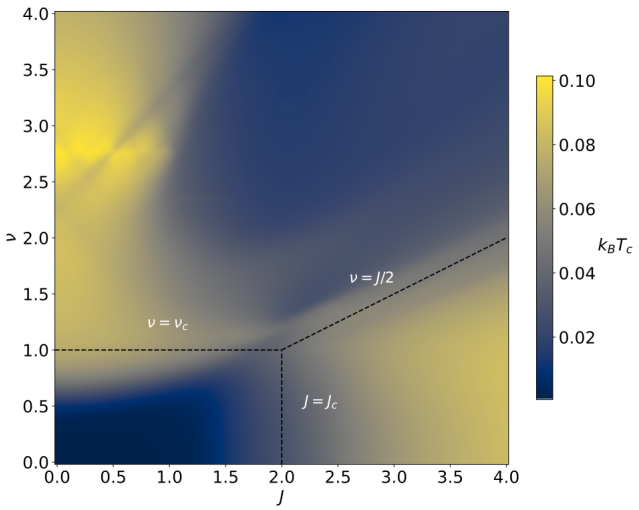


Figure 4.14: $k_B T_c$ as a function of $(J,\nu)$, computed with the ALGE. The system size is $N = 987$ and $g_1 = 0.5$.

We also found a power-law scaling of the critical temperature with the interaction coupling for the

critical regime, i.e., for $\nu > \frac{1}{2}\max(2,J)$, as we show in Fig. 4.15. In the incommensurate limit, we get a power-law $T_c \sim g_1^{1.42\pm0.03}$ with a smaller exponent than the one we found for the critical point $J = J_c$ of the AAH model. In the commensurate limit, we obtain once again the typical BCS scaling.

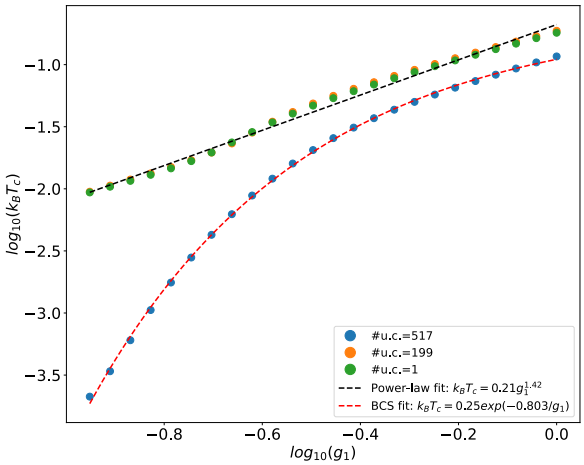


Figure 4.15: $(J,\nu) = (0,2)$. The power-law fit to the $\#u.c. = 1$ curve gives us $k_BT_c = 0.21g_1^{1.42}$, while a BCS fit to the $\#u.c. = 517$ curve gives $k_BT_c = 0.25e^{-0.803/g_1}$.

### 4.2.2 Localization of the superconductor local parameters

Finally, we can look at the localization of the superconductor local parameter in the $(J,\nu)$ parameter space. This will only be done in the context of the ALGE, given that the high computational cost of the HLGE did not allow us to compute a converged phase diagram. For systems of moderate size, such as $N = 987$, the study with the HLGE is already intractable.

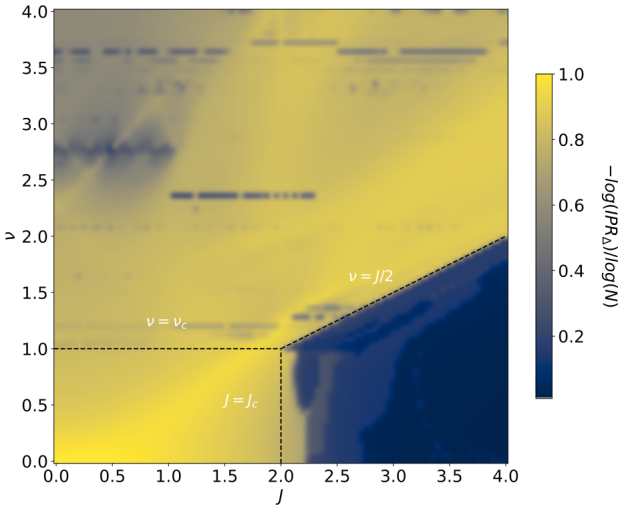


Figure 4.16: $-\log(IPR_\Delta)/\log(N)$ as a function of $(J,\nu)$, computed with the ALGE. The system size is $N = 987$ and $g_1 = 0.5$.

As we can see in Fig. 4.16, the superconductor local parameter phase diagram for $IPR_{\Delta}$, computed with the ALGE, can not capture the three distinct phases we found for the noninteracting wave functions (See Fig. 4.13). The solutions of the ALGE can only reproduce the extended and localized regime, albeit with a shifted transition curve $J_c^{ALGE}(\nu)$ with $J_c^{ALGE}(\nu = 0) = 2.36 > J_c$. The superconductor local parameter phase diagram does not host a well defined critical regime at the level of the ALGE. This can be seen from the lack of a transition at $\nu = \nu_c$ (Fig. 4.16), with the superconductor parameters having an extended nature even for $\nu > \frac{1}{2}\max(2, J)$.

# Chapter 5

# 2D magic-angle semimetals: cTBG

Having studied the connection between superconductivity and incommensurability for 1D quasiperiodic models, we now turn to 2D systems. Motivated by the discovery of sub-ballistic states in the narrow-band regime around the magic angle in tBLG for incommensurate twist angles [20], we wish to investigate if incommensurability in this system plays a role in the scaling of the superconductor critical temperature with the interaction coupling, as it did in the models of the previous chapter.

Recent work by Pixley *et al.* [21] has shown that quasiperiodicity can induce single-particle quantum phase transitions in a class of models called magic-angle semimetals, which have in common the existence of nodes in the band structure and an incommensurate modulation of either the diagonal or the off-diagonal elements of the single-particle Hamiltonian. In this chapter, will use an effective model proposed in [21] for TBG at moderate twist angles in the chiral limit (cTBG).

The Hamiltonian for our cTBG model consists of two sectors corresponding to the Hamiltonians of individual graphene layers along with the coupling of the two layers,

$$\hat{H}_{cTBG} = \hat{H}_1 + \hat{H}_2 + \hat{H}_{12} + \hat{H}_{21}, \tag{5.1}$$

with the kinetic term for each layer $l$ being the usual nearest-neighbor tight-binding model of graphene

$$\hat{H}_l = -t \sum_{\langle \boldsymbol{R}_i, \boldsymbol{R}_j \rangle} c^\dagger_{l,\boldsymbol{R}_i} c_{l,\boldsymbol{R}_j}. \tag{5.2}$$

Obeying $\hat{H}_{21} = \hat{H}^\dagger_{12}$, the two layers are then coupled with a finite-ranged quasiperiodically modulated tunnelling to simulate twisting for moderate angles. The interlayer term, that destroys an eletron in layer 2 and creates it in layer 1, can be written in the momentum space of the single layer graphene as

$$\begin{aligned}\hat{H}_{12} = J \sum_{\boldsymbol{k}} \Bigg[ & c^\dagger_{1,\boldsymbol{k}-\frac{q_1}{2}} \sigma_x c_{2,\boldsymbol{k}+\frac{q_1}{2}} + c^\dagger_{1,\boldsymbol{k}-\frac{q_2}{2}} \left( e^{-i\boldsymbol{k}\cdot\boldsymbol{a}_1}\sigma_+ + e^{i\boldsymbol{k}\cdot\boldsymbol{a}_1}\sigma_- \right) c_{2,\boldsymbol{k}+\frac{q_2}{2}} + c^\dagger_{1,\boldsymbol{k}-\frac{q_3}{2}} \left( e^{-i\boldsymbol{k}\cdot\boldsymbol{a}_2}\sigma_+ + e^{i\boldsymbol{k}\cdot\boldsymbol{a}_2}\sigma_- \right) c_{2,\boldsymbol{k}+\frac{q_3}{2}} \Bigg] \Lambda(\boldsymbol{k}) \\ + J \sum_{\boldsymbol{k}} \Bigg[ & c^\dagger_{1,\boldsymbol{k}+\frac{q_1}{2}} \sigma_x c_{2,\boldsymbol{k}-\frac{q_1}{2}} + c^\dagger_{1,\boldsymbol{k}+\frac{q_2}{2}} \left( e^{-i\boldsymbol{k}\cdot\boldsymbol{a}_1}\sigma_+ + e^{i\boldsymbol{k}\cdot\boldsymbol{a}_1}\sigma_- \right) c_{2,\boldsymbol{k}-\frac{q_2}{2}} + c^\dagger_{1,\boldsymbol{k}+\frac{q_3}{2}} \left( e^{-i\boldsymbol{k}\cdot\boldsymbol{a}_2}\sigma_+ + e^{i\boldsymbol{k}\cdot\boldsymbol{a}_2}\sigma_- \right) c_{2,\boldsymbol{k}-\frac{q_3}{2}} \Bigg] \Lambda(-\boldsymbol{k}),\end{aligned} \tag{5.3}$$

such that $c_{l,\boldsymbol{k}} \equiv \left(c_{l,A,\boldsymbol{k}}, c_{l,B,\boldsymbol{k}}\right)^T$ is defined in terms of the operators $c_{l,A/B,\boldsymbol{k}}$ that create an electron in layer $l$, sublattice $A/B$ and with momentum $\boldsymbol{k}$. The matrices $\{\sigma_i; i = x, y, z\}$ are the usual Pauli matrices in the sublattice subspace, with $\sigma_\pm = \left(\sigma_x \pm i\sigma_y\right)/2$ being the raising and lowering operators. $J$ is the strength of the quasiperiodic tunnelling and $\Lambda(\boldsymbol{k})$ is the function

$$\Lambda(\boldsymbol{k}) \equiv \frac{1}{2} + \frac{1}{6i\sqrt{3}} \sum_{n=1}^{6} (-1)^{n+1} e^{-i\boldsymbol{a}_n \cdot \boldsymbol{k}}. \tag{5.4}$$

The vectors $\{\boldsymbol{a}_n\}$ connect a lattice site to its six nearest Bravais lattice neighbours and can be constructed from the $\boldsymbol{\tau}_i$ nearest neighbors vectors (3.4) as

$$\begin{aligned}
\boldsymbol{a}_1 &= \boldsymbol{\tau}_1 - \boldsymbol{\tau}_2, \\
\boldsymbol{a}_2 &= \boldsymbol{\tau}_1 - \boldsymbol{\tau}_3, \\
\boldsymbol{a}_3 &= \boldsymbol{a}_2 - \boldsymbol{a}_1, \\
\boldsymbol{a}_4 &= -\boldsymbol{a}_1, \\
\boldsymbol{a}_5 &= -\boldsymbol{a}_2, \\
\boldsymbol{a}_6 &= -\boldsymbol{a}_3.
\end{aligned} \tag{5.5}$$

Finally, the vectors $\left\{\boldsymbol{q}_\gamma\right\}$ are defined by

$$\begin{aligned}
\boldsymbol{q}_1 &= k_\theta\,(0, -1)\,, \\
\boldsymbol{q}_2 &= \frac{k_\theta}{2}\left(\sqrt{3}, 1\right), \\
\boldsymbol{q}_3 &= \frac{k_\theta}{2}\left(-\sqrt{3}, 1\right),
\end{aligned} \tag{5.6}$$

where $k_\theta = 2k_D \sin\left(\frac{\theta}{2}\right)$, with $k_D$ being the distance from the $\Gamma$-point to the Dirac cone, encodes the twist angle in our TBG emulator, such that for $\theta \simeq 8.958°$ we have $k_\theta = \frac{4\pi}{3} Q$, with $Q = \frac{1}{\varphi^5}$. Once again, given that $Q$ is written as power of the golden ration $\varphi$, it can be obtained from the Fibonacci sequence in the form of the limit $Q = \lim_{n\to\infty} \frac{F_{n-5}}{F_n}$ which also provides a sequence of rational approximants $Q_n$. The denominator of $Q_n$ defines the linear number of unit cells in our system, i.e., $\#u.c. = F_n$ such that $F_n^2$ is the total number of unit cells in our system.

This model is constructed such that the interlayer coupling of Eq. (5.3) allows our Hamiltonian to be a good approximation for low energies of the full twisted bilayer graphene in the chiral limit for our specified twist angle. It is with this goal in mind that the $\Lambda$ function has the form of Eq. (5.4), since at the Dirac point $\boldsymbol{K}$ we have the limiting values of $\Lambda(\boldsymbol{K}) = 1$ and $\Lambda(-\boldsymbol{K}) = 0$, along with $\boldsymbol{K} \cdot \boldsymbol{a}_1 = -\frac{2\pi}{3}$ and $\boldsymbol{K} \cdot \boldsymbol{a}_2 = \frac{2\pi}{3}$, allowing us to recover the usual low-energy continuum approximation of TBG [6, 9] in the chiral limit

$$\hat{H}_{12} \approx J \sum_{\boldsymbol{k},\gamma} c^\dagger_{1,\boldsymbol{k}-\frac{\boldsymbol{q}_\gamma}{2}} T_\gamma c_{2,\boldsymbol{k}+\frac{\boldsymbol{q}_\gamma}{2}}, \tag{5.7}$$

where the matrices $\{T_\gamma\}$ are given by

$$\begin{aligned} T_1 &= \sigma_x, \\ T_2 &= e^{2\pi i/3}\sigma_+ + e^{-2\pi i/3}\sigma_-, \\ T_3 &= e^{-2\pi i/3}\sigma_- + e^{2\pi i/3}\sigma_-. \end{aligned} \tag{5.8}$$

Having a simple form of the interlayer tunneling that simulates TBG in the low-energy approximation is the main motivation for choosing Eq. (5.3). Another reason for choosing this model is that it translates to a simple real space Hamiltonian that is short-ranged (couples up to nearest-neighbors of order 3) and has a harmonical quasiperiodical modulation of the interlayer hoppings.

After doing a Fourier transform of the $c$-operators, we get that the real space version of our cTBG model is given by the Hamiltonian

$$\begin{aligned} \hat{H}_{12} = J \sum_{\boldsymbol{R},\gamma} \Bigg\{ &\left( c^\dagger_{1,\boldsymbol{R}+\boldsymbol{s}_\gamma} \sigma_+ c_{2,\boldsymbol{R}} + c^\dagger_{1,\boldsymbol{R}} \sigma_- c_{2,\boldsymbol{R}+\boldsymbol{s}_\gamma} \right) \cos\left[ \boldsymbol{q}_\gamma \cdot \left( \boldsymbol{R} + \frac{\boldsymbol{s}_\gamma}{2} \right) \right] \\ &+ \frac{1}{3\sqrt{3}} \sum_{n=1}^{6} (-1)^{n+1} \left( -c^\dagger_{1,\boldsymbol{R}+\boldsymbol{a}_n+\boldsymbol{s}_\gamma} \sigma_+ c_{2,\boldsymbol{R}} + c^\dagger_{1,\boldsymbol{R}} \sigma_- c_{2,\boldsymbol{R}+\boldsymbol{a}_n+\boldsymbol{s}_\gamma} \right) \sin\left[ \boldsymbol{q}_\gamma \cdot \left( \boldsymbol{R} + \frac{(\boldsymbol{s}_\gamma + \boldsymbol{a}_n)}{2} \right) \right] \Bigg\}. \end{aligned} \tag{5.9}$$

where

$$\begin{aligned} \boldsymbol{s}_1 &= (0,0), \\ \boldsymbol{s}_2 &= -\boldsymbol{a}_1, \\ \boldsymbol{s}_3 &= -\boldsymbol{a}_2. \end{aligned} \tag{5.10}$$

One of the most interesting features of this model is the narrow miniband that forms in the metallic regime, similar to the one that exists in TBG. As we can see in Fig. 5.1, the miniband is quite isolated at the center of the spectrum, separated from the higher energy bands by a gap of a order of magnitude greater that its bandwidth $\Delta E \sim 0.01$ (As before, all energy values will be in units of $t$ thoughout the rest of this chapter).

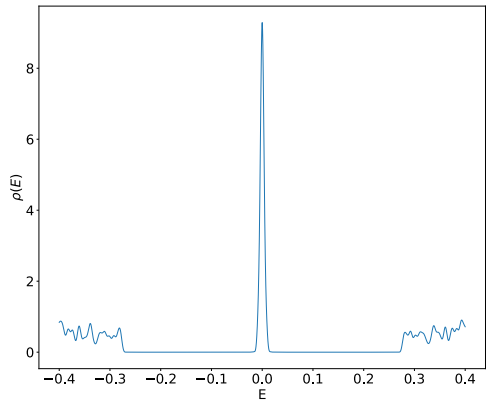


Figure 5.1: $\rho(E)$ computed with KPM for a system of size $L = 4 \cdot N^2 = 4 \cdot 144^2$ at the critical point of the semimetal-metal transition (See section (5.1) for discussion).

## 5.1 Semimetal-metal transition

As we know, in the clean limit $J \to 0$, the cTBG Hamiltonian (5.1) reduces to two copies of single layer graphene and, as such, is a semimetal that has two Dirac cones with a density of states (DOS) that vanishes linearly at the Fermi level. The interesting property of this model, that puts it in the magic-angle semimetals class, is that it hosts a semimetal-metal phase transition for a critical value $J_c$ of the interlayer tunneling (5.9). In fact, it hosts a metallic phase for a small range of values of the tunneling strength $J_c < J < J_c'$, with a reentrant semimetal phase for $J > J_c'$ (See Fig. (5.3)).The signature of this metallic phase is the formation of a narrow miniband at zero energy that is associated with critical zero energy wave functions that partially delocalize in momentum space (See Fig. (5.2)).

In order to study the formation of the flat miniband and determine the critical values of $J$, we will need to compute the DOS at zero energy. However, to clearly capture the semimetal-metal transition we need to study Hamiltonians of considerable size in real space. For example, a typical rational approximant that we will use for the inverse of the wavelength of the tunneling modulation is $Q = \frac{13}{144}$. For this choice of $Q$, the dimension of our Hilbert space, taking into account the two layers and the two sublattice degrees of freedom, is of order $L \sim 10^5$ which already makes exact diagonalization an expensive computational task.

Having this in mind, for the purpose of computing the DOS we will be using a technique that has become standard in recent years in condensed matter physics called the kernel polynomial method (KPM) (See Ref. [52]), which is an efficient method for computing spectral quantities, that scales linearly with the dimensionality of the Hamiltonian, making it an excellent alternative to exact diagonalization. As for the low energy wave functions, we used the implicitly restarted Lanczos method included in the numerical software library ARPACK [53], which is useful to compute a few eigenvalues and eigenvectors of large sparce matrices.

Regarding the eigenstates near the Fermi level (the Dirac energy $E = 0$), they are adiabatically connected to those in the clean limit $J = 0$ and are ballistic in momentum space, for $J < J_c$, i.e., in the semimetal

regime. As we can see in Fig. 5.2, they are localized in momentum space with peaks at the Dirac cones and, as we transition to the metallic regime at $J = J_c$, they start to delocalize and become critical, displaying a "multifractal" profile with partial localization around the $\boldsymbol{K}$-points. This multifractality can be investigated numerically by studying the non-linear multifractal behaviour of the scaling exponent $\tau(q)$, that can be computed from the momentum space IPR, $\sum_{\boldsymbol{k}} |\varphi_{\boldsymbol{k}}(E=0)|^4 \sim L^{-\tau(q)}$, as it is done in Ref. [21].

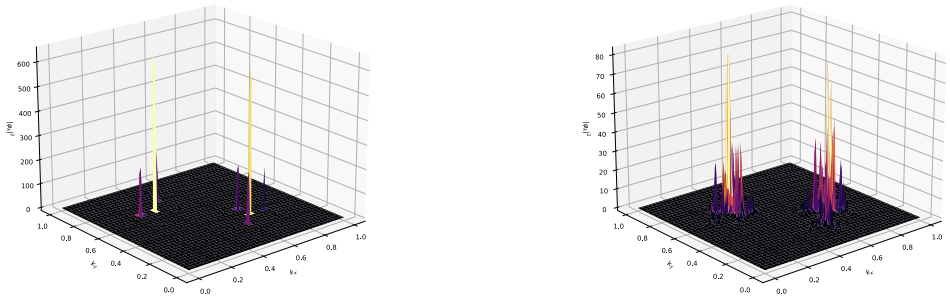

(a) $J = 0.29 < J_c$.

(b) $J = 0.313 = J_c$.

Figure 5.2: Plot of $\left|\varphi_{\boldsymbol{k}}^{l=1}(E=0)\right|^2$,i.e., the Fourier transform of the zero energy wavefunction for the $l = 1$ layer. Computed for a system of size $L = 4 \cdot 144^2$.

However, these systems have a major difference relative to the 1D models we previously studied, regarding the critical value at which the transition occurs. In this case, even though the IPR loses its signature in the metallic phase as we increase the number of unit cells, we can still compute a critical value for the semimetal-metal transition from the DOS at the Dirac energy alone. It turns out that this critical value depends on the rational approximant chosen, i.e., the critical value of the quasiperiodic tunneling strength is a function of the interlayer hoppings modulation wavelength $J_c(Q)$. We can think that by changing $Q$ we are changing the twist angle our effective model, which changes the physical system we are studying. It should not be expected that for different systems we would obtain the same critical value for the semimetal-metal transition.

By fixing the system size, we can study the DOS at zero energy, $\rho(0)$, as a function of both the quasiperiodic tunneling strength $J$ and the inverse of the wavelength $Q$. The semimetal-metal phase diagram, determined by $\rho(0)$, can be seen in Fig. 5.3, where it is clear that the system hosts a metallic phase in a thin strip of the $(Q, J)$ plane located between two critical curves $J_c(Q)$ and $J_c'(Q)$ that separates it from an otherwise semimetallic regime. Hence, if we wish to study a system with more unit cells, to do a finite size scaling and to compare the commensurate with the incommensurate case, we always need to compute the critical value $J_c$ for that particular rational approximant.

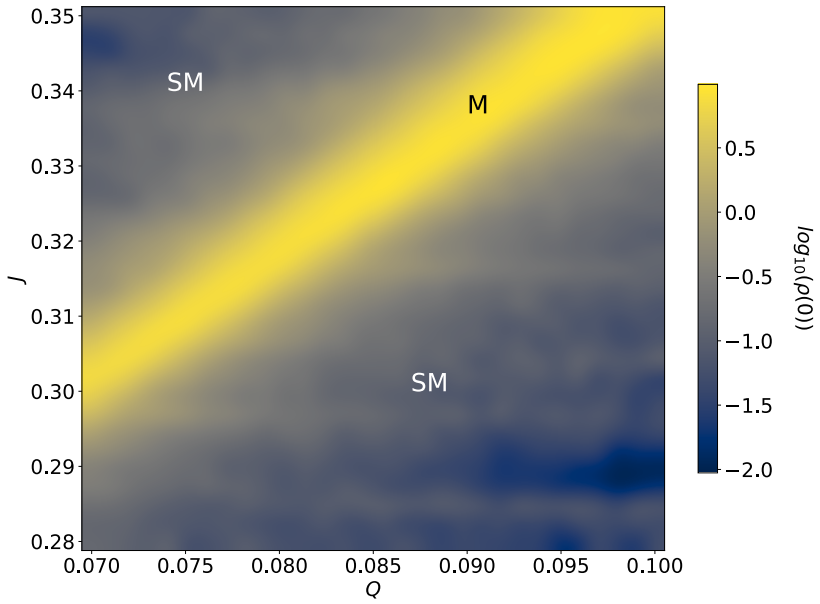


Figure 5.3: $\rho\,(E=0)$, computed with KPM, as a function of $Q$ and $J$. The system size is $L = 4 \cdot 144^2$ and we used the Jackson kernel with $N_c = 2^{12}$ Chebyshev polynomials and $N_R = 1$ random vectors for the stochastic trace evaluation.

## 5.2 Critical temperature results

To study superconductivity in this system, we will use the ALGE with a energy cutoff, since it is the only feasible numerical method for systems of this size, where we can only acess a few eigenstates. The average theoretical Debye energy of the three acoustic phonon modes in graphene is of order $\omega_D \sim 0.1$ [54]. This will serve as motivation to pick a cutoff in energy close to $\omega_D$, so that the only states that will contribute to the structure of the ALGE are those within the miniband, given that the bandwidth of the miniband is of order $\Delta E \sim 0.01$.

In order to study the ALGE with a cutoff, we need to know how many states there are inside the miniband for each rational approximant $Q_n$. This is a necessary step, given that we have to fix the dimensionality of the ALGE in order to know how many eigenvalues and eigenvectors of $\hat{H}_{cTBG}$ we must compute with the Lanczos algorithm. Since we do not have access to the whole spectrum, because we did not fully diagonalize the Hamiltonian, we will have to compute the number of states within the energy cutoff window with KPM.

This procedure can be summarized as follows:

1. Fix the rational approximant $Q_n$ and compute the critical value $J_c\,(Q_n)$ by analysing $\rho_{KPM}\,(0)$;

2. Compute the number of states within the Debye energy window as

$$N_{\text{miniband}} = N \int_{-\omega_D}^{\omega_D} \rho_{KPM}\,(\varepsilon)\, d\varepsilon; \tag{5.11}$$

3. Use the Lanczos algorithm, with shift-invert, to obtain the set of $N_{\text{miniband}}$ eigenvalues and eigenvectors of $\hat{H}_{cTBG}$ closest to zero energy.

4. Compute the critical temperature and the superconductor gap parameters with the ALGE for this truncated eigenspace.

In the metalic regime, we found an almost linear scaling of $T_c$ with $g_1$ for moderate values of $g_1$, as shown in Fig. 5.4. This stands in contrast with the power-law $T_c \sim g_1^{\eta}$ with a larger scaling exponent $\eta$ we computed in the 1D quasiperiodic models, such as the one found for the critical point the AAH model (Fig. 4.5a) or the one found for the critical regime of the eAHH model (Fig. 4.15). We suspect that this power-law with a diminished exponent is due to the restrictive imposition we made with our choice of energy cutoff. Recalling the results for the AAH model in Fig. 4.7, we showed that imposing a very restrictive energy cutoff could reduce the power-law in the critical regime into a simple linear scaling.

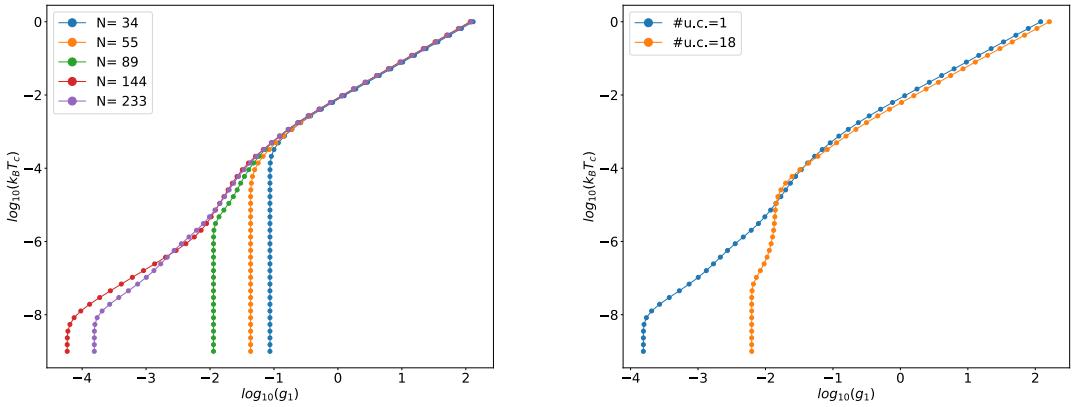


(a) (b)

Figure 5.4: $T_c$ as a function of $g_1$, for sizes up to $L = 4 \cdot N^2 = 4 \cdot (233)^2$ and with an energy cutoff of $\omega_D = 0.1$. $(a)$ Incommensurate systems: Critical temperature scaling for $J_c = 0.313$, computed for different systems sizes from $L_1 = 4 \cdot N_1^2 = 4 \cdot (34)^2$, corresponding to the rational approximant $Q_1 = \frac{1}{13}$, up to $L_5 = 4 \cdot N_5^2 = 4 \cdot (233)^2$, corresponding to the the rational approximant $Q_5 = \frac{21}{233}$. $(b)$ Critical temperature scaling in the commensurate and in the incommensurate limit. The incommensurate limit corresponds to a system with 1 unit cell, corresponding to $Q_{\#u.c.=1} = \frac{21}{233}$ with a system size of $L_{\#u.c.=1} = 4 \cdot (233)^2$ at $J_c\,(Q_{\#u.c.=1}) = 0.313$. The commensurate limit is the system with $18 \times 18$ unit cells, corresponding to $Q_{\#u.c.=18} = \frac{1}{13}$ with a system size of $L_{\#u.c.=1} = 4 \cdot (234)^2$ at $J_c\,(Q_{\#u.c.=18}) = 0.270$.

The role of incommensurability seems to come into play in the weak-coupling regime, i.e., for small values of $g_1$. As we see in Fig. 5.4b, the incommensurability of the single-particle Hamiltonian seems to promote superconductivity, since the curve for the incommensurate case seems to present a higher critical temperature than the commensurate case in this regime. As we decrease the interaction coupling below the linear scaling regime, the commensurate and incommensurate curves diverge, with the critical temperature falling much faster to zero in the commensurate case. The fact that critical couplings appear, i.e., minimum values of $g_1^c$ below which superconductivity does not develop at finite temperatures, is reminiscent of what

we found in Chapter 3 for single layer graphene, albeit with much higher values of $g_1^c$ in that case. Although it seems that in the incommensurate case the critical coupling is smaller, there is still work to be done to find out if the origin of this difference in minimum couplings is really an effect of incommensurability or if it is a numerical error of the ALGE. It could happen that due to $g_1$ being very small, we could be dealing with an interaction energy scale that competes with the average spacing of levels in the spectrum of our single-particle Hamiltonian. Future work will attempt to ascertain this with a more detailed finite size analysis.

# Chapter 6

# Conclusion

In this thesis, we studied the interplay between superconductivity, localization and incommensurability in a set of tight-binding 1D and 2D systems.

Within a Green's function approach to superconductivity, we deduced a linearized gap equation in order to study the superconductor critical temperature and the corresponding superconductor gap parameters, for an arbitrary single-particle Hamiltonian, with a general two-body interaction term.

We investigated an extended Hubbard interaction in single layer graphene, with both a momentum and real space treatment, and found the existence of a critical value for both the on-site and the nearest-neighbor interaction coupling parameter, when the chemical potential is at the Dirac energy. If any of the coupling parameters are below these critical values, the development of superconductivity, associated with a finite value of the critical temperature, is forbidden due to the semimetallic nature of graphene, for which the density of states vanishes at the chemical potential.

Having studied this commensurate case, we moved on to a set of incommensurate systems, both 1D and 2D. We started by studying the classical Aubry-André-Harper model with an Hubbard attractive term, for which the on-site superconductor gap parameters exhibit, similarly to the eigenstates of the noninteracting systems, a transition from an extended regime to a localized regime. This transition is accompanied by an increase of the superconductor critical temperature with the strength of the quasiperiodic potential strength. It was found that the critical temperature exhibits a power-law scaling with the interaction coupling, with characteristic exponents for both the critical and the localized regime, which is due to the incommensurate nature of this 1D model. We found similar results for an extended variant of this 1D model which features a quasiperiodical modulation of the nearest-neighbor hoppings, with a power-law scaling of the critical temperature inside the critical regime.

As for the 2D case, we studied a magic-angle semimetal model which emulates twisted bilayer graphene in the chiral limit. For the metallic phase of this model, we found that the critical temperature has a linear scaling for moderate values of the interaction coupling but appears to be enhanced due to incommensurability in the weak interaction coupling regime. Future work with a more detailed finite size analysis is required to verify these results.

# Appendix A

# Bogoliubov-de Gennes Method

The purpose of this appendix is to show how we can use a mean-field method, called the Bogoliubov-de Gennes method, to compute the superconductor gap parameters as a function of temperature. We will also show that this method is not adequate to compute the superconductor critical temperature.

For concreteness, we will focus on the case of a system with an on-site Hubbard interaction that conserves spin,

$$\begin{aligned}\hat{H} &= \sum_{\sigma}\sum_{i,j} h_{i,j} c^{\dagger}_{i\sigma} c_{j\sigma} - \frac{g_1}{2}\sum_{s}\sum_{i} c^{\dagger}_{i,s} c^{\dagger}_{i,-s} c_{i,-s} c_{i,s} \\ &= \sum_{\sigma}\sum_{i,j} h_{i,j} c^{\dagger}_{i\sigma} c_{j\sigma} - g_1 \sum_{i} c^{\dagger}_{i\uparrow} c^{\dagger}_{i\downarrow} c_{i\downarrow} c_{i\uparrow}. \end{aligned} \tag{A.1}$$

We can do a mean-field decoupling in the Cooper channel by first introducing the fluctuations

$$d_i \equiv c_{i\downarrow} c_{i\uparrow} - \left\langle c_{i\downarrow} c_{i\uparrow} \right\rangle, \tag{A.2}$$

which allows to rewrite the Hamiltonian (A.1) as

$$\hat{H} = \sum_{\sigma}\sum_{i,j} h_{i,j} c^{\dagger}_{i\sigma} c_{j\sigma} - g_1 \sum_{i} \left( d^{\dagger}_i + \left\langle c^{\dagger}_{i\uparrow} c^{\dagger}_{i\downarrow} \right\rangle \right) \left( d_i + \left\langle c_{i\downarrow} c_{i\uparrow} \right\rangle \right),$$

and, ignoring the bilinear terms $d^{\dagger}_i d_i$ in the fluctuations, we get the mean-field Hamiltonian

$$\hat{H}_{MF} = \sum_{\sigma}\sum_{i,j} h_{i,j} c^{\dagger}_{i\sigma} c_{j\sigma} - g_1 \sum_{i} \left[ c^{\dagger}_{i\uparrow} c^{\dagger}_{i\downarrow} \left\langle c_{i\downarrow} c_{i\uparrow} \right\rangle + c_{i\downarrow} c_{i\uparrow} \left\langle c^{\dagger}_{i\uparrow} c^{\dagger}_{i\downarrow} \right\rangle - \left\langle c_{i\downarrow} c_{i\uparrow} \right\rangle \left\langle c^{\dagger}_{i\uparrow} c^{\dagger}_{i\downarrow} \right\rangle \right].$$

The superconductor gap parameter can be defined as

$$\Delta_i \equiv g_1 \left\langle c_{i\uparrow} c_{i\downarrow} \right\rangle, \tag{A.3}$$

such that the mean-field Hamiltonian takes the simple form

$$\hat{H}_{MF} = \sum_{\sigma}\sum_{i,j} h_{i,j} c^{\dagger}_{i\sigma} c_{j\sigma} + \sum_{i}\left[\Delta_i c^{\dagger}_{i\uparrow} c^{\dagger}_{i\downarrow} + \Delta^{*}_{i} c_{i\downarrow} c_{i\uparrow}\right] + \sum_{i} \frac{|\Delta_i|^2}{g_1}. \tag{A.4}$$

Equipped with this mean-field Hamiltonian, we can compute the following commutators

$$\begin{aligned}\left[c_{i\uparrow}, \hat{H}_{MF}\right] &= \sum_{\sigma}\sum_{m,j} h_{m,j}\left[c_{i\uparrow}, c^{\dagger}_{m\sigma} c_{j\sigma}\right] + \sum_{j}\Delta_j\left[c_{i\uparrow}, c^{\dagger}_{j\uparrow} c^{\dagger}_{j\downarrow}\right] + \Delta^{*}_{j}\left[c_{i\uparrow}, c_{j\downarrow} c_{j\uparrow}\right] \\ &= \sum_{j} h_{i,j} c_{j\uparrow} + \Delta_i c^{\dagger}_{i\downarrow},\end{aligned} \tag{A.5}$$

where we used the fermionic anti-commutation relations

$$\begin{aligned}\left\{c_{i\sigma}, c^{\dagger}_{j\sigma}\right\} &= \delta_{ij} \\ \left\{c_{i\sigma}, c_{j\sigma}\right\} &= \left\{c^{\dagger}_{i\sigma}, c^{\dagger}_{j\sigma}\right\} = 0.\end{aligned} \tag{A.6}$$

Similarly, we can compute the other commutators

$$\left[c^{\dagger}_{i\uparrow}, \hat{H}_{MF}\right] = -\sum_{j} h_{j,i} c^{\dagger}_{j\uparrow} - \Delta^{*}_{i} c_{i\downarrow}, \tag{A.7}$$

$$\left[c_{i\downarrow}, \hat{H}_{MF}\right] = \sum_{j} h_{i,j} c_{j\downarrow} - \Delta_i c^{\dagger}_{i\uparrow}, \tag{A.8}$$

$$\left[c^{\dagger}_{i\downarrow}, \hat{H}_{MF}\right] = -\sum_{j} h_{j,i} c^{\dagger}_{j\downarrow} + \Delta^{*}_{i} c_{i\uparrow}. \tag{A.9}$$

From looking at the previous commutators we can see that our eletron field operators are a linear combination of particle and hole quasiparticle excitations. We can then do a Bogoliubov canonical transformation of the form

$$\begin{aligned}c_{i\sigma} &= \sum_{n}{}' \left[u^{n}_{i\sigma}\gamma_n - \sigma v^{n,*}_{i\sigma}\gamma^{\dagger}_{n}\right] \\ c^{\dagger}_{i\sigma} &= \sum_{n}{}' \left[u^{n,*}_{i\sigma}\gamma^{\dagger}_{n} - \sigma v^{n}_{i\sigma}\gamma_n\right],\end{aligned} \tag{A.10}$$

such that the Bogoliubov quasiparticle operators obey the canonical anti-commutation relations

$$\begin{aligned}\left\{\gamma_n, \gamma^{\dagger}_{m}\right\} &= \delta_{nm} \\ \{\gamma_n, \gamma_m\} &= \left\{\gamma^{\dagger}_{n}, \gamma^{\dagger}_{m}\right\} = 0.\end{aligned} \tag{A.11}$$

This canonical transformation diagonalizes our Hamiltonian:

$$\hat{H}_{MF} = E_0 + \sum_n{}' E_n \gamma_n^\dagger \gamma_n,$$

where the $'$ means that we only sum over positive eigenvalues $E_n$, implying that we must have the commutations relations

$$\begin{aligned}\left[\gamma_n^\dagger, \hat{H}_{MF}\right] &= -E_n \gamma_n^\dagger \\ \left[\gamma_n, \hat{H}_{MF}\right] &= E_n \gamma_n. \end{aligned} \tag{A.12}$$

If we compare this commutations relations with those for $c_{i\sigma}^\dagger$ and $c_{i\sigma}$ term by term, we find that

$$\left[c_{i\uparrow}, \hat{H}_{MF}\right] = \sum_n{}' \left[u_{i\uparrow}^n \left[\gamma_n, \hat{H}_{MF}\right] - v_{i\uparrow}^{n,*} \left[\gamma_n^\dagger, \hat{H}_{MF}\right]\right]$$

$$\sum_n{}' \left[\sum_j h_{i,j} u_{j\uparrow}^n + \Delta_i v_{i\downarrow}^n\right] \gamma_n + \left[-\sum_j h_{i,j} v_{j\uparrow}^{n,*} + \Delta_i u_{i\downarrow}^{n,*}\right] \gamma_n^\dagger = \sum_n{}' E_n u_{i\uparrow}^n \gamma_n + E_n v_{i\uparrow}^{n,*} \gamma_n^\dagger,$$

which implies

$$\begin{aligned} E_n u_{i\uparrow}^n &= \sum_j h_{i,j} u_{j\uparrow}^n + \Delta_i v_{i\downarrow}^n \\ E_n v_{i\uparrow}^n &= -\sum_j h_{i,j}^* v_{j\uparrow}^n + \Delta_i^* u_{i\downarrow}^n \end{aligned}$$

and, similarly, we get

$$\left[c_{i\downarrow}, \hat{H}_{MF}\right] = \sum_n{}' \left[u_{i\downarrow}^n \left[\gamma_n, \hat{H}_{MF}\right] + v_{i\downarrow}^{n,*} \left[\gamma_n^\dagger, \hat{H}_{MF}\right]\right]$$

$$\sum_n{}' \left[\sum_j h_{i,j} u_{j\downarrow}^n + \Delta_i v_{i\uparrow}^n\right] \gamma_n + \left[\sum_j h_{i,j} v_{j\downarrow}^{n,*} - \Delta_i u_{i\uparrow}^{n,*}\right] \gamma_n^\dagger = \sum_n{}' E_n u_{i\downarrow}^n \gamma_n - E_n v_{i\downarrow}^{n,*} \gamma_n^\dagger,$$

implying

$$\begin{aligned} E_n u_{i\downarrow}^n &= \sum_j h_{i,j} u_{j\downarrow}^n + \Delta_i v_{i\uparrow}^n \\ E_n v_{i\downarrow}^n &= -\sum_j h_{i,j}^* v_{j\downarrow}^n + \Delta_i^* u_{i\uparrow}^n. \end{aligned}$$

This set of equations can be cast in matrix format as

$$\sum_{i,j} \Omega_{i,j} \phi_j^n = E_n \phi_i^n, \tag{A.13}$$

where

$$\left(\Omega_{i,j}\right) = \begin{pmatrix} h_{i,j} & 0 & 0 & \Delta_i\delta_{i,j} \\ 0 & h_{i,j} & \Delta_i\delta_{i,j} & 0 \\ 0 & \Delta_i^*\delta_{i,j} & -h_{i,j}^* & 0 \\ \Delta_i^*\delta_{i,j} & 0 & 0 & -h_{i,j}^* \end{pmatrix} \tag{A.14}$$

and

$$\phi_i^n = \begin{pmatrix} u_{i\uparrow}^n \\ u_{i\downarrow}^n \\ v_{i\uparrow}^n \\ v_{i\downarrow}^n \end{pmatrix}. \tag{A.15}$$

The BdG Eqs. (A.13), due to the absence of spin-orbit coupling and spin-flip scattering terms, can be block-diagonalized into two sets of equations

$$\begin{pmatrix} h_{i,j} & \Delta_i\delta_{i,j} \\ \Delta_i^*\delta_{i,j} & -h_{i,j}^* \end{pmatrix} \begin{pmatrix} u_{i\uparrow}^{\tilde{n}1} \\ v_{i\downarrow}^{\tilde{n}1} \end{pmatrix} = E_{\tilde{n}1} \begin{pmatrix} u_{i\uparrow}^{\tilde{n}1} \\ v_{i\downarrow}^{\tilde{n}1} \end{pmatrix} \tag{A.16}$$

$$\begin{pmatrix} h_{i,j} & \Delta_i\delta_{i,j} \\ \Delta_i^*\delta_{i,j} & -h_{i,j}^* \end{pmatrix} \begin{pmatrix} u_{i\downarrow}^{\tilde{n}2} \\ v_{i\uparrow}^{\tilde{n}2} \end{pmatrix} = E_{\tilde{n}2} \begin{pmatrix} u_{i\downarrow}^{\tilde{n}2} \\ v_{i\uparrow}^{\tilde{n}2} \end{pmatrix}. \tag{A.17}$$

This block-diagonalization leads to the following modified canonical transformation:

$$\begin{aligned} c_{i\uparrow} &= {\sum_{\tilde{n}}}' \left[ u_{i\uparrow}^{\tilde{n}1}\gamma_{\tilde{n}1} - v_{i\uparrow}^{\tilde{n}2,*}\gamma_{\tilde{n}2}^\dagger \right] \\ c_{i\uparrow}^\dagger &= {\sum_{\tilde{n}}}' \left[ u_{i\uparrow}^{\tilde{n}1,*}\gamma_{\tilde{n}1}^\dagger - v_{i\uparrow}^{\tilde{n}2}\gamma_{\tilde{n}2} \right], \end{aligned} \tag{A.18}$$

$$\begin{aligned} c_{i\downarrow} &= {\sum_{\tilde{n}}}' \left[ u_{i\downarrow}^{\tilde{n}2}\gamma_{\tilde{n}2} + v_{i\downarrow}^{\tilde{n}1,*}\gamma_{\tilde{n}1}^\dagger \right] \\ c_{i\downarrow}^\dagger &= {\sum_{\tilde{n}}}' \left[ u_{i\downarrow}^{\tilde{n}2,*}\gamma_{\tilde{n}2}^\dagger + v_{i\downarrow}^{\tilde{n}1}\gamma_{\tilde{n}1} \right]. \end{aligned} \tag{A.19}$$

Using this and the fact that if $\left(u_{i\uparrow}^n, v_{i\downarrow}^n, u_{i\downarrow}^n, v_{i\uparrow}^n\right)$ is a solution to the BdG equations with eigenvalue $E_n$, then $\left(-v_{i\uparrow}^{n,*}, u_{i\downarrow}^{n,*}, v_{i\downarrow}^{n,*}, -u_{i\uparrow}^{n,*}\right)$ is also a solution with eigenvalue $-E_n$, we obtain the the following self-consistency

condition:

$$
\begin{aligned}
\Delta_i &= \frac{g_1}{2}\left\langle c_{i\uparrow}c_{i\downarrow}\right\rangle - \frac{g_1}{2}\left\langle c_{i\downarrow}c_{i\uparrow}\right\rangle \\
&= \frac{g_1}{2}\sum_{\tilde{n},\tilde{m}}{}'\left\langle\left[u_{i\uparrow}^{\tilde{n}1}\gamma_{\tilde{n}1} - v_{i\uparrow}^{\tilde{n}2,*}\gamma_{\tilde{n}2}^{\dagger}\right]\left[u_{i\downarrow}^{\tilde{m}2}\gamma_{\tilde{m}2}+v_{i\downarrow}^{\tilde{m}1,*}\gamma_{\tilde{m}1}^{\dagger}\right]\right\rangle \\
&\quad - \frac{g_1}{2}\sum_{\tilde{n},\tilde{m}}{}'\left\langle\left[u_{i\downarrow}^{\tilde{n}2}\gamma_{\tilde{n}2}+v_{i\downarrow}^{\tilde{n}1,*}\gamma_{\tilde{n}1}^{\dagger}\right]\left[u_{i\uparrow}^{\tilde{m}1}\gamma_{\tilde{m}1} - v_{i\uparrow}^{\tilde{m}2,*}\gamma_{\tilde{m}2}^{\dagger}\right]\right\rangle \\
&= \frac{g_1}{2}\sum_{\tilde{n}}{}'\left[u_{i\uparrow}^{\tilde{n}1}v_{i\downarrow}^{\tilde{n}1,*}f\left(-E_{\tilde{n}1}\right) - v_{i\uparrow}^{\tilde{n}2,*}u_{i\downarrow}^{\tilde{n}2}f\left(E_{\tilde{n}2}\right)\right] \\
&\quad - \frac{g_1}{2}\sum_{\tilde{n}}{}'\left[-u_{i\downarrow}^{\tilde{n}2}v_{i\uparrow}^{\tilde{n}2,*}f\left(-E_{\tilde{n}2}\right) + v_{i\downarrow}^{\tilde{n}1,*}u_{i\uparrow}^{\tilde{n}1}f\left(E_{\tilde{n}1}\right)\right] \\
&= \frac{g_1}{2}\sum_{\tilde{n}}{}'u_{i\uparrow}^{\tilde{n}1}v_{i\downarrow}^{\tilde{n}1,*}\left[f\left(-E_{\tilde{n}1}\right) - f\left(E_{\tilde{n}1}\right)\right] + u_{i\downarrow}^{\tilde{n}2}v_{i\uparrow}^{\tilde{n}2,*}\left[f\left(-E_{\tilde{n}2}\right) - f\left(E_{\tilde{n}2}\right)\right] \\
&= \frac{g_1}{2}\sum_{\tilde{n}}{}'u_{i\uparrow}^{\tilde{n}1}v_{i\downarrow}^{\tilde{n}1,*}\tanh\left(\frac{E_{\tilde{n}1}}{2k_BT}\right) + u_{i\downarrow}^{\tilde{n}2}v_{i\uparrow}^{\tilde{n}2,*}\tanh\left(\frac{E_{\tilde{n}2}}{2k_BT}\right) \\
&= \frac{g_1}{2}\sum_{\tilde{n}}u_{i\uparrow}^{\tilde{n}1}v_{i\downarrow}^{\tilde{n}1,*}\tanh\left(\frac{E_{\tilde{n}1}}{2k_BT}\right).
\end{aligned}
\tag{A.20}
$$

Solving (A.13) constrained to the condition (A.20), allows us to compute the superconductor gap parameters self-consistently. If we define a vector $\vec{\Delta}^{\alpha}$, whose components are the superconductor gap parameters $\{\Delta_i\}$ at iteration $\alpha$, then we can define the relative residual error as

$$
\delta\Delta \equiv \frac{\left\|\vec{\Delta}^{\alpha} - \vec{\Delta}^{\alpha-1}\right\|}{\left\|\vec{\Delta}^{\alpha}\right\|}. \tag{A.21}
$$

As we can see in Fig. A.1, the number of iterations required to achieve convergence within a tolerance of $\delta\Delta = 10^{-6}$ has its maximum where the average $\langle|\Delta_i|\rangle$ over the lattice of the superconductor gap parameters goes to zero, i.e., at the critical temperature of the system. Therefore, the Bogoliubov-de Gennes method is not suitable for computing the superconductor critical temperature, due to its slow convergence near this temperature. A more suitable method is the linearized gap equation that we used throughout this thesis.

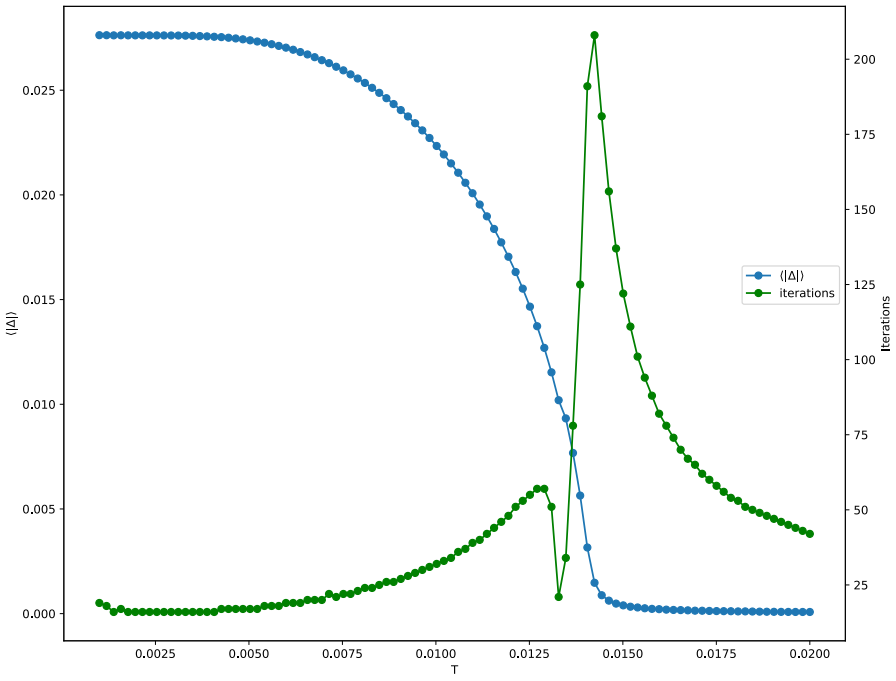


Figure A.1: $\langle|\Delta_i|\rangle$ as a function of $k_BT$, for the AAH model with system size $N = 100$ at $J = 0$ (See section 4.1). The tolerance for the relative residual error is $\delta\Delta = 10^{-6}$.

# Appendix B

# Inversion of the equation of motion for the anomalous Green's function

In order to do the inversion in (2.21), let us consider the following system of matrix equations:

$$\sum_i A_{mi} F_{in} = D_{mn} \tag{B.1}$$

$$\sum_i A_{mi} G_{in} = \delta_{m,n}, \tag{B.2}$$

where $A$, $F$, $D$ and $G$ are general square matrices. A solution for $F$ is given by

$$F_{in} = \sum_l G_{il} D_{ln}. \tag{B.3}$$

This is easy to check,

$$\begin{aligned}
\sum_i A_{mi} F_{in} &= \sum_i A_{mi} \sum_l G_{il} D_{ln} \\
&= \sum_l \left[ \sum_i A_{mi} G_{il} \right] D_{ln} \\
&= \sum_l \delta_{m,l} D_{ln} \\
&= D_{mn},
\end{aligned}$$

as intended.

If we interpret the anomalous Green's function equation of motion (2.21) as equation (B.1) and the equation of motion of the noninteracting Green's function (2.12) as equation (B.2), then the inversion for $\mathcal{F}$ follows easily in analogy with equation (B.3).

# Appendix C

# Linear gap equation details for SLG

This appendix is devoted to computing the coefficients $\Gamma_{i,j}^{m,n}(\mathbf{k})$ defined in Eq. (3.26). In order to simplify the final results, it is useful to define the auxiliar functions given by

$$\begin{aligned}\chi^{\pm}(\mathbf{k};\mu,\beta_c) &\equiv \frac{tanh\left(\frac{\beta_c[\varepsilon(\mathbf{k})-\mu]}{2}\right)}{2[\varepsilon(\mathbf{k})-\mu]} + \frac{tanh\left(\frac{\beta_c[\varepsilon(\mathbf{k})+\mu]}{2}\right)}{2[\varepsilon(\mathbf{k})+\mu]} \pm l(\mathbf{k};\mu,\beta_c)\\ \zeta(\mathbf{k};\mu,\beta_c) &\equiv \frac{tanh\left(\frac{\beta_c[\varepsilon(\mathbf{k})-\mu]}{2}\right)}{2[\varepsilon(\mathbf{k})-\mu]} - \frac{tanh\left(\frac{\beta_c[\varepsilon(\mathbf{k})+\mu]}{2}\right)}{2[\varepsilon(\mathbf{k})+\mu]},\end{aligned} \tag{C.1}$$

where

$$l(\mathbf{k};\mu,\beta_c) \equiv \chi(\varepsilon_+(\mathbf{k}),\varepsilon_-(\mathbf{k})) + \chi(\varepsilon_-(\mathbf{k}),\varepsilon_+(\mathbf{k})) = \begin{cases} -\frac{\beta_c}{1+cosh(\beta_c\varepsilon(\mathbf{k}))} & ,\mu = 0 \\ \frac{1}{2\mu}\left[tanh\left(\frac{\beta_c[\varepsilon(\mathbf{k})-\mu]}{2}\right) - tanh\left(\frac{\beta_c[\varepsilon(\mathbf{k})+\mu]}{2}\right)\right] & ,\mu \neq 0, \end{cases} \tag{C.2}$$

is a function that retains information about inter-band interactions, in contrast with the $\frac{tanh\left(\frac{\beta_c[\varepsilon(\mathbf{k})\pm\mu]}{2}\right)}{2[\varepsilon(\mathbf{k})\pm\mu]}$ terms that pertain to the intra-band coupling.

In order to explicitly do the double sum over band indices, we have to project the eigenvectors (3.16) of the Bloch Hamiltonian onto the sublattice basis,

$$\begin{aligned}u_A^+(\mathbf{k}) &= \frac{e^{i\phi(\mathbf{k})/2}}{\sqrt{2}}, u_B^+(\mathbf{k}) = \frac{e^{-i\phi(\mathbf{k})/2}}{\sqrt{2}}\\ u_A^-(\mathbf{k}) &= \frac{e^{i\phi(\mathbf{k})/2}}{\sqrt{2}}, u_B^-(\mathbf{k}) = -\frac{e^{-i\phi(\mathbf{k})/2}}{\sqrt{2}},\end{aligned} \tag{C.3}$$

and use the fact that for the $\chi\left(\varepsilon_{\lambda}\left(\mathbf{k}\right),\varepsilon_{\lambda'}\left(\mathbf{k}\right)\right)$ function we have that

$$\begin{aligned}
\chi\left(\varepsilon_{+}\left(\mathbf{k}\right),\varepsilon_{+}\left(\mathbf{k}\right)\right) &= -\frac{tanh\left(\frac{\beta_{c}\left[\varepsilon\left(\mathbf{k}\right)-\mu\right]}{2}\right)}{2\left[\varepsilon\left(\mathbf{k}\right)-\mu\right]} \\
\chi\left(\varepsilon_{-}\left(\mathbf{k}\right),\varepsilon_{-}\left(\mathbf{k}\right)\right) &= -\frac{tanh\left(\frac{\beta_{c}\left[\varepsilon\left(\mathbf{k}\right)+\mu\right]}{2}\right)}{2\left[\varepsilon\left(\mathbf{k}\right)+\mu\right]} \\
\chi\left(\varepsilon_{+}\left(\mathbf{k}\right),\varepsilon_{-}\left(\mathbf{k}\right)\right)+\chi\left(\varepsilon_{-}\left(\mathbf{k}\right),\varepsilon_{+}\left(\mathbf{k}\right)\right) &= l\left(\mathbf{k};\mu,\beta_{c}\right) \\
\chi\left(\varepsilon_{+}\left(\mathbf{k}\right),\varepsilon_{-}\left(\mathbf{k}\right)\right)-\chi\left(\varepsilon_{-}\left(\mathbf{k}\right),\varepsilon_{+}\left(\mathbf{k}\right)\right) &= 0,
\end{aligned} \tag{C.4}$$

which follows trivially from the Matsubara summation results in Eqs. (3.28), (3.30), (3.31) and (3.29).

Therefore, the explict form of the coefficients $\Gamma_{i,j}^{m,n}\left(\mathbf{k}\right)$ is

$$\begin{aligned}
\Gamma_{A,A}^{A,A}\left(\mathbf{k}\right) &= \sum_{\lambda,\lambda'}\chi\left(\varepsilon_{\lambda}\left(\mathbf{k}\right),\varepsilon_{\lambda'}\left(\mathbf{k}\right)\right)u_{A}^{\lambda}\left(\mathbf{k}\right)u_{A}^{\lambda,*}\left(\mathbf{k}\right)u_{A}^{\lambda'}\left(-\mathbf{k}\right)u_{A}^{\lambda',*}\left(-\mathbf{k}\right) \\
&= \frac{1}{4}\left[\chi\left(\varepsilon_{+}\left(\mathbf{k}\right),\varepsilon_{+}\left(\mathbf{k}\right)\right)+\chi\left(\varepsilon_{+}\left(\mathbf{k}\right),\varepsilon_{-}\left(\mathbf{k}\right)\right)+\chi\left(\varepsilon_{-}\left(\mathbf{k}\right),\varepsilon_{+}\left(\mathbf{k}\right)\right)+\chi\left(\varepsilon_{-}\left(\mathbf{k}\right),\varepsilon_{-}\left(\mathbf{k}\right)\right)\right] \\
&= -\frac{1}{4}\left[\frac{tanh\left(\frac{\beta_{c}\left[\varepsilon\left(\mathbf{k}\right)-\mu\right]}{2}\right)}{2\left[\varepsilon\left(\mathbf{k}\right)-\mu\right]}+\frac{tanh\left(\frac{\beta_{c}\left[\varepsilon\left(\mathbf{k}\right)+\mu\right]}{2}\right)}{2\left[\varepsilon\left(\mathbf{k}\right)+\mu\right]}-l\left(\mathbf{k};\mu,\beta_{c}\right)\right] \\
&= -\frac{1}{4}\chi^{-}\left(\mathbf{k};\mu,\beta_{c}\right),
\end{aligned}$$

$$\begin{aligned}
\Gamma_{A,A}^{A,B}\left(\mathbf{k}\right) &= \sum_{\lambda,\lambda'}\chi\left(\varepsilon_{n}\left(\mathbf{k}\right),\varepsilon_{n'}\left(\mathbf{k}\right)\right)u_{A}^{\lambda}\left(\mathbf{k}\right)u_{A}^{\lambda,*}\left(\mathbf{k}\right)u_{A}^{\lambda'}\left(-\mathbf{k}\right)u_{B}^{\lambda',*}\left(-\mathbf{k}\right) \\
&= \frac{1}{4}\left[\chi\left(\varepsilon_{+}\left(\mathbf{k}\right),\varepsilon_{+}\left(\mathbf{k}\right)\right)-\chi\left(\varepsilon_{+}\left(\mathbf{k}\right),\varepsilon_{-}\left(\mathbf{k}\right)\right)+\chi\left(\varepsilon_{-}\left(\mathbf{k}\right),\varepsilon_{+}\left(\mathbf{k}\right)\right)-\chi\left(\varepsilon_{-}\left(\mathbf{k}\right),\varepsilon_{-}\left(\mathbf{k}\right)\right)\right]e^{i\phi\left(-\mathbf{k}\right)} \\
&= -\frac{1}{4}\left[\frac{tanh\left(\frac{\beta_{c}\left[\varepsilon\left(\mathbf{k}\right)-\mu\right]}{2}\right)}{2\left[\varepsilon\left(\mathbf{k}\right)-\mu\right]}-\frac{tanh\left(\frac{\beta_{c}\left[\varepsilon\left(\mathbf{k}\right)+\mu\right]}{2}\right)}{2\left[\varepsilon\left(\mathbf{k}\right)+\mu\right]}\right]e^{i\phi\left(-\mathbf{k}\right)} \\
&= -\frac{1}{4}\zeta\left(\mathbf{k};\mu,\beta_{c}\right)e^{i\phi\left(-\mathbf{k}\right)},
\end{aligned}$$

$$\begin{aligned}
\Gamma_{A,A}^{B,A}\left(\mathbf{k}\right) &= \sum_{\lambda,\lambda'}\chi\left(\varepsilon_{n}\left(\mathbf{k}\right),\varepsilon_{n'}\left(\mathbf{k}\right)\right)u_{A}^{\lambda}\left(\mathbf{k}\right)u_{B}^{\lambda,*}\left(\mathbf{k}\right)u_{A}^{\lambda'}\left(-\mathbf{k}\right)u_{A}^{\lambda',*}\left(-\mathbf{k}\right) \\
&= \frac{1}{4}\left[\chi\left(\varepsilon_{+}\left(\mathbf{k}\right),\varepsilon_{+}\left(\mathbf{k}\right)\right)+\chi\left(\varepsilon_{+}\left(\mathbf{k}\right),\varepsilon_{-}\left(\mathbf{k}\right)\right)-\chi\left(\varepsilon_{-}\left(\mathbf{k}\right),\varepsilon_{+}\left(\mathbf{k}\right)\right)-\chi\left(\varepsilon_{-}\left(\mathbf{k}\right),\varepsilon_{-}\left(\mathbf{k}\right)\right)\right]e^{i\phi\left(\mathbf{k}\right)} \\
&= -\frac{1}{4}\left[\frac{tanh\left(\frac{\beta_{c}\left[\varepsilon\left(\mathbf{k}\right)-\mu\right]}{2}\right)}{2\left[\varepsilon\left(\mathbf{k}\right)-\mu\right]}-\frac{tanh\left(\frac{\beta_{c}\left[\varepsilon\left(\mathbf{k}\right)+\mu\right]}{2}\right)}{2\left[\varepsilon\left(\mathbf{k}\right)+\mu\right]}\right]e^{i\phi\left(\mathbf{k}\right)} \\
&= -\frac{1}{4}\zeta\left(\mathbf{k};\mu,\beta_{c}\right)e^{i\phi\left(\mathbf{k}\right)},
\end{aligned}$$

$$\begin{aligned}
\Gamma_{A,A}^{B,B}(\mathbf{k}) &= \sum_{\lambda,\lambda'} \chi\left(\varepsilon_n(\mathbf{k}), \varepsilon_{n'}(\mathbf{k})\right) u_A^{\lambda}(\mathbf{k}) u_B^{\lambda,*}(\mathbf{k}) u_A^{\lambda'}(-\mathbf{k}) u_B^{\lambda',*}(-\mathbf{k}) \\
&= \frac{1}{4}\left[\chi\left(\varepsilon_+(\mathbf{k}), \varepsilon_+(\mathbf{k})\right) - \chi\left(\varepsilon_+(\mathbf{k}), \varepsilon_-(\mathbf{k})\right) - \chi\left(\varepsilon_-(\mathbf{k}), \varepsilon_+(\mathbf{k})\right) + \chi\left(\varepsilon_-(\mathbf{k}), \varepsilon_-(\mathbf{k})\right)\right] e^{i(\phi(\mathbf{k})+\phi(-\mathbf{k}))} \\
&= -\frac{1}{4}\left[\frac{tanh\left(\frac{\beta_c[\varepsilon(\mathbf{k})-\mu]}{2}\right)}{2[\varepsilon(\mathbf{k})-\mu]} + \frac{tanh\left(\frac{\beta_c[\varepsilon(\mathbf{k})+\mu]}{2}\right)}{2[\varepsilon(\mathbf{k})+\mu]} + l(\mathbf{k};\mu,\beta_c)\right] e^{i(\phi(\mathbf{k})+\phi(-\mathbf{k}))} \\
&= -\frac{1}{4}\chi^{+}(\mathbf{k};\mu,\beta_c)\, e^{i(\phi(\mathbf{k})+\phi(-\mathbf{k}))}
\end{aligned}$$

$$\begin{aligned}
\Gamma_{A,B}^{A,A}(\mathbf{k}) &= \sum_{\lambda,\lambda'} \chi\left(\varepsilon_n(\mathbf{k}), \varepsilon_{n'}(\mathbf{k})\right) u_A^{\lambda}(\mathbf{k}) u_A^{\lambda,*}(\mathbf{k}) u_B^{\lambda'}(-\mathbf{k}) u_A^{\lambda',*}(-\mathbf{k}) \\
&= \frac{1}{4}\left[\chi\left(\varepsilon_+(\mathbf{k}), \varepsilon_+(\mathbf{k})\right) - \chi\left(\varepsilon_+(\mathbf{k}), \varepsilon_-(\mathbf{k})\right) + \chi\left(\varepsilon_-(\mathbf{k}), \varepsilon_+(\mathbf{k})\right) - \chi\left(\varepsilon_-(\mathbf{k}), \varepsilon_-(\mathbf{k})\right)\right] e^{-i\phi(-\mathbf{k})} \\
&= -\frac{1}{4}\left[\frac{tanh\left(\frac{\beta_c[\varepsilon(\mathbf{k})-\mu]}{2}\right)}{2[\varepsilon(\mathbf{k})-\mu]} - \frac{tanh\left(\frac{\beta[\varepsilon(\mathbf{k})+\mu]}{2}\right)}{2[\varepsilon(\mathbf{k})+\mu]}\right] e^{-i\phi(-\mathbf{k})} \\
&= -\frac{1}{4}\zeta(\mathbf{k};\mu,\beta_c)\, e^{-i\phi(-\mathbf{k})},
\end{aligned}$$

$$\begin{aligned}
\Gamma_{A,B}^{A,B}(\mathbf{k}) &= \sum_{\lambda,\lambda'} \chi\left(\varepsilon_n(\mathbf{k}), \varepsilon_{n'}(\mathbf{k})\right) u_A^{\lambda}(\mathbf{k}) u_A^{\lambda,*}(\mathbf{k}) u_B^{\lambda'}(-\mathbf{k}) u_B^{\lambda',*}(-\mathbf{k}) \\
&= \frac{1}{4}\left[\chi\left(\varepsilon_+(\mathbf{k}), \varepsilon_+(\mathbf{k})\right) + \chi\left(\varepsilon_+(\mathbf{k}), \varepsilon_-(\mathbf{k})\right) + \chi\left(\varepsilon_-(\mathbf{k}), \varepsilon_+(\mathbf{k})\right) + \chi\left(\varepsilon_-(\mathbf{k}), \varepsilon_-(\mathbf{k})\right)\right] \\
&= -\frac{1}{4}\left[\frac{tanh\left(\frac{\beta_c[\varepsilon(\mathbf{k})-\mu]}{2}\right)}{2[\varepsilon(\mathbf{k})-\mu]} + \frac{tanh\left(\frac{\beta_c[\varepsilon(\mathbf{k})+\mu]}{2}\right)}{2[\varepsilon(\mathbf{k})+\mu]} - l(\mathbf{k};\mu,\beta_c)\right] \\
&= -\frac{1}{4}\chi^{-}(\mathbf{k};\mu,\beta_c)
\end{aligned}$$

$$\begin{aligned}
\Gamma_{A,B}^{B,A}(\mathbf{k}) &= \sum_{\lambda,\lambda'} \chi\left(\varepsilon_n(\mathbf{k}), \varepsilon_{n'}(\mathbf{k})\right) u_A^{\lambda}(\mathbf{k}) u_B^{\lambda,*}(\mathbf{k}) u_B^{\lambda'}(-\mathbf{k}) u_A^{\lambda',*}(-\mathbf{k}) \\
&= \frac{1}{4}\left[\chi\left(\varepsilon_+(\mathbf{k}), \varepsilon_+(\mathbf{k})\right) - \chi\left(\varepsilon_+(\mathbf{k}), \varepsilon_-(\mathbf{k})\right) - \chi\left(\varepsilon_-(\mathbf{k}), \varepsilon_+(\mathbf{k})\right) + \chi\left(\varepsilon_-(\mathbf{k}), \varepsilon_-(\mathbf{k})\right)\right] e^{i(\phi(\mathbf{k})-\phi(-\mathbf{k}))} \\
&= -\frac{1}{4}\left[\frac{tanh\left(\frac{\beta_c[\varepsilon(\mathbf{k})-\mu]}{2}\right)}{2[\varepsilon(\mathbf{k})-\mu]} + \frac{tanh\left(\frac{\beta_c[\varepsilon(\mathbf{k})+\mu]}{2}\right)}{2[\varepsilon(\mathbf{k})+\mu]} + l(\mathbf{k};\mu,\beta_c)\right] e^{i(\phi(\mathbf{k})-\phi(-\mathbf{k}))} \\
&= -\frac{1}{4}\chi^{+}(\mathbf{k};\mu,\beta_c)\, e^{i(\phi(\mathbf{k})-\phi(-\mathbf{k}))},
\end{aligned}$$

$$\begin{aligned}
\Gamma_{A,B}^{B,B}(\mathbf{k}) &= \sum_{\lambda,\lambda'} \chi\left(\varepsilon_n(\mathbf{k}), \varepsilon_{n'}(\mathbf{k})\right) u_A^{\lambda}(\mathbf{k}) u_B^{\lambda,*}(\mathbf{k}) u_B^{\lambda'}(-\mathbf{k}) u_B^{\lambda',*}(-\mathbf{k}) \\
&= \frac{1}{4}\left[\chi\left(\varepsilon_+(\mathbf{k}), \varepsilon_+(\mathbf{k})\right) + \chi\left(\varepsilon_+(\mathbf{k}), \varepsilon_-(\mathbf{k})\right) - \chi\left(\varepsilon_-(\mathbf{k}), \varepsilon_+(\mathbf{k})\right) - \chi\left(\varepsilon_-(\mathbf{k}), \varepsilon_-(\mathbf{k})\right)\right] e^{i\phi(\mathbf{k})} \\
&= -\frac{1}{4}\left[\frac{tanh\left(\frac{\beta_c[\varepsilon(\mathbf{k})-\mu]}{2}\right)}{2[\varepsilon(\mathbf{k})-\mu]} - \frac{tanh\left(\frac{\beta_c[\varepsilon(\mathbf{k})+\mu]}{2}\right)}{2[\varepsilon(\mathbf{k})+\mu]}\right] e^{i\phi(\mathbf{k})} \\
&= -\frac{1}{4}\zeta(\mathbf{k};\mu,\beta_c)\, e^{i\phi(\mathbf{k})},
\end{aligned}$$

$$\begin{aligned}
\Gamma_{B,A}^{A,A}(\mathbf{k}) &= \sum_{\lambda,\lambda'} \chi\left(\varepsilon_n(\mathbf{k}), \varepsilon_{n'}(\mathbf{k})\right) u_B^{\lambda}(\mathbf{k}) u_A^{\lambda,*}(\mathbf{k}) u_A^{\lambda'}(-\mathbf{k}) u_A^{\lambda',*}(-\mathbf{k}) \\
&= \frac{1}{4}\left[\chi\left(\varepsilon_+(\mathbf{k}), \varepsilon_+(\mathbf{k})\right) + \chi\left(\varepsilon_+(\mathbf{k}), \varepsilon_-(\mathbf{k})\right) - \chi\left(\varepsilon_-(\mathbf{k}), \varepsilon_+(\mathbf{k})\right) - \chi\left(\varepsilon_-(\mathbf{k}), \varepsilon_-(\mathbf{k})\right)\right] e^{-i\phi(\mathbf{k})} \\
&= -\frac{1}{4}\left[\frac{tanh\left(\frac{\beta_c[\varepsilon(\mathbf{k})-\mu]}{2}\right)}{2[\varepsilon(\mathbf{k})-\mu]} - \frac{tanh\left(\frac{\beta_c[\varepsilon(\mathbf{k})+\mu]}{2}\right)}{2[\varepsilon(\mathbf{k})+\mu]}\right] e^{-i\phi(\mathbf{k})} \\
&= -\frac{1}{4}\zeta(\mathbf{k};\mu,\beta_c)\, e^{-i\phi(\mathbf{k})}
\end{aligned}$$

$$\begin{aligned}
\Gamma_{B,A}^{A,B}(\mathbf{k}) &= \sum_{\lambda,\lambda'} \chi\left(\varepsilon_n(\mathbf{k}), \varepsilon_{n'}(\mathbf{k})\right) u_B^{\lambda}(\mathbf{k}) u_A^{\lambda,*}(\mathbf{k}) u_A^{\lambda'}(-\mathbf{k}) u_B^{\lambda',*}(-\mathbf{k}) \\
&= \frac{1}{4}\left[\chi\left(\varepsilon_+(\mathbf{k}), \varepsilon_+(\mathbf{k})\right) - \chi\left(\varepsilon_+(\mathbf{k}), \varepsilon_-(\mathbf{k})\right) - \chi\left(\varepsilon_-(\mathbf{k}), \varepsilon_+(\mathbf{k})\right) + \chi\left(\varepsilon_-(\mathbf{k}), \varepsilon_-(\mathbf{k})\right)\right] e^{-i(\phi(\mathbf{k})-\phi(-\mathbf{k}))} \\
&= -\frac{1}{4}\left[\frac{tanh\left(\frac{\beta_c[\varepsilon(\mathbf{k})-\mu]}{2}\right)}{2[\varepsilon(\mathbf{k})-\mu]} + \frac{tanh\left(\frac{\beta_c[\varepsilon(\mathbf{k})+\mu]}{2}\right)}{2[\varepsilon(\mathbf{k})+\mu]} + l(\mathbf{k};\mu,\beta_c)\right] e^{-i(\phi(\mathbf{k})-\phi(-\mathbf{k}))} \\
&= -\frac{1}{4}\chi^{+}(\mathbf{k};\mu,\beta_c)\, e^{-i(\phi(\mathbf{k})-\phi(-\mathbf{k}))},
\end{aligned}$$

$$\begin{aligned}
\Gamma_{B,A}^{B,A}(\mathbf{k}) &= \sum_{\lambda,\lambda'} \chi\left(\varepsilon_n(\mathbf{k}), \varepsilon_{n'}(\mathbf{k})\right) u_B^{\lambda}(\mathbf{k}) u_B^{\lambda,*}(\mathbf{k}) u_A^{\lambda'}(-\mathbf{k}) u_A^{\lambda',*}(-\mathbf{k}) \\
&= \frac{1}{4}\left[\chi\left(\varepsilon_+(\mathbf{k}), \varepsilon_+(\mathbf{k})\right) + \chi\left(\varepsilon_+(\mathbf{k}), \varepsilon_-(\mathbf{k})\right) + \chi\left(\varepsilon_-(\mathbf{k}), \varepsilon_+(v)\right) + \chi\left(\varepsilon_-(\mathbf{k}), \varepsilon_-(\mathbf{k})\right)\right] \\
&= -\frac{1}{4}\left[\frac{tanh\left(\frac{\beta_c[\varepsilon(\mathbf{k})-\mu]}{2}\right)}{2[\varepsilon(\mathbf{k})-\mu]} + \frac{tanh\left(\frac{\beta_c[\varepsilon(\mathbf{k})+\mu]}{2}\right)}{2[\varepsilon(\mathbf{k})+\mu]} - l(\mathbf{k};\mu,\beta_c)\right] \\
&= -\frac{1}{4}\chi^{-}(\mathbf{k};\mu,\beta_c),
\end{aligned}$$

$$\begin{aligned}
\Gamma_{B,A}^{B,B}(\mathbf{k}) &= \sum_{\lambda,\lambda'} \chi\left(\varepsilon_n(\mathbf{k}), \varepsilon_{n'}(\mathbf{k})\right) u_B^{\lambda}(\mathbf{k}) u_B^{\lambda,*}(\mathbf{k}) u_A^{\lambda'}(-\mathbf{k}) u_B^{\lambda',*}(-\mathbf{k}) \\
&= \frac{1}{4}\left[\chi\left(\varepsilon_+(\mathbf{k}), \varepsilon_+(\mathbf{k})\right) - \chi\left(\varepsilon_+(\mathbf{k}), \varepsilon_-(\mathbf{k})\right) + \chi\left(\varepsilon_-(\mathbf{k}), \varepsilon_+(\mathbf{k})\right) - \chi\left(\varepsilon_-(\mathbf{k}), \varepsilon_-(\mathbf{k})\right)\right] e^{i\phi(-\mathbf{k})} \\
&= -\frac{1}{4}\left[\frac{tanh\left(\frac{\beta_c[\varepsilon(\mathbf{k})-\mu]}{2}\right)}{2[\varepsilon(\mathbf{k})-\mu]} - \frac{tanh\left(\frac{\beta[\varepsilon(\mathbf{k})+\mu]}{2}\right)}{2[\varepsilon(\mathbf{k})+\mu]}\right] e^{i\phi(-\mathbf{k})} \\
&= -\frac{1}{4}\zeta(\mathbf{k};\mu,\beta_c)\, e^{i\phi(-\mathbf{k})},
\end{aligned}$$

$$\begin{aligned}
\Gamma_{B,B}^{A,A}(\mathbf{k}) &= \sum_{\lambda,\lambda'} \chi\left(\varepsilon_n(\mathbf{k}), \varepsilon_{n'}(\mathbf{k})\right) u_B^{\lambda}(\mathbf{k}) u_A^{\lambda,*}(\mathbf{k}) u_B^{\lambda'}(-\mathbf{k}) u_A^{\lambda',*}(-\mathbf{k}) \\
&= \frac{1}{4}\left[\chi\left(\varepsilon_+(\mathbf{k}), \varepsilon_+(\mathbf{k})\right) - \chi\left(\varepsilon_+(\mathbf{k}), \varepsilon_-(\mathbf{k})\right) - \chi\left(\varepsilon_-(\mathbf{k}), \varepsilon_+(\mathbf{k})\right) + \chi\left(\varepsilon_-(\mathbf{k}), \varepsilon_-(\mathbf{k})\right)\right] e^{-i(\phi(\mathbf{k})+\phi(-\mathbf{k}))} \\
&= -\frac{1}{4}\left[\frac{tanh\left(\frac{\beta_c[\varepsilon(\mathbf{k})-\mu]}{2}\right)}{2[\varepsilon(\mathbf{k})-\mu]} + \frac{tanh\left(\frac{\beta_c[\varepsilon(\mathbf{k})+\mu]}{2}\right)}{2[\varepsilon(\mathbf{k})+\mu]} + l(\mathbf{k};\mu,\beta_c)\right] e^{-i(\phi(\mathbf{k})+\phi(-\mathbf{k}))} \\
&= -\frac{1}{4}\chi^{+}(\mathbf{k};\mu,\beta_c)\, e^{-i(\phi(\mathbf{k})+\phi(-\mathbf{k}))},
\end{aligned}$$

$$\begin{aligned}
\Gamma_{B,B}^{A,B}(\mathbf{k}) &= \sum_{\lambda,\lambda'} \chi\left(\varepsilon_n(\mathbf{k}), \varepsilon_{n'}(\mathbf{k})\right) u_B^{\lambda}(\mathbf{k}) u_A^{\lambda,*}(\mathbf{k}) u_B^{\lambda'}(-\mathbf{k}) u_B^{\lambda',*}(-\mathbf{k}) \\
&= \frac{1}{4}\left[\chi\left(\varepsilon_+(\mathbf{k}), \varepsilon_+(\mathbf{k})\right) + \chi\left(\varepsilon_+(\mathbf{k}), \varepsilon_-(\mathbf{k})\right) - \chi\left(\varepsilon_-(\mathbf{k}), \varepsilon_+(v)\right) - \chi\left(\varepsilon_-(\mathbf{k}), \varepsilon_-(\mathbf{k})\right)\right] e^{-i\phi(\mathbf{k})} \\
&= -\frac{1}{4}\left[\frac{tanh\left(\frac{\beta_c[\varepsilon(\mathbf{k})-\mu]}{2}\right)}{2[\varepsilon(\mathbf{k})-\mu]} - \frac{tanh\left(\frac{\beta_c[\varepsilon(\mathbf{k})+\mu]}{2}\right)}{2[\varepsilon(\mathbf{k})+\mu]}\right] e^{-i\phi(\mathbf{k})} \\
&= -\frac{1}{4}\zeta(\mathbf{k};\mu,\beta_c)\, e^{-i\phi(\mathbf{k})},
\end{aligned}$$

$$\begin{aligned}
\Gamma_{B,B}^{B,A}(\mathbf{k}) &= \sum_{\lambda,\lambda'} \chi\left(\varepsilon_n(\mathbf{k}), \varepsilon_{n'}(\mathbf{k})\right) u_B^{\lambda}(\mathbf{k}) u_B^{\lambda,*}(\mathbf{k}) u_B^{\lambda'}(-\mathbf{k}) u_A^{\lambda',*}(-\mathbf{k}) \\
&= \frac{1}{4}\left[\chi\left(\varepsilon_+(\mathbf{k}), \varepsilon_+(\mathbf{k})\right) - \chi\left(\varepsilon_+(\mathbf{k}), \varepsilon_-(\mathbf{k})\right) + \chi\left(\varepsilon_-(\mathbf{k}), \varepsilon_+(\mathbf{k})\right) - \chi\left(\varepsilon_-(\mathbf{k}), \varepsilon_-(\mathbf{k})\right)\right] e^{-i\phi(-\mathbf{k})} \\
&= -\frac{1}{4}\left[\frac{tanh\left(\frac{\beta_c[\varepsilon(\mathbf{k})-\mu]}{2}\right)}{2[\varepsilon(\mathbf{k})-\mu]} - \frac{tanh\left(\frac{\beta_c[\varepsilon(\mathbf{k})+\mu]}{2}\right)}{2[\varepsilon(\mathbf{k})+\mu]}\right] e^{-i\phi(-\mathbf{k})} \\
&= -\frac{1}{4}\zeta(\mathbf{k};\mu,\beta_c)\, e^{-i\phi(-\mathbf{k})},
\end{aligned}$$

$$
\begin{aligned}
\Gamma_{B,B}^{B,B}(\mathbf{k}) &= \sum_{\lambda,\lambda'} \chi\left(\varepsilon_n(\mathbf{k}), \varepsilon_{n'}(\mathbf{k})\right) u_B^{\lambda}(\mathbf{k}) u_B^{\lambda,*}(\mathbf{k}) u_B^{\lambda'}(-\mathbf{k}) u_B^{\lambda',*}(-\mathbf{k}) \\
&= \frac{1}{4}\left[\chi\left(\varepsilon_+(\mathbf{k}), \varepsilon_+(\mathbf{k})\right) + \chi\left(\varepsilon_+(\mathbf{k}), \varepsilon_-(\mathbf{k})\right) + \chi\left(\varepsilon_-(\mathbf{k}), \varepsilon_+(\mathbf{k})\right) + \chi\left(\varepsilon_-(\mathbf{k}), \varepsilon_-(\mathbf{k})\right)\right] \\
&= -\frac{1}{4}\left[\frac{tanh\left(\frac{\beta_c[\varepsilon(\mathbf{k})-\mu]}{2}\right)}{2[\varepsilon(\mathbf{k})-\mu]} + \frac{tanh\left(\frac{\beta[\varepsilon(\mathbf{k})+\mu]}{2}\right)}{2[\varepsilon(\mathbf{k})+\mu]} - l(\mathbf{k};\mu,\beta_c)\right] \\
&= -\frac{1}{4}\chi^{-}(\mathbf{k};\mu,\beta_c).
\end{aligned}
$$

# Bibliography


[1] Walther Meissner and Robert Ochsenfeld. Ein neuer effekt bei eintritt der supraleitfähigkeit. *Naturwissenschaften*, 21(44):787–788, 1933.

[2] J. Bardeen, L. N. Cooper, and J. R. Schrieffer. Theory of superconductivity. *Phys. Rev.*, 108:1175–1204, Dec 1957.

[3] J George Bednorz and K Alex Müller. Possible high Tc superconductivity in the Ba- La- Cu- O system. *Zeitschrift für Physik B Condensed Matter*, 64(2):189–193, 1986.

[4] Yuan Cao, Valla Fatemi, Shiang Fang, Kenji Watanabe, Takashi Taniguchi, Efthimios Kaxiras, and Pablo Jarillo-Herrero. Unconventional superconductivity in magic-angle graphene superlattices. *Nature*, 556(7699):43–50, 2018.

[5] J. M. B. Lopes dos Santos, N. M. R. Peres, and A. H. Castro Neto. Graphene bilayer with a twist: Electronic structure. *Phys. Rev. Lett.*, 99:256802, Dec 2007.

[6] Rafi Bistritzer and A. Macdonald. Moire bands in twisted double-layer graphene. *Proceedings of the National Academy of Sciences of the United States of America*, 108, 09 2010.

[7] S. Shallcross, S. Sharma, E. Kandelaki, and O. A. Pankratov. Electronic structure of turbostratic graphene. *Phys. Rev. B*, 81:165105, Apr 2010.

[8] E. Suárez Morell, J. D. Correa, P. Vargas, M. Pacheco, and Z. Barticevic. Flat bands in slightly twisted bilayer graphene: Tight-binding calculations. *Phys. Rev. B*, 82:121407, Sep 2010.

[9] J. M. B. Lopes dos Santos, N. M. R. Peres, and A. H. Castro Neto. Continuum model of the twisted graphene bilayer. *Phys. Rev. B*, 86:155449, Oct 2012.

[10] Yuan Cao, Valla Fatemi, Ahmet Demir, Shiang Fang, Spencer L. Tomarken, Jason Y. Luo, Javier D. Sanchez-Yamagishi, Kenji Watanabe, Takashi Taniguchi, Efthimios Kaxiras, Ray C. Ashoori, and Pablo Jarillo-Herrero. Correlated insulator behaviour at half-filling in magic-angle graphene superlattices. *Nature*, 556(7699):80–84, 2018.

[11] Teemu J. Peltonen, Risto Ojajärvi, and Tero T. Heikkilä. Mean-field theory for superconductivity in twisted bilayer graphene. *Phys. Rev. B*, 98:220504, Dec 2018.

[12] Hoi Chun Po, Liujun Zou, Ashvin Vishwanath, and T. Senthil. Origin of mott insulating behavior and superconductivity in twisted bilayer graphene. *Phys. Rev. X*, 8:031089, Sep 2018.

[13] Cenke Xu and Leon Balents. Topological superconductivity in twisted multilayer graphene. *Phys. Rev. Lett.*, 121:087001, Aug 2018.

[14] Hiroki Isobe, Noah F. Q. Yuan, and Liang Fu. Unconventional superconductivity and density waves in twisted bilayer graphene. *Phys. Rev. X*, 8:041041, Dec 2018.

[15] Dante M. Kennes, Johannes Lischner, and Christoph Karrasch. Strong correlations and $d+id$ superconductivity in twisted bilayer graphene. *Phys. Rev. B*, 98:241407, Dec 2018.

[16] Cheng-Cheng Liu, Li-Da Zhang, Wei-Qiang Chen, and Fan Yang. Chiral spin density wave and $d+id$ superconductivity in the magic-angle-twisted bilayer graphene. *Phys. Rev. Lett.*, 121:217001, Nov 2018.

[17] Tommaso Cea and Francisco Guinea. Coulomb interaction, phonons, and superconductivity in twisted bilayer graphene. *Proceedings of the National Academy of Sciences*, 118:e2107874118, 08 2021.

[18] Sujay Ray, Jeil Jung, and Tanmoy Das. Wannier pairs in superconducting twisted bilayer graphene and related systems. *Phys. Rev. B*, 99:134515, Apr 2019.

[19] Grigory Tarnopolsky, Alex Jura Kruchkov, and Ashvin Vishwanath. Origin of magic angles in twisted bilayer graphene. *Phys. Rev. Lett.*, 122:106405, Mar 2019.

[20] Miguel Gonçalves, Hadi Z Olyaei, Bruno Amorim, Rubem Mondaini, Pedro Ribeiro, and Eduardo V Castro. Incommensurability-induced sub-ballistic narrow-band-states in twisted bilayer graphene. *2D Materials*, 9(1):011001, 2021.

[21] Yixing Fu, Elio J König, Justin H Wilson, Yang-Zhi Chou, and Jedediah H Pixley. Magic-angle semimetals. *npj Quantum Materials*, 5(1):1–8, 2020.

[22] Zhijie Fan, Gia-Wei Chern, and Shi-Zeng Lin. Enhanced superconductivity in quasiperiodic crystals. *Phys. Rev. Research*, 3:023195, Jun 2021.

[23] P. W. Anderson. Absence of diffusion in certain random lattices. *Phys. Rev.*, 109:1492–1505, Mar 1958.

[24] P G Harper. Single band motion of conduction electrons in a uniform magnetic field. *Proceedings of the Physical Society. Section A*, 68(10):874–878, oct 1955.

[25] Serge Aubry and Gilles André. Analyticity breaking and anderson localization in incommensurate lattices. *Ann. Israel Phys. Soc*, 3(133):18, 1980.

[26] Douglas R. Hofstadter. Energy levels and wave functions of bloch electrons in rational and irrational magnetic fields. *Phys. Rev. B*, 14:2239–2249, Sep 1976.

[27] Mahito Kohmoto and Jayanth R. Banavar. Quasiperiodic lattice: Electronic properties, phonon properties, and diffusion. *Phys. Rev. B*, 34:563–566, Jul 1986.

[28] Ya. G. Sinai. Anderson localization for one-dimensional difference Schrödinger operator with quasiperiodic potential. *Journal of Statistical Physics*, 46(5-6):861–909, March 1987.

[29] V. A. Chulaevsky and Ya. G. Sinai. Anderson localization for the 1- D discrete Schrödinger operator with two-frequency potential. *Communications in Mathematical Physics*, 125(1):91–112, March 1989.

[30] Attila Szabó and Ulrich Schneider. Mixed spectra and partially extended states in a two-dimensional quasiperiodic model. *Phys. Rev. B*, 101:014205, Jan 2020.

[31] J. B. Sokoloff. Electron localization in crystals with quasiperiodic lattice potentials. *Phys. Rev. B*, 22:5823–5828, Dec 1980.

[32] Trithep Devakul and David A. Huse. Anderson localization transitions with and without random potentials. *Phys. Rev. B*, 96:214201, Dec 2017.

[33] Giacomo Roati, Chiara D'Errico, Leonardo Fallani, Marco Fattori, Chiara Fort, Matteo Zaccanti, Giovanni Modugno, Michele Modugno, and Massimo Inguscio. Anderson localization of a non-interacting bose-einstein condensate. *Nature*, 453:895–8, 07 2008.

[34] B. Deissler, Matteo Zaccanti, Giacomo Roati, Chiara D'Errico, Marco Fattori, M. Modugno, Giovanni Modugno, and M. Inguscio. Delocalization of a disordered bosonic system by repulsive interactions. *Nature Physics*, 6, 10 2009.

[35] Shankar Iyer, Vadim Oganesyan, Gil Refael, and David A. Huse. Many-body localization in a quasiperiodic system. *Phys. Rev. B*, 87:134202, Apr 2013.

[36] Michael Schreiber, Sean S Hodgman, Pranjal Bordia, Henrik P Lüschen, Mark H Fischer, Ronen Vosk, Ehud Altman, Ulrich Schneider, and Immanuel Bloch. Observation of many-body localization of interacting fermions in a quasirandom optical lattice. *Science*, 349(6250):842–845, 2015.

[37] Pranjal Bordia, Henrik P. Lüschen, Sean S. Hodgman, Michael Schreiber, Immanuel Bloch, and Ulrich Schneider. Coupling identical one-dimensional many-body localized systems. *Phys. Rev. Lett.*, 116:140401, Apr 2016.

[38] Mac Lee, Thomas R. Look, S. P. Lim, and D. N. Sheng. Many-body localization in spin chain systems with quasiperiodic fields. *Phys. Rev. B*, 96:075146, Aug 2017.

[39] Vedika Khemani, D. N. Sheng, and David A. Huse. Two universality classes for the many-body localization transition. *Phys. Rev. Lett.*, 119:075702, Aug 2017.

[40] Henrik P. Lüschen, Pranjal Bordia, Sebastian Scherg, Fabien Alet, Ehud Altman, Ulrich Schneider, and Immanuel Bloch. Observation of slow dynamics near the many-body localization transition in one-dimensional quasiperiodic systems. *Phys. Rev. Lett.*, 119:260401, Dec 2017.

[41] Pranjal Bordia, Henrik Lüschen, Sebastian Scherg, Sarang Gopalakrishnan, Michael Knap, Ulrich Schneider, and Immanuel Bloch. Probing slow relaxation and many-body localization in two-dimensional quasiperiodic systems. *Phys. Rev. X*, 7:041047, Nov 2017.

[42] Thomas Kohlert, Sebastian Scherg, Xiao Li, Henrik P. Lüschen, Sankar Das Sarma, Immanuel Bloch, and Monika Aidelsburger. Observation of many-body localization in a one-dimensional system with a single-particle mobility edge. *Phys. Rev. Lett.*, 122:170403, May 2019.

[43] G.D. Mahan. *Many-Particle Physics*. Physics of Solids and Liquids. Springer US, 1990.

[44] P.W. Anderson. Theory of dirty superconductors. *Journal of Physics and Chemistry of Solids*, 11(1):26–30, 1959.

[45] T. Dekker. Finding a zero by means of successive linear interpolation. *Constructive Aspects of the Fundamental Theorem of Algebra*, 01 1969.

[46] Richard Brent. An algorithm with guaranteed convergence for finding a zero of a function. *Comput. J.*, 14:422–425, 04 1971.

[47] Amit Ghosal, Mohit Randeria, and Nandini Trivedi. Inhomogeneous pairing in highly disordered s-wave superconductors. *Phys. Rev. B*, 65:014501, Nov 2001.

[48] Chao Tang and Mahito Kohmoto. Global scaling properties of the spectrum for a quasiperiodic schrödinger equation. *Phys. Rev. B*, 34:2041–2044, Aug 1986.

[49] D. J. Thouless. Bandwidths for a quasiperiodic tight-binding model. *Phys. Rev. B*, 28:4272–4276, Oct 1983.

[50] J. H. Han, D. J. Thouless, H. Hiramoto, and M. Kohmoto. Critical and bicritical properties of harper's equation with next-nearest-neighbor coupling. *Phys. Rev. B*, 50:11365–11380, Oct 1994.

[51] Fangli Liu, Somnath Ghosh, and Y. Chong. Localization and adiabatic pumping in a generalized aubry-andré-harper model. *Physical Review B*, 91, 06 2014.

[52] Alexander Weisse, Gerhard Wellein, Andreas Alvermann, and H. Fehske. The kernel polynomial method. *Reviews of Modern Physics*, 78, 05 2005.

[53] Richard B. Lehoucq, Danny C. Sorensen, and Chao Yang. Arpack users' guide - solution of large-scale eigenvalue problems with implicitly restarted arnoldi methods. In *Software, environments, tools*, 1998.

[54] Yangsu Xie, Zaoli Xu, Shen Xu, Zhe Cheng, Nastaran Hashemi, Cheng Deng, and Xinwei Wang. The defect level and ideal thermal conductivity of graphene uncovered by residual thermal reffusivity at the 0 k limit. *Nanoscale*, 7:10101–10110, 2015.

[55] N. Kopnin and Edouard Sonin. Bcs superconductivity of dirac electrons in graphene layers. *Physical review letters*, 100:246808, 06 2008.

[56] Manfred Sigrist and Kazuo Ueda. Phenomenological theory of unconventional superconductivity. *Rev. Mod. Phys.*, 63:239–311, Apr 1991.

[57] Bruno Uchoa and Antonio Castro Neto. Superconducting states of pure and doped graphene. *Physical review letters*, 98:146801, 05 2007.

[58] Ferdinand Evers and A. Mirlin. Anderson transitions. *Rev. Mod. Phys*, 80:1355–1417, 10 2008.

[59] E. Abrahams, P. W. Anderson, D. C. Licciardello, and T. V. Ramakrishnan. Scaling theory of localization: Absence of quantum diffusion in two dimensions. *Phys. Rev. Lett.*, 42:673–676, Mar 1979.

[60] Bernhard Kramer and Angus MacKinnon. Localization: Theory and experiment. *Rep. Prog. Phys.*, 56:1469–1564, 12 1993.

[61] Franz J. Wegner. Electrons in disordered systems. Scaling near the mobility edge. *Zeitschrift fur Physik B Condensed Matter*, 25(4):327–337, December 1976.

[62] A. MacKinnon and B. Kramer. One-parameter scaling of localization length and conductance in disordered systems. *Phys. Rev. Lett.*, 47:1546–1549, Nov 1981.

[63] D. Vollhardt and P. Wölfle. Diagrammatic, self-consistent treatment of the anderson localization problem in d<=2 dimensions. *Phys. Rev. B*, 22:4666–4679, Nov 1980.

[64] Mahito Kohmoto, Leo P. Kadanoff, and Chao Tang. Localization problem in one dimension: Mapping and escape. *Phys. Rev. Lett.*, 50:1870–1872, Jun 1983.